CHALMERS
UNIVERSITY OF TECHNOLOGY

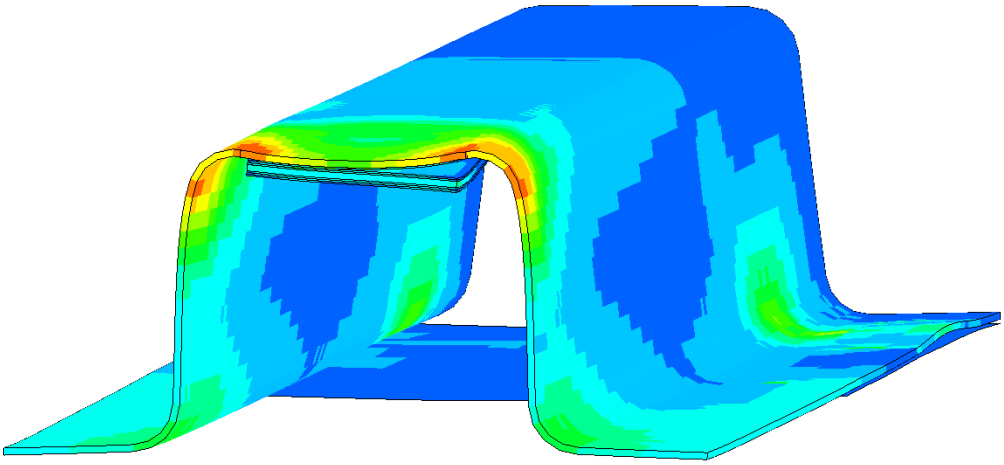

Benchmarking study of steel-composite structures in CAE crash applications

Master's thesis in Applied Mechanics

MADELEINE ANDERSSON
EMMA LARSSON

Department of Applied Mechanics
CHALMERS UNIVERSITY OF TECHNOLOGY
Göteborg, Sweden 2016

MASTER'S THESIS IN APPLIED MECHANICS

Benchmarking study of steel-composite structures in CAE crash applications

MADELEINE ANDERSSON
EMMA LARSSON

Department of Applied Mechanics
Division of Material and Computational Mechanics
CHALMERS UNIVERSITY OF TECHNOLOGY

Göteborg, Sweden 2016

Benchmarking study of steel-composite structures in CAE crash applications
MADELEINE ANDERSSON
EMMA LARSSON

Master's thesis 2016:23
ISSN 1652-8557
Department of Applied Mechanics
Division of Material and Computational Mechanics
Chalmers University of Technology
SE-412 96 Göteborg
Sweden
Telephone: +46 (0)31-772 1000

Cover:
Cross section at midpoint of steel-composite hat profile at initial delamination.

Chalmers Reproservice
Göteborg, Sweden 2016

Benchmarking study of steel-composite structures in CAE crash applications
Master's thesis in Applied Mechanics
MADELEINE ANDERSSON
EMMA LARSSON
Department of Applied Mechanics
Division of Material and Computational Mechanics
Chalmers University of Technology

Abstract

One of the major issues for decreasing the environmental impact of the automotive industry is lowering the weight of the vehicles. For weight reduction purposes, fibre reinforced polymer composites are of interest due to their desirable stiffness per weight properties and the ability to design the material for its specific purpose. Since the development process of this industry is highly based on computer simulations of the components performance, it is of importance to develop the simulation models. This in order to obtain reliable results of the potential failure of the fibre reinforced polymer components and how the composite interacts with metal materials, e.g. in automotive crash simulations. The work within the project is focusing on increasing the understanding of how to model the failure behaviour of mixed material automotive components (a combination of fibre reinforced polymer and ultra high strength steel) at a reasonable computational cost.

In this report, a benchmarking study of modelling composite materials using the explicit FE solver LS-DYNA is described, focusing on capturing the delamination behaviour in the lamina interface as well as the composite steel interface. For the study different modelling aspects are investigated, such as composite material models available in LS-DYNA, the compatibility of element types and material models and two different types of adhesive modelling (a tiebreak condition and a cohesive zone). Simulations are run to test the mode I and mode II delamination behaviour.

The simulation model is validated using experimental data. The experiments were conducted, specifically for the project, using two different composite laminates. The procedure of designing the composite laminate stackup is described in the report. In both experimental tests the composite shows delamination as well as failure in the composite. The joining between the steel and composite is undamaged in both test cases.

The recommendations for modelling of steel-composite structures, includes modelling both steel and composite using thick-shell elements, modelling the adhesive between steel and composite as well as the lamina interface with cohesive elements. LS-DYNA version R9.0.0. is needed in order for the described model procedure to work as intended.

Keywords: Fibre composite, Composite failure, Delamination, Crash analysis, Finite Element Method, LS-DYNA, Composite-steel interface, Comparison Tiebreak and Cohesive zone modelling, Failure modelling using cohesive zone, Material card comparison

Preface

The work within the project is focusing on increasing the understanding of how to model the failure in mixed material automotive components (a combination of fibre reinforced polymer and ultra high strength steel). The project was conducted at Chalmers University of Technology in cooperation with the companies Case5 and Gestamp HardTech.

Case5 is a consulting company in Gotheburg established in 2010 with a wide range of customers from different industries, such as automotive, aviation, space, and offshore. The company provides their customers with structural analysis simulations and help them to achieve weight and performance optimised products by using state of the art simulation methods.

Gestamp HardTech is a company located in Luleå developing and manufacturing press hardened ultra high strength steel components for the automotive industry as well as press hardening tools.

Acknowledgements

Firstly, thank you to DYNAmore Nordic AB for providing us with a license to LS-DYNA, and to BETA CAE Systems supplying us with the pre- and postprocessors ANSA and μETA. An extra thanks to the staff at DYNAmore Nordic for answering our many questions and going that extra mile and providing us with the newest BETA version of LS-DYNA.

To our supervisor at Case5, Salar Mostofizadeh, we are very grateful for all your help and support. Also, a great thanks to all co-workers at Case5, for all the help and the great laughs that have carried us through the project.

To our examiner and supervisor at Chalmers, Martin Fagerström, we are thankful for your support.

We want to acknowledge our contact at Gestamp Hardtech, Lars Wikström, for being so accommodating and helpful.

Last but not least, we are thankful for our families and friend being so supportive and understanding.

Contents

1 Introduction

1.1 Background

The automotive industry strives towards reducing the environmental impact. One of the major issues for this improvement is to reduce the weight of the vehicles. In order to do so new technologies and design solutions are required. Fibre reinforced polymer composites are of interest due to their desirable stiffness per weight properties and the ability to design the material for its specific purpose.

For the automotive industry, a limiting factor for the weight reduction is the crash safety. The energy absorption prediction needs to be accurate for the crash simulations during the development process, and this is yet only achievable for metals and polymers with well-known behaviour. An interesting industrial approach to reduce the vehicle weight is to combine fibre reinforced polymers for increased stiffness (per weight unit) with ultra high strength steel for energy absorption in the safety structure. Since the development process of this industry is highly based on computer simulations of the component performance, it is of importance to develop the simulation models in order to obtain reliable results of the potential failure of the fibre reinforced polymer components, e.g. in automotive crash simulations.

1.2 Purpose

The purpose of the project has been to establish a modelling method for mixed material (fibre reinforced polymer and ultra high strength steel) automotive components in crash scenarios, suitable for the needs within the component development process at Gestamp HardTech.

1.3 Objective

The main objective has been to take a step forward from the simulation models used by Gestamp Hardtech in level of failure prediction in both cracking and delamination of the composite material. The project should determine what material model and element type to use in crash simulations of fibre reinforced composites, how the interaction and interface between steel and composite should be modelled, and which level of detail is necessary in the simulations in order to achieve a satisfactory prediction of failure and energy in the mixed material component.

1.4 Limitations

The project did not take manufacturing methods into account, and only focused on the impact simulations matching the crash scenarios for hat profiles given by Gestamp HardTech. The analysis was performed in LS-DYNA and the pre- and post-processing carried out in ANSA and μETA respectively. The material models and failure criteria investigated will therefore be limited to the ones available in LS-DYNA [1].

2 Theory

A composite is a material consisting of two or more constituent materials with significantly different physical properties. The combination of the constituent materials gives a composite with noticeably different properties compared to the individual constituents. Still, the characteristics of the composite are strongly influenced by the properties of the included materials, their distribution, and the interaction between them. The constituents may interact in such a way that the properties of the composite are not so easily provided as by the volume-fraction sum of the separate material properties. Many factors therefore need to be accounted for when modelling a composite, such as the reinforcements concentration, concentration distribution, and orientation.

The composite materials are classified based on the geometry of the reinforcement. The basic categories are particle- and fibre-reinforcement. The particles are of approximately the same length in all directions, e.g. a sphere or a cube, whereas the fibre is characterised by its length being much greater than its cross section dimensions. Reinforcing fibres may be short or long compared with its overall dimensions. Composites with short fibres are called discontinuous-fibre-reinforced composites while composites with long fibres are called continuous-fibre-reinforced composites.

The fibre reinforced polymer composites have become an important class of composite materials due to their ability of achieving high stiffness and strength at low weight. The continuous fibres may be aligned in one direction and bound together and protected by a matrix, e.g. a polymer. This is called a unidirectional (UD) composite, see Figure 2.1 with axis 1 in the *longitudinal direction* (along the fibres), axis 2 in the *transverse direction* in the lamina plane and axis 3 in the *through thickness direction* perpendicular to the lamina plane. These UD-plies have very different properties in the longitudinal and the transverse directions. Therefore, UD-plies are stacked together with varying fibre directions to form laminates with a desired behaviour. [2]

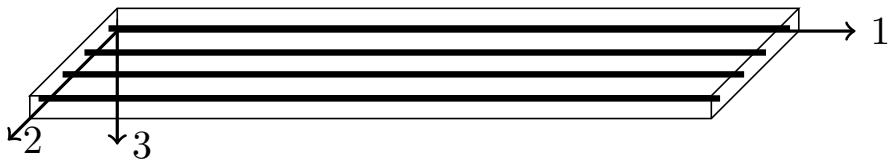

Figure 2.1: *Schematic representation of a unidirectional composite, with axis 1 and 2 in the longitudinal and transverse directions respectively, and axis 3 in the through thickness direction.*

2.1 Failure process of a composite

The failure process in a composite is significantly different and more complex than the fracture process in homogeneous and on the global scale isotropic materials such as metal and polymers. In isotropic materials the crack growth is often a simple enlargement of the crack without branching or directional changes, also known as self-similar crack growth. In composite laminates on the other hand, the crack growth is generally different in plies with different fibre orientation. Therefore, it is not possible to define a unique crack length and it becomes more meaningful to analyse a damage zone ahead of the crack. [2]

The damage zone includes several energy absorbing mechanisms since internal material failure generally proceeds the macroscopic failure of the specimen. The internal material failure may appear in various forms separately or combined, such as (i) breaking of fibres, (ii) microcracking of the matrix, (iii) separation of fibres from the matrix, i.e. debonding and (iv) separation of adjacent plies, i.e. delamination. Generally, due to the internal failure, the material response changes well before the actual failure of the specimen. The failure load of a UD composite may therefore either be considered as the load at which the material behaviour deviates from linear stress-strain response or the load at final fracture. Note that most UD composites have a linear stress-strain response up to failure. [2]

The main failure modes of laminated fibre-reinforced composites are matrix compression failure, fibre compression failure, matrix tensile failure, fibre tensile failure and delamination [3]. These failure modes are described further in the subsections below.

2.1.1 Compressive failure

When subjected to longitudinal compressive loading the fibres of the composite can be seen as long columns and therefore are at risk of buckling. When appearing within a composite it is referred to as fibre microbuckling [2]. Kink bands are commonly observed in the compressive failure mode and may be a consequence of microbuckling. Note that there is a discussion in the literature concerning the kinking being a separate failure mode and not being seen as a consequent of microbuckling. Kinking is a localized shear deformation of the matrix, along a band across the fibres. This deformation is triggered by imperfections in the material, particularly initial fibre misalignments, and by the rotation of the fibres during the compressive loading. The failure mode is also affected by the resin shear behaviour [3]. Due to these factors, the failure mechanism typically takes place is regions with a lower level of shear stress and higher compressive stress or when severe local fibre misalignments take place in the composite [4]. The failure mode is illustrated in Figure 2.2a.

The predominant failure mode of a unidirectional composite subjected to transverse compression is matrix shear failure with or without constituent debonding and/or fibre crushing. The failure of the specimen may be accelerated by failure of the fibre-resin bond, resulting in a lower transverse compressive strength than the longitudinal transverse strength [2]. The failure surface typically has a 53° angle to the loading axis [**Pinho2005**]. This failure mode is illustrated in Figure 2.2b.

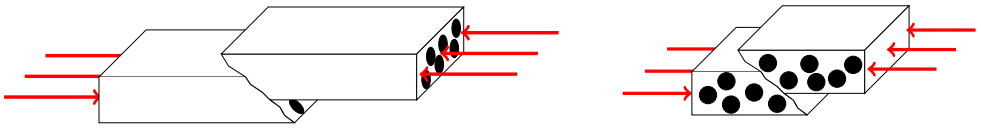

(a) (b)

Figure 2.2: *Failure modes when the composite is subjected to compression; (a) shear failure mode due to longitudinal loading and (b) matrix shear failure due to transverse loading.*

2.1.2 Tensile failure

In a UD composite subjected to an increasing longitudinal tensile load, failure is initiated by fibre breakage at their weakest cross sections. Individual fibres break until the cross section of the composite is unable to sustain the load and failure of the specimen occurs. This brittle failure may arise with or without additional failure mechanisms like fibre pullout, interface-matrix shear or constituent debonding. The brittle failure of a UD composite subjected to longitudinal tension is illustrated in Figure 2.3a.

When subjected to a transverse tensile load, the main failure mode is matrix tensile failure. This is due to stress concentration at the interface and in the matrix created by the fibres aligned perpendicular to the loading direction. If the fibres are highly aligned and are weak in the transverse direction, the failure may originate by fibre transverse tensile failure, i.e. fibre splitting. Another failure mechanism that may occur is constituent debonding, i.e failure of interfacial bonds between the fibre and the matrix. The matrix tensile failure is illustrated in Figure 2.3b.[2]

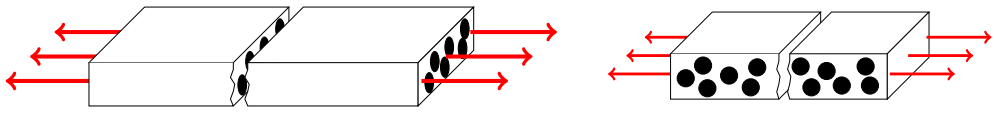

(a) (b)

Figure 2.3: *Failure modes when the composite is subjected to compression; (a) shear failure mode due to longitudinal loading and (b) matrix shear failure due to transverse loading.*

2.1.3 Delamination

As stated above, composite laminates consists of distinct plies that are stacked together. One critical failure mode is delamination, i.e. the plies detaching from each other [3]. Composite laminates are highly susceptible to crack initiation and propagation along the laminar interfaces, this is one of the most common life-limiting

crack growth modes in composite laminates. This may cause severe reduction of in-plane strength and stiffness, potentially leading to catastrophic failure of the whole structure [5]. Even if the delamination is not visible on the surface or the free edges it may affect the material properties [3].

When the composite is subjected to a 2D load, 3D stress states still needs to be accounted for. The stresses σ_3, τ_{13} and τ_{23} are called interlaminar stresses and may initiate delamination. Their magnitude is largest at the lamina interface, i.e. where the plies are stuck together, and at the edges of the lamina. A specimen developing a tensile value of the interlaminar normal stress, σ_3, shows delamination much prior to the fracture of the specimen. A specimen developing a compressive normal stress at the free edge shows very little evidence of delamination even when fracture occurs. [2]

The interlaminar stresses are affected by the angles of the plies and the laminate stacking sequence. The crack propagation along a laminar interface has three different modes; (i) mode I - pure opening of the crack, (ii) mode II - pure sliding between the layers and (iii) mode III - tearing. These three modes are illustrated in Figure 2.4. Mode I propagation is driven by a force or stress that opens the crack in the normal direction to the crack surface, mode II propagation is driven by a force or stress in the direction of the crack propagation and mode III is drive by a force or stress perpendicular to the crack propagation direction. [2]

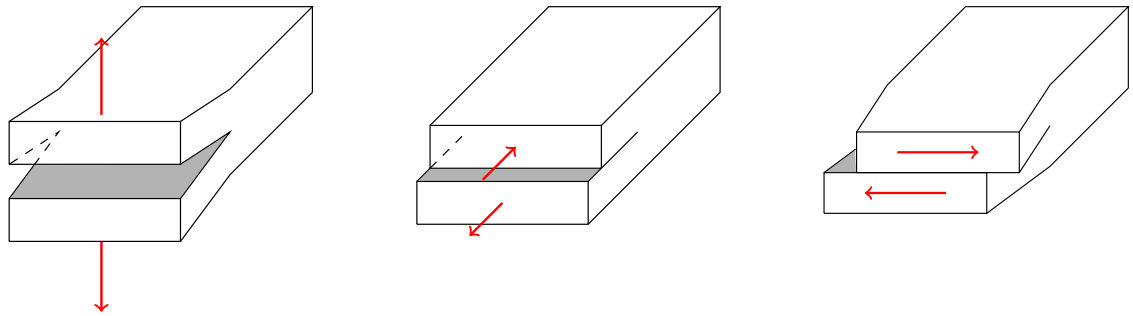

(a) (b) (c)

Figure 2.4: *Delamination modes, (a) mode I - opening of the crack in the normal direction, (b) mode II - sliding between the plies, and (c) mode III - tearing of the composite.*

2.2 Non-crimp fabric

Non-crimp fabrics (NCF) are reinforcement fabrics created to combine the accurate fibre alignment of UD tapes with the easy handling of the woven fibres. If unidirectional tapes are used, either placed by hand or by a robot, and the structure is cured in an autoclave the fibre placement and local properties can be used efficiently. However, the manufacturing is inconvenient and costly. On the contrary, if a woven reinforcement is used, and the curing is handled without an autoclave, the manufacturing process cost can be lowered significantly since large sheets of fabric are handled. In woven materials the mechanical properties are affected by the waviness of the fibres that the woven structure imposes, which means that more material is required, compared to the material cost of a UD tape. [6]

The NCF may be produced in various variants, with the basic idea of bundles of fibres being aligned and held together by weft threads [6]. This enables a fabric that behaves as a woven material in manufacturing but structurally similar to a UD material, although with reduced longitudinal stiffness and longitudinal strength. The name non-crimp comes from that the fibre reinforcement is considered ideally straight in the fibre direction, which means that the fibres are not prebuckled when subjected to longitudinal compressive loads [7]. A schematic figure of a unidirectional NCF is illustrated in Figure 2.5.

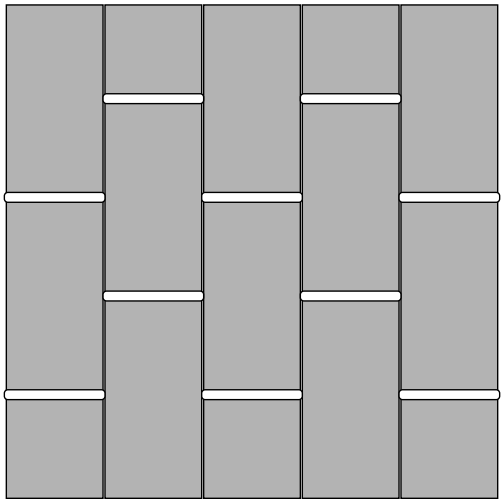

Figure 2.5: *A schematic figure of a non-crimp fabric (NCF), with vertically aligned bundles of fibres (gray) held together by weft threads (white).*

2.3 Classic laminate theory

The classic laminate theory includes some general assumptions; plane stress, linearly elastic orthotropic layers, perfect bonding between fibres and matrix as well as between layers [8]. For classic laminate theory the relation between the resultant forces ($\mathbf{N}$) and moments ($\mathbf{M}$) acting on a laminate cross section and the midplane strain ($\boldsymbol{\epsilon}_0$) and the curvature ($\boldsymbol{\kappa}$), is presented in Equation (2.1). The matrices are called the extensional stiffness matrix ($\mathbf{A}$), the coupling stiffness matrix ($\mathbf{B}$), and the bending stiffness matrix ($\mathbf{D}$). Note that for a symmetric stackup the coupling stiffness matrix becomes zero and therefore there is no coupling between curvature and strain. [2]

$$\begin{Bmatrix} \mathbf{N} \\ \mathbf{M} \end{Bmatrix} = \begin{bmatrix} \mathbf{A} & \mathbf{B} \\ \mathbf{B} & \mathbf{D} \end{bmatrix} \begin{Bmatrix} \boldsymbol{\epsilon}_0 \\ \boldsymbol{\kappa} \end{Bmatrix} \tag{2.1}$$

The matrices are calculated according to Equation (2.2)-(2.4). The contribution of each layer of the composite is determined using the distance to the midpoint (h). This component is defined in Figure 2.6.

$$A_{ij} = \sum_{k=1}^{n} \left(\bar{Q}_{ij}\right)_k \left(h_k - h_{k-1}\right) \tag{2.2}$$

$$Bij = \frac{1}{2} \sum_{k=1}^{n} \left(\bar{Q}_{ij}\right)_k \left(h_k^2 - h_{k-1}^2\right) \tag{2.3}$$

$$D_{ij} = \frac{1}{3} \sum_{k=1}^{n} \left(\bar{Q}_{ij}\right)_k \left(h_k^3 - h_{k-1}^3\right) \tag{2.4}$$

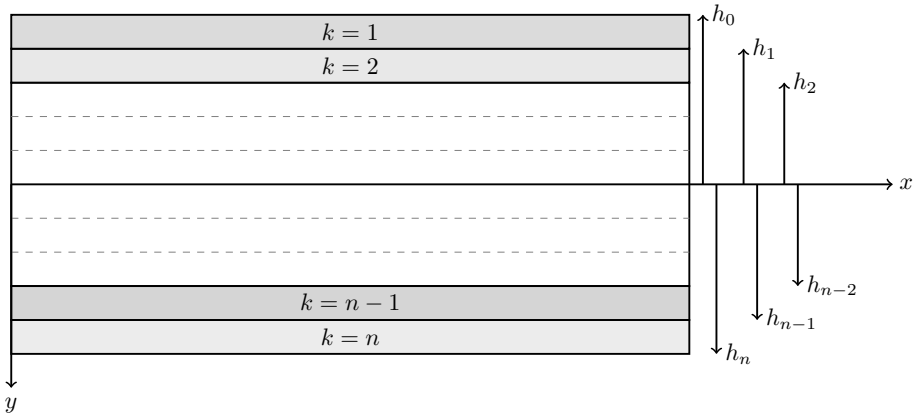

Figure 2.6: *Schematic figure of how the distance from the midpoint (h_k) is defined.*

The included parameters are presented in Equations (2.5)-(2.8). $\bar{Q}$ is the lamina stiffness matrix in the global x, y, z-coordinate system and is constant for each lamina. It is determined using the lamina stiffness matrix in the local $1, 2, 3$-coordinate system Q and the matrices T_1 and T_2 which are the stress and the strain transformation matrices respectively. θ is the angle of the fibres, i.e. the angle between axis 1 and x, see Figure 2.7. [2]

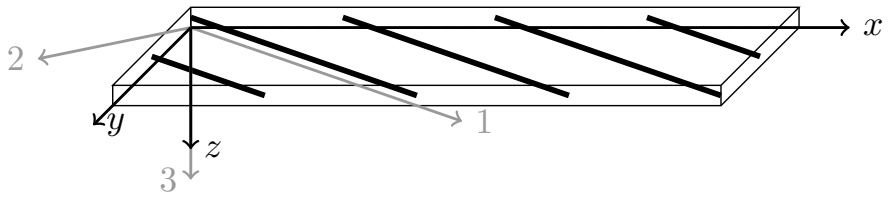

Figure 2.7: *Composite UD ply with the local $1, 2, 3-$coordinate system and the global $x, y, z-$coordinate system.*

$$\bar{Q} = [T_1]^{-1} Q [T_2] \tag{2.5}$$

$$Q = \begin{bmatrix} Q_{11} & Q_{12} & Q_{13} \\ Q_{21} & Q_{22} & Q_{23} \\ Q_{31} & Q_{32} & Q_{33} \end{bmatrix} = \begin{bmatrix} \dfrac{E_{11}}{1-\nu_{12}\nu_{21}} & \dfrac{\nu_{12}E_{11}}{1-\nu_{12}\nu_{21}} & 0 \\ \dfrac{\nu_{12}E_{22}}{1-\nu_{12}\nu_{21}} & \dfrac{E_{22}}{1-\nu_{12}\nu_{21}} & 0 \\ 0 & 0 & G_{12} \end{bmatrix} \tag{2.6}$$

$$T_1 = \begin{bmatrix} \cos(\theta)^2 & \sin(\theta)^2 & 2\cos(\theta)\sin(\theta) \\ \sin(\theta)^2 & \cos(\theta)^2 & -2\cos(\theta)\sin(\theta) \\ -\cos(\theta)\sin(\theta) & \cos(\theta)\sin(\theta) & \cos(\theta)^2 - \sin(\theta)^2 \end{bmatrix} \tag{2.7}$$

$$T_2 = \begin{bmatrix} \cos(\theta)^2 & \sin(\theta)^2 & \cos(\theta)\sin(\theta) \\ \sin(\theta)^2 & \cos(\theta)^2 & -\cos(\theta)\sin(\theta) \\ -2\cos(\theta)\sin(\theta) & 2\cos(\theta)\sin(\theta) & \cos(\theta)^2 - \sin(\theta)^2 \end{bmatrix} \tag{2.8}$$

The stiffness (i.e. relation between stress and strain) of the total composite laminate is calculated using the extensional stiffness matrix since the extensional stiffness relates the resultant forces to the midplane

strains. For bending around the z-axis the x direction is assumed to take up the load (global direction), which corresponds to the value of the first row and first column in $\mathbf{A}$, i.e. $A(1,1)$. The Young's modulus for the entire laminate may then be approximated by dividing this component with the lamina thickness. [2]

2.4 FE-modelling of composites

When modelling a composite laminate using FE there is two general approaches; (i) joining all plies together in one element using a summation of the lamina properties or (ii) modelling each ply with individual element layers and joining the elements together with either a cohesive element or a contact condition [8]. The element configuration of the two approaches is presented in Figure 2.8

(i) When modelling the laminate using only one element, each lamina has an individual through thickness integration point in order to capture the stress state in each ply. This method does not take the delamination into account. This approach has a low computational cost since only one element through the thickness of the lamina is required. It is possible to either sum up the properties using classic laminate theory or to sum the properties in a manner that takes the through thickness stress into account. [8]

(ii) The method of modelling each ply with a layer of elements is computationally heavy, but in return the delamination behaviour can be included in the analysis if the joining between the element layers allows for separation. [8]

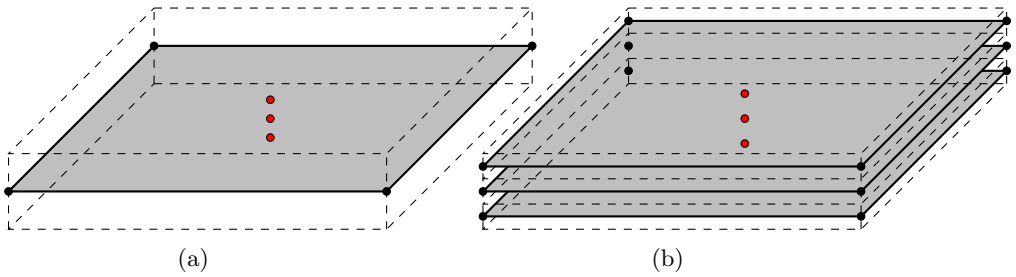

Figure 2.8: *Mesh and integration point configuration for a composite element with three layers of (a) all plies joined into a single layer and (b) the plies modelled with individual elements with the integration points marked with red points.*

2.5 Common numerical errors in FE-modelling

There are some numerical errors that can appear in a finite element analysis. The different types of numerical errors and why they occur are described below.

2.5.1 Hourglass

Hourglass modes are nonphysical, zero energy modes of deformation corresponding to zero strain and stress, and can occur when using reduced integration [9]. A schematic figure of an hourglass mode is presented in Figure 2.9. As can be seen in Figure 2.9 the strain at the midpoint between the nodes remain unchanged. Since hourglass deformation modes are unnoticed by the integration point, work done by the hourglass resistance is neglected in the energy equation. This may lead to a small loss of energy [10].

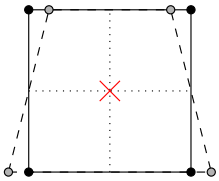

Figure 2.9: *A schematic figure of a zero energy hourglass mode, for an element with one integration point (red).*

2.5.2 Shear locking

Shear locking is a phenomena of an overly stiff response for a first order element in bending. The shape of the in-plane deflection for a bent element is curved in the ideal case, but for a first order element the deflection within each element is modelled linearly, see Figure 2.10. The energy required to bend the first order element is higher than the energy in the actual case since the angle φ is changed for the first order element. [11]

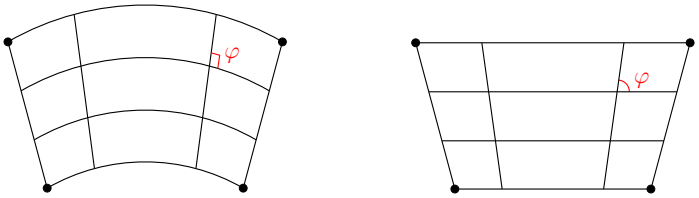

(a) (b)

Figure 2.10: *A schematic figure of the deflection of the actual case (a) and the first order element (b). Figures reproduced and altered from* Shear Locking and Hourglassing in MSC Nastran, ABAQUS, and ANSYS *[11].*

3 Benchmark test-case setup

The simulation results were calibrated and validated using physical test data, provided by Gestamp HardTech. The physical test was conducted at the Gestamp HardTech facilities in Luleå and consisted of a regular three point bending test where the force-displacement relation was recorded in the impactor. For the experiment a composite laminate was designed consisting of a well characterised composite material from Chalmers and Swerea SICOMP [12]. In this section, the properties of the composite material, the procedure of designing the composite laminate, and the setup of the physical test are described.

3.1 Material properties

The composite material used in the tests and simulations is a well characterised non-crimp fabric (NCF) material used for research purposes at Chalmers and Swerea SICOMP. The material consists of carbon fibres in an epoxy matrix, where the carbon fibres are stitched together using glass fibres. The averaged properties of the composite are obtained from tests conducted by Bru et al. [12] and are presented in Table 3.1. Additionally, the volume fraction of the carbon fibres is 60%, the thickness of each ply is 0.18 mm, and the shear fracture angle is 62° [12]. Note that the Young's modulus (E) has different values for compression and tension in both the longitudinal and the transverse direction. All further use of E_{11} and E_{22} is referring to the lower values for the two cases, i.e. E_{11c} and E_{22t}.

Table 3.1: Average values of physical properties for the material used in the tests and simulation. [12]

Young's modulus			
E_{11c}	132	GPa	Longitudinal compression
E_{11t}	140	GPa	Longitudinal tension
E_{22c}	9.3	GPa	Transverse compression
E_{22t}	9	GPa	Transverse tension
Shear modulus			
G_{12}	4.4	GPa	In-plane
G_{13}	3.7	GPa	Through thickness
Strength			
X_c	631	MPa	Longitudinal compression
X_t	1787	MPa	Longitudinal tension
Y_c	130	MPa	Transverse compression
Y_t	29.2	MPa	Transverse tension
S_{12}	77.8	MPa	Shear
Poissons ratio			
ν_{12}	0.28		
ν_{21}	0.029		
ν_{31}	0.02		
ν_{32}	0.43		
Interlaminar energy release rate			
G_I	149	J/m^2	Mode I
G_{II}	690	J/m^2	Mode II
Strain at failure			
ε_{11cu}	0.491	%	
ε_{11tu}	1.23	%	
ε_{22cu}	1.71	%	
ε_{22tu}	0.32	%	
γ_{12u}	9.1	%	
γ_{13u}	2.9	%	
Fracture toughness - initiation value of energy release rate			
$G_{IC,lamcomp}$	51.8	kJ/m^2	
$G_{IC,0°comp}$	103.1	kJ/m^2	
$G_{IC,lamtens}$	33.7	kJ/m^2	
$G_{IC,0°comp}$	67.1	kJ/m^2	

The adhesive used to attach the composite to the steel is a glue from Sika (SikaPower®-MBX Class I), intended for joining of metals and polymers. The mechanical properties are presented in Table 3.2. During the curing process the beam was heat treated. The heat treatment consisted of a temperature of $60°C$ for 20 minutes, then a temperature increase to $175°C$ that was kept for 30 minutes.

Table 3.2: Mechanical properties of the glue used in the experiment [13].

Property	**Value**	
Young's modulus	800	MPa
Lap shear strength	20	MPa
Tensile strength	20	MPa
Elongation at failure	20	%
T-Peel strength	10	N/mm

The steel used in the experiment is a steel manufactured by Gestamp HardTech. The mechanical properties of the steel is presented in Table 3.3, and the yield properties of the steel is presented in Figure 3.1. Note that this is for the steel without the heat treatment.

Table 3.3: Mechanical properties of the steel used in the experiment.

Property	**Value**	
Young's modulus	206	GPa
Poisson's ratio	0.3	

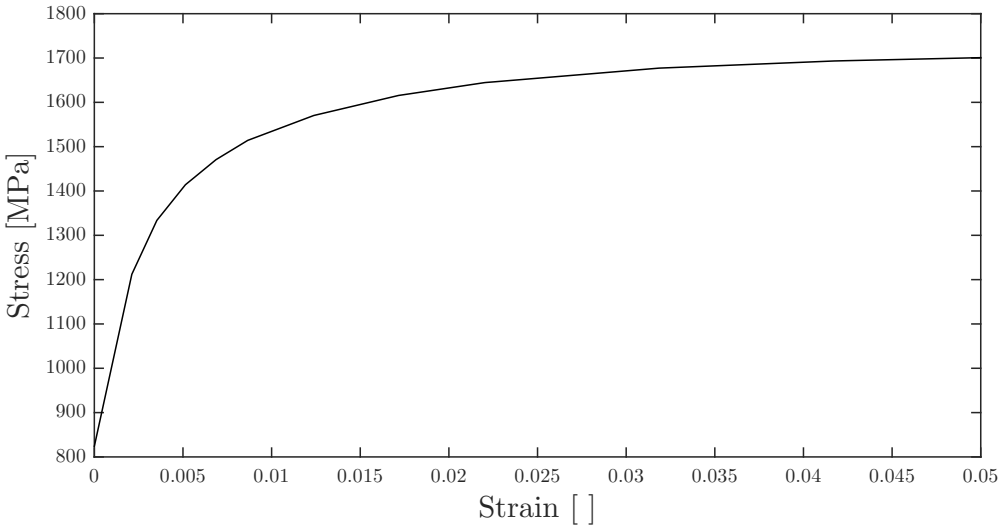

Figure 3.1: *Yield function of the steel used in the experiment.*

3.2 Designing the composite laminate

The design of the composite laminate implemented in the hat profile beam three point bending test, described in Section 3.3, was made to provide a noticeable increase of the bending stiffness of the beam, compared to the pure steel beam. However, the design also takes into account that a too stiff composite laminate may lead to total delamination between the laminate and the steel, resulting in the composite laminate simply falling off. The design also provokes delamination within the laminate since this is a behaviour the simulation model should be able to capture.

In order to approximate the effect of the composite laminate on the bending stiffness of the beam, the bending stiffness of the total beam is compared to the one of the pure steel beam. This is calculated by dividing the beam into parts with constant Young's modulus and second moment of inertia, see Figure 3.2. The bending is assumed to occur around the centre of mass which is in reality not the case for a beam consisting of two different materials, but is in this case considered a reasonable assumption. It can be seen that the pure steel beam is divided into three parts while the mixed-material beam has a fourth part - the composite laminate. Since the bending in the test is around the x-axis, only this bending stiffness component is of interest. Note that the coordinate system is modified from the one in Section 2 in order to match the coordinate system in the model provided by Gestamp Hardtech.

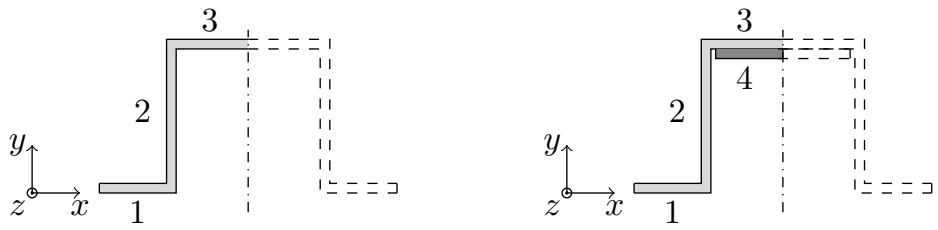

(a) (b)

Figure 3.2: *The cross section of the hat profile beam, with the different parts of the beam with constant Young's modulus and moment of inertia marked numbered. The parts are marked for both (a) the pure steel beam and (b) the combined steel and composite beam. The dash-dotted line represents the symmetry line in the x-direction.*

For each part of the beam, the second moment of inertia for the total centre of rotation is calculated using Steiners law [14], see Equation (3.1). The original second moment of inertia (I) is calculated according to Equation (3.2) [14], with the width and the thickness referred to as w and t respectively. A is the area and b the distance between the centre of rotation for the part and for the total beam. The total bending stiffness is the sum of the individual parts bending stiffness around the centre of the rotation, meaning that each part gives a contribution of the Young's modulus (E) multiplied with the compensated moment of inertia (I_{comp}) from Steiners law, according to Equation (3.3) [14]. For approximating Young's modulus for the composite laminate some further calculations are needed.
As presented in Section 2.3, for a laminate with a linearly elastic composite material where plane stress is assumed, the relation between the resultant forces and the midplane strain may be approximated using components from the extensional stiffness matrix. For bending around the x-axis (see Figure 3.2 for coordinate system), the stiffness corresponding to the strain in the z-direction is of interest.

$$I_{comp} = I + b^2 A \tag{3.1}$$

$$I = \frac{wt^3}{12} \tag{3.2}$$

$$(EI)_{total} = E_1 I_{comp,1} + E_2 I_{comp,2} + ... = \sum_{i=1}^{N} E_i I_{comp,i} \tag{3.3}$$

For the experiment, two different laminate stack-ups are designed. This to secure the simulation model to not be calibrated for only one case. These two laminates are therefore needed to give a different response in the three point bending test. However, only one piece of composite laminate is manufactured, from which both composite plates are to be cut. The design of the composite plate therefore also takes into account that the stiffness needs to be different depending on the placement of the cut out. The two plates, referred to as plate A and plate E, are therefore cut from the same composite laminate but rotated with an angle of 90° from each other, see Figure 3.3. The plate is kept symmetric in order to not introduce any coupling between strain and curvature. Some ±45° plies are included in the laminate to prevent a rapid drop in the force-displacement relation when failure occurs, and also to provoke delamination. Due to the significantly higher Young's modulus, the 0° plies increase the bending stiffness more than any other fibre angle, and therefore plate E has a higher bending stiffness than plate A. The stack-ups of plates A and E are presented in Figure 3.4 and a change of the bending stiffness compared to the pure steel beam is predicted to 11.64% for beam A and 17.41% for beam E.

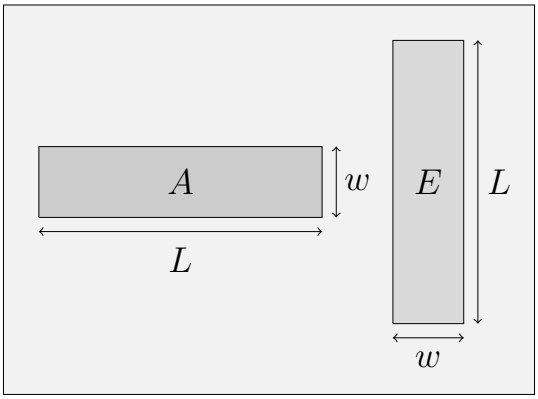

Figure 3.3: *The manufactured composite laminate and how the two different plates, A and E, are cut out.*

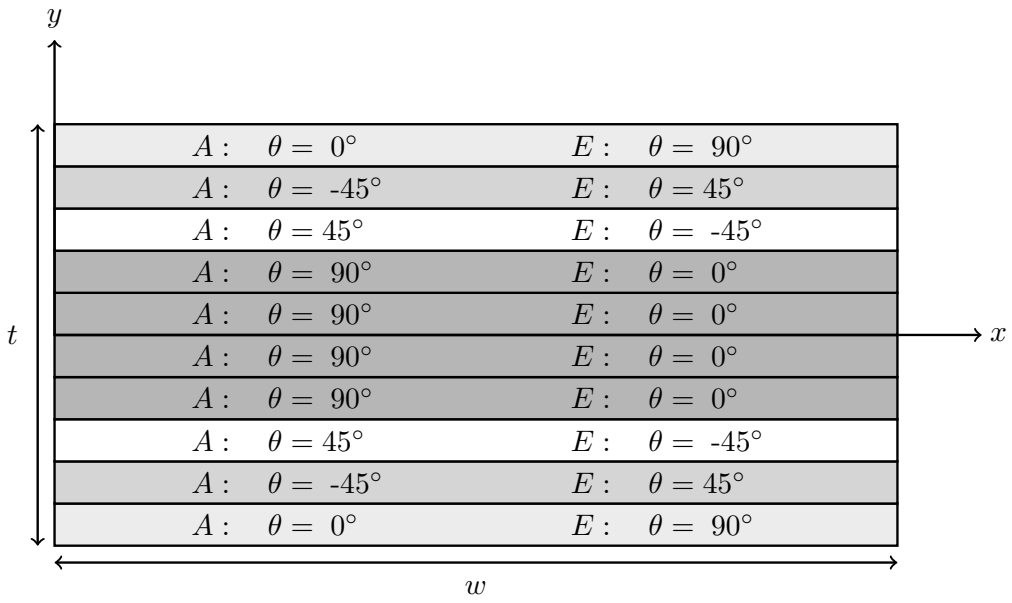

Figure 3.4: *Cross section view of the laminate stackup. The angles of the fibres (θ) are listed to the left for plate A and to the right for plate E. The thickness is referred to as t and the width as w.*

3.3 Experimental setup and result

The three point bending test is performed such that the hat profile beam is placed on two roller supports with an applied load located at the middle of the beam. The applied load is introduced by an impactor, i.e. a cylinder shaped body with a prescribed vertical displacement (δ) pressing on top of the beam. A schematic figure of the test setup is presented in Figure 3.5 along with the beam cross section. As can be seen in the figure, the composite laminate is attached to the top flange of the hat profile. Note that there are two plates attached to the bottom of the hat profile, one in each end of the beam. The purpose of the plates is to keep the bottom flanges together over the supports in order to make the bending of the beam the main deformation mode. The dimensions are presented in Table 3.4. Note that the composite plate does not span over the entire length or width of the profile. The plate measurements are included in the table.

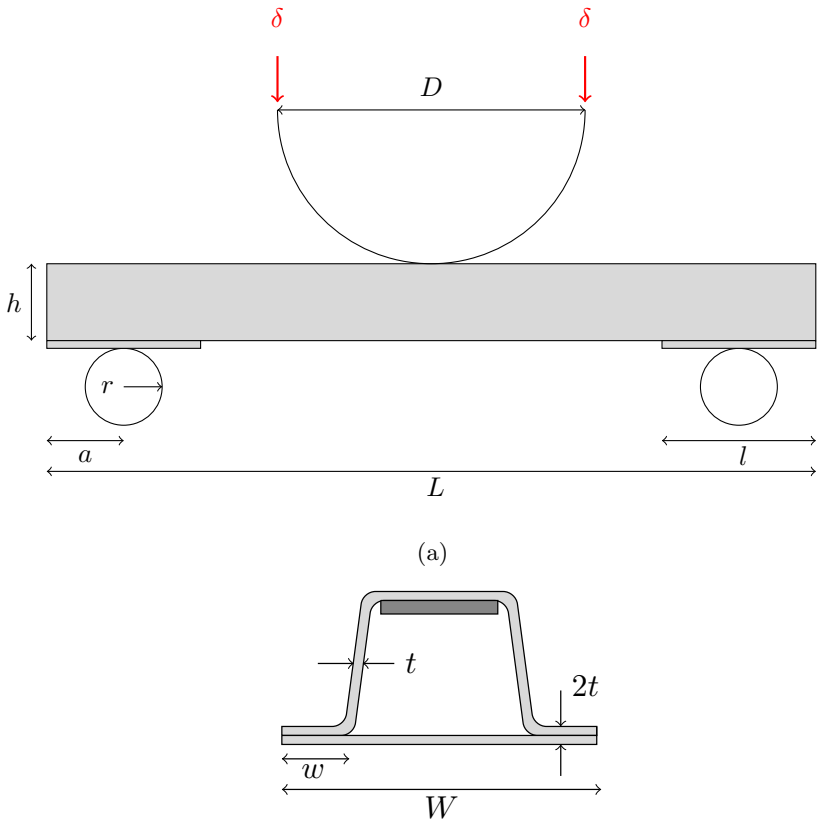

Figure 3.5: *Schematic figure of (a) the three point bending test and (b) the cross section of the beam with the steel hat profile with the lid (light grey) and the attached composite laminate (dark grey).*

Table 3.4: Geometric properties for the hat profile experiment

Dimension	**Length [mm]**	**Description**
D	305	Diameter of impactor
L	490	Length of beam
$L_{composite}$	300	Length of composite plate
l	130	Length of cover plate
a	45	Placement of supports
r	25	Radius of supports
h	36.6	Height of beam
W	82	Width of beam
w	15	Width of flange
$w_{composite}$	24	Width of composite plate
t	0.8	Thickness of steel

A photo of the actual test setup of the three point bending test is presented in Figure 3.6, and a photo of test beam A before the experiment is shown in Figure 3.7. The composite laminate (black) is attached to the top flange of the hat profile using glue (green). The bottom plates have a lighter grey colour in the figure.

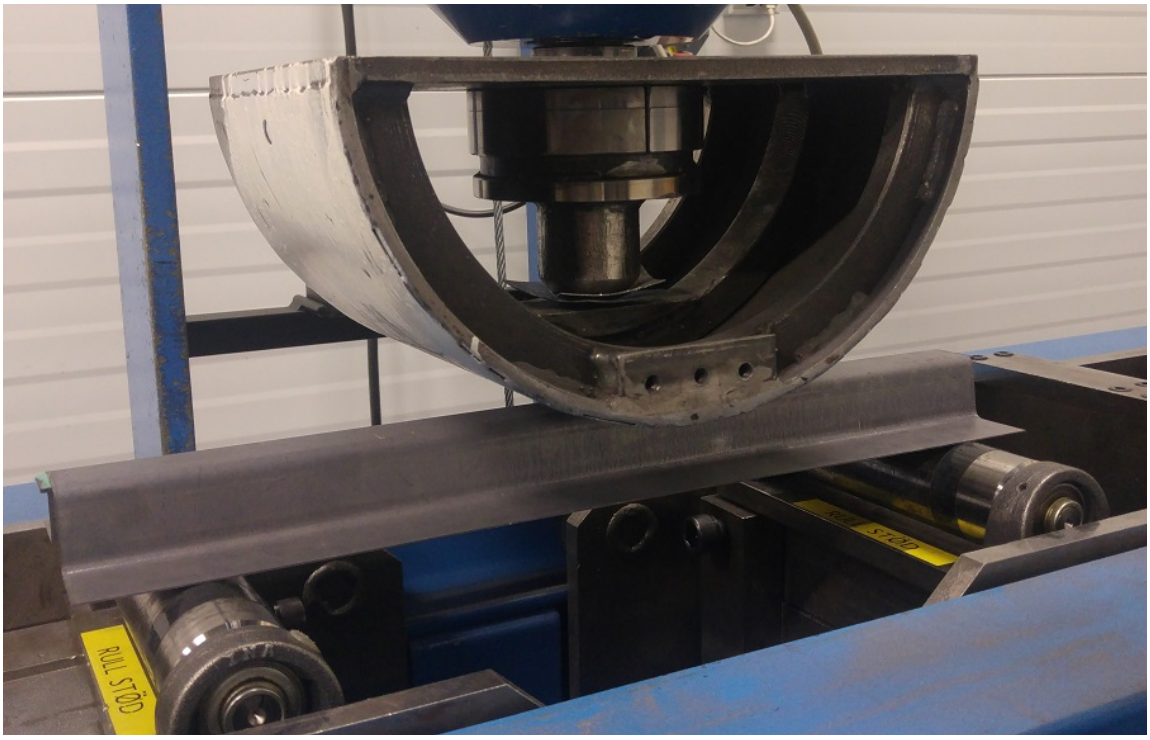

Figure 3.6: *The setup of the three point bending test. The hat profile beam is placed on two roller supports and the impactor is aligned in the middle of the beam.*

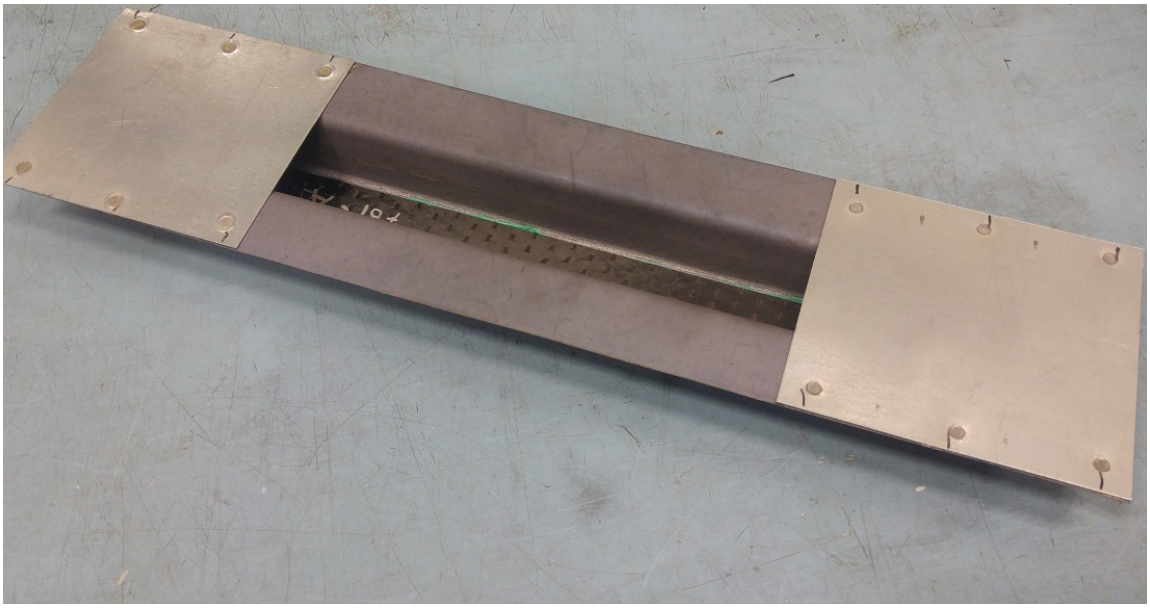

Figure 3.7: *Test beam A before the experiment. The composite is (black) can be seen attached on the top flange of the steel hat profile. The light gray plates are attached to the bottom flanges to prevent them from bending outward along their width. The glue (green) is visible at the edge of the composite.*

The loading profile of the applied displacement can be seen in Figure 3.8 as a time-displacement curve. Note that the displacement starts at a negative value, due to the reference displacement not being set to zero. The velocity for the experiment is approximately 6 mm/s, which indicates quasi static conditions (i.e. no inertial effects need to be considered).

The result in form of a force-displacement curve measured in the impactor is presented in Figure 3.9. As expected, test beam A and test beam E differ in behaviour. Delamination in the composite laminate occurs for both test beams. Since test beam E has a higher bending stiffness, a higher force (and therefore a higher stress) is to be expected at the same displacement, compared to test beam A. This higher stress leads to a delamination at approximately 6 mm for test beam E, between the $\pm 45°$ plies closest to the steel. The delamination can be seen in the force-displacement relation as a rapid drop in the force corresponding to further displacement. For test beam A, a similar decrease of the force can be seen at a displacement of approximately 10 mm. The delamination for test beam A occurs, as for test beam E, in the interface of the top $\pm 45°$ plies. Note that an additional delamination may be detected between the remaining $-45°$ ply and the underlying $0°$ ply, due to the inability of the $-45°$ ply to follow the shape of the steel profile.

After the delamination, the composite plies still attached to the test beam A ($0°$ and $-45°$) have a higher bending stiffness than the plies attached to test beam E ($90°$ and $45°$). This is due to a higher ability of withstanding loads along the length of the plate for a $0°$ ply, compared to a $90°$ ply. This is visible in the diagram as a higher curve for test beam A.

Both beams experience a full buckling behaviour at a displacement of approximately 21 mm. The force corresponding to the applied displacement is then distinctly reduced.

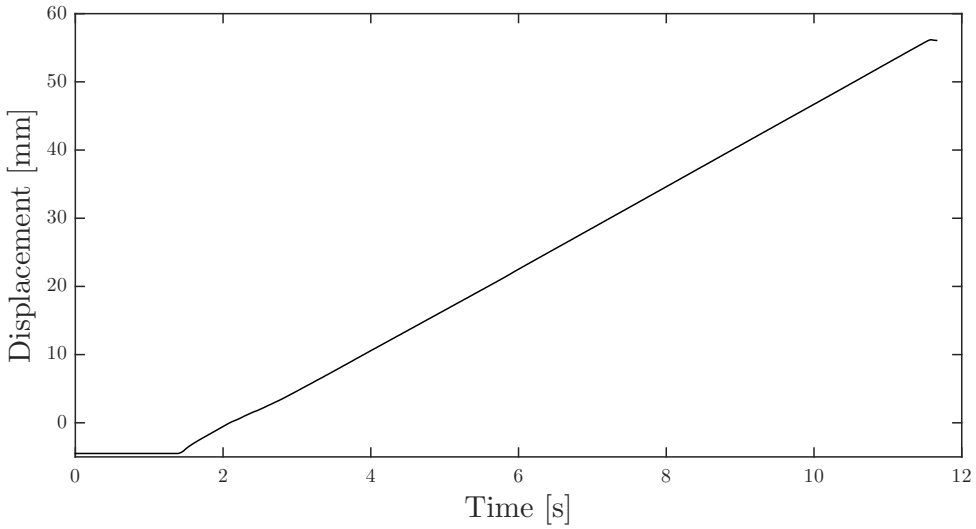

Figure 3.8: *The loading curve of the applied displacement. The displacement starts at a negative value due to the reference displacement not being set to zero.*

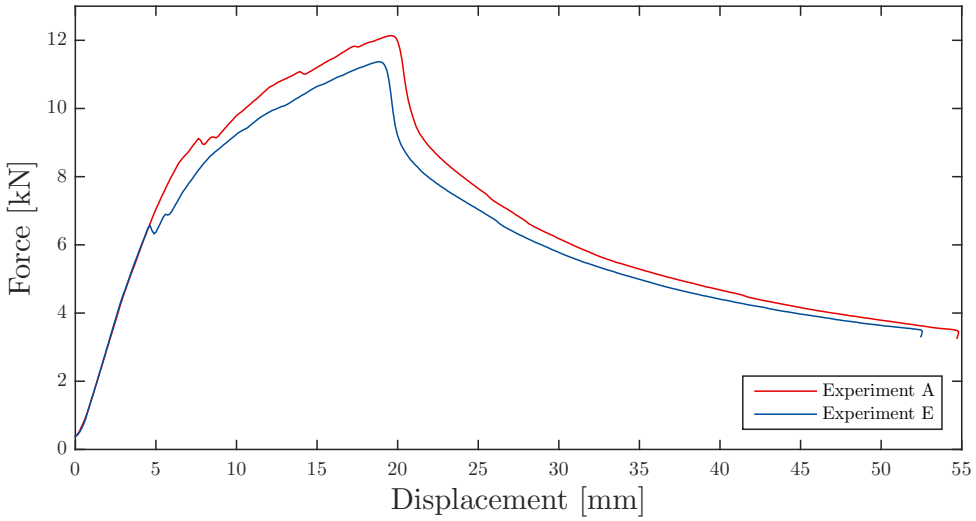

Figure 3.9: *Experimental result for test beam A (red) and test beam E (blue).*

Photos of the test beams after the test are presented in Figure 3.10. The adhesive used to attach the composite to the steel beam is visible in the photos (green). The delamination, which is observed as a rapid decrease of the force needed to induce further delamination, is observed as the inability of the composite to mimic the deformation of the steel beam. In the photo, the delamination is visible along the whole length of the exposed part of laminate for test beam E. For test beam A, the laminate is intact on one side of the buckled steel. In Figure 3.10 this is observed on the left side.

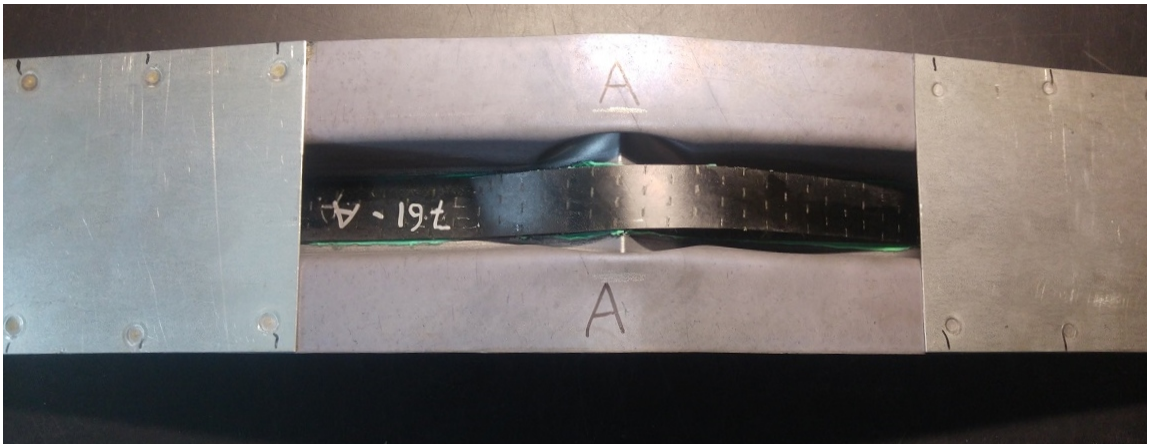

(a)

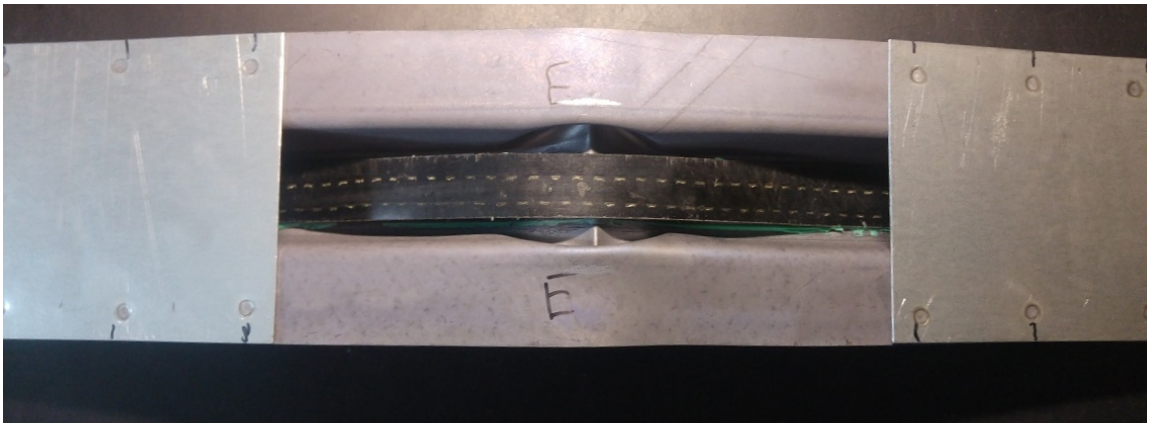

(b)

Figure 3.10: *Photo of the hat profile beam after the experiment for both (a) test beam A and (b) test beam E.*

Due to the severe delamination, the buckling behaviour of the steel and the breakage of the still attached composite plies are not visible in Figure 3.10. Therefore the delaminated parts of the composite were removed and the still attached composite documented, see Figure 3.11. For both test beam A and test beam E, it can be seen that the delamination occurred at a ply with a fibre angle of 45° and that this ply is still attached. The angle of the plies may be seen from the weft thread (white) that runs perpendicular to the fibre direction. Note that an additional delamination may be detected between the remaining $-45°$ ply and the underlying 0° ply, due to the inability of the $-45°$ ply to follow the beams shape. Failure of the composite has occurred in the midpoint of the beam, at the buckling of the steel.

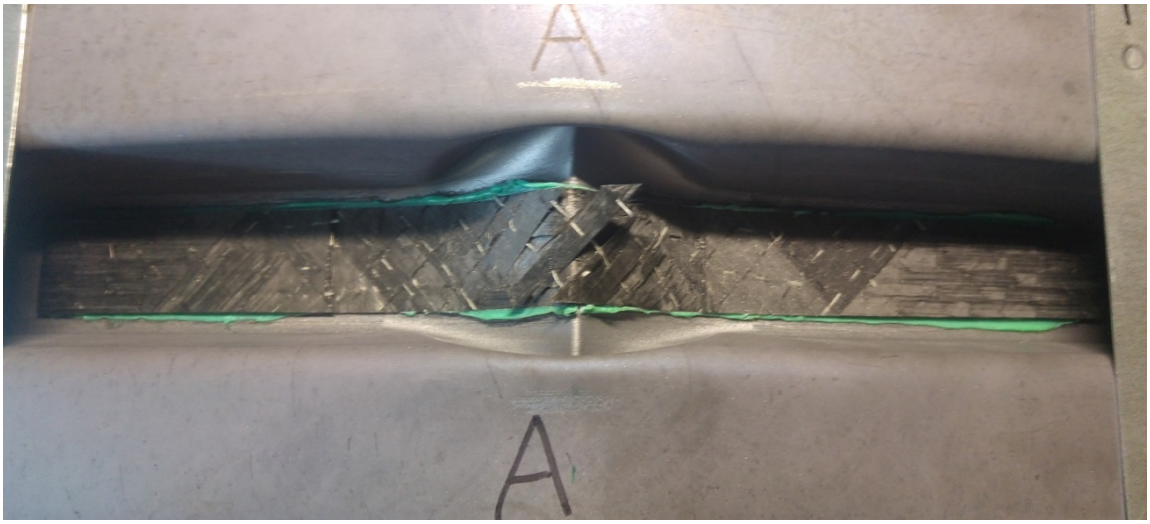

(a)

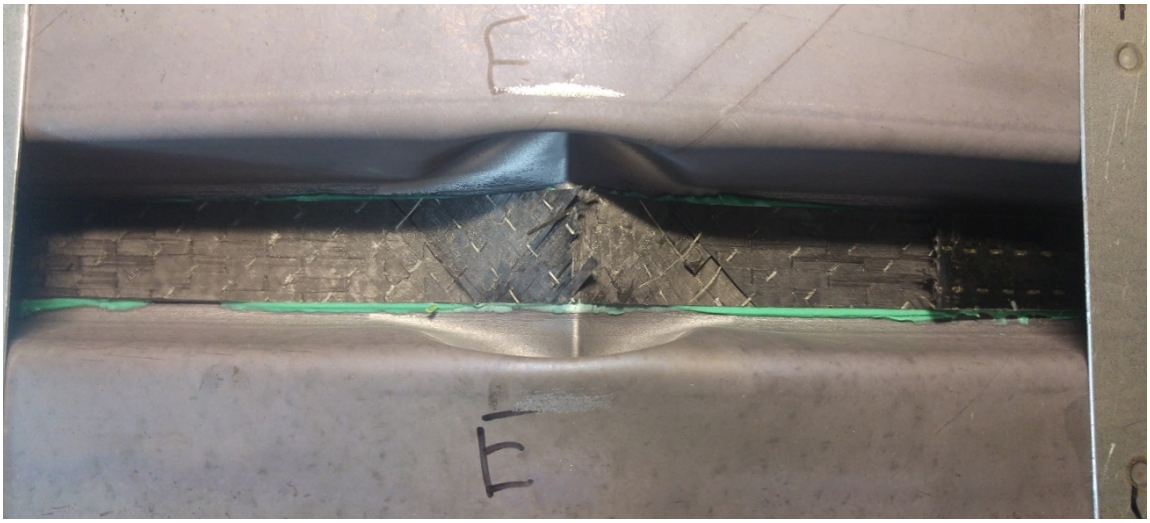

(b)

Figure 3.11: *Photo of the hat profile beam after the experiment with the delaminated pieces removed for both (a) test beam A and (b) test beam E.*

4 Developing and benchmarking the simulation model

In this section the process of obtaining the final model presented in Section 5 is described. Since the model needs to account for many different behaviours, various tests are run in order to determine how to model both the composite laminate as well as the glue and lamina interface. The delamination behaviour is of interest and therefore the general approach is to use one layer of elements for each ply. Element types are investigated in order to determine how to model each individual ply such that the behaviour is reasonable even after delamination, i.e when there is only one element through thickness. To capture the behaviour of the material, different composite material models are investigated and compared. Also the compatibility of the element types and composite materials is studied. To capture the delamination behaviour, both between the steel and composite parts and within the composite laminate, different types of adhesive modelling are tested. During the process, both the behaviour of the model and the simulation time is documented in order to get a model that gives a reasonable response for a justifiable computational cost.

4.1 Element types

This section describes the element types in LS-DYNA and the procedure of determine which types are suited for the current model. A simple bending test with a cantilever beam is performed with the different element types in order to rule out element types not giving a correct stiffness response. The setup of the test is presented in Figure 4.1. The fixed boundary was modelled using the boundary condition BOUNDARY_SPC(SET) with all degrees of freedom fixed. The applied displacement was imposed using the condition BOUNDARY_PRESCRIBED_MOTION, with a linear loading curve at velocity 0.05 m/s.

A short description of the element formulations used and the results of the cantilever bending test is presented under each subsection. For all simulations one layer of elements through thickness is used, since the intention is to model each ply with one layer in order to capture the delamination behaviour. Since solid elements usually are modelled with at least three elements through thickness, employing a configuration of one layer of elements through thickness will give the solid elements a disadvantage and the element type will most likely not perform as well as the shell elements [15]. The simulations to investigate the element formulations are performed to find the types and formulations that can perform well with one layer of elements through thickness, and no alterations in the mesh configuration is performed between simulations despite the different recommendations for different element types. Note that for the under-integrated elements hourglass control is recommended in order to prevent hourglass modes. The energy dissipating by the hourglass forces reacting against the formations of the hourglass modes is tracked and reported in the output file GLSTAT. [10]

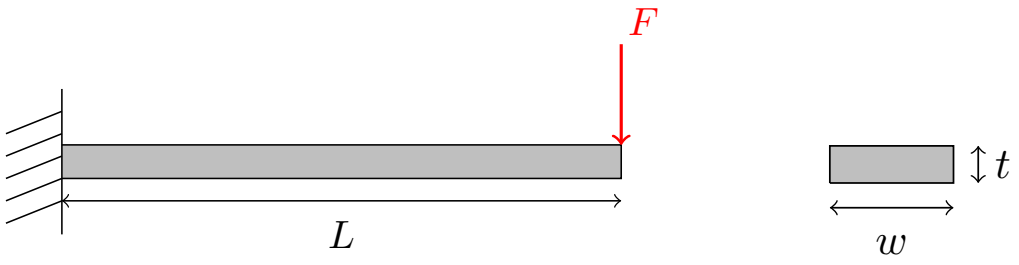

Figure 4.1: *A schematic figure of (a) the cantilever beam test setup, performed to test the stiffness response of the element types, and (b) the beam cross section. The length is referred to as L, the width as w and the thickness as t.*

The expected response is calculated according to Equation (4.1) [14] with the tip displacement δ, the Young's modulus E, the second moment of inertia I and the length L. This analytical solution is represented by a black line in the figures under each subsection. The mechanical and geometric properties for the cantilever beam are presented in Table 4.1. The mesh consists of 50 elements along the length, 7 elements along the width

and one element through thickness.

$$F = \frac{3EI}{L^3}\delta \tag{4.1}$$

Table 4.1: Mechanical and geometric properties for cantilever beam analysis

Property	**Value**	
E	132	GPa
L	150	mm
t	1.98	mm
w	20	mm

4.1.1 Solid elements

The solid element is a three-dimensional finite element that requires no simplifying geometry, constitutive, or loading assumptions. The boundary conditions are treated more realistic compared to shell or beam elements. This, however, comes at a high computational cost. Also, very important in this case, solid elements often has poor performance for thin-walled structures due to shear locking. Hexahedron elements are to be used if possible. The 8-noded hexahedron solid element is presented in Figure 4.2.

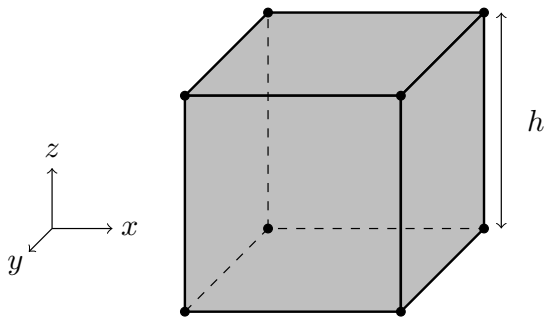

Figure 4.2: *Schematic figure of a 8-noded hexahedron solid element. The thicknesss of the element is marked with h.*

For hexahedron elements intended to model the composite there are five applicable element formulations in LS-DYNA; (i) constant stress element, (ii) fully integrated selectively reduced (S/R) element, (iii) fully integrated quadratic 8 node elements with nodal rotations, (iv) efficient element formulation for poor aspect ratio, and (v) accurate element for poor aspect ratio [16, 17].

(i) The constant stress element (ELFORM 1) is the default element in LS-DYNA. The element is underintegrated (has one integration point in the middle of the element), which allows for hourglass modes. The element formulation is efficient and accurate, and can be used for large deformations. Hourglass control type 6 is recommended as a supplement to avoid zero-energy modes. [16, 17]

(ii) The fully integrated selectively reduced (S/R) element (ELFORM 2) is has 8 integration points and therefore hourglass formation is not an issue. This element type is slower than the the constant stress solid element and is more unstable in large deformation applications. It is too stiff in many situations, especially for poor aspect ratios, where shear locking is a problem. [16, 17]

(iii) Fully integrated quadratic 8 node elements with nodal rotations (ELFORM 3) is an expensive element with quadratic interpolation between nodes. The element has 14 integration points, and 6 degrees of freedom in each of the 8 nodes. The element is not compatible with incompressible materials or simulations with plasticity. This element formulation is not generally recommended due to high computational cost. [16, 17]

(iv),(v) There are two element formulations for poor aspect ratio; one accurate formulation (ELFORM -2) and one efficient formulation (ELFORM -1). Both formulations are based on the fully integrated selectively reduced (S/R) element (ELFORM 2). They result in a slower simulation than ELFORM 2, but since they can handle poor aspect ratio without shear locking, it can still be the faster choice for thin structures since fewer elements are needed. The efficient formulation (ELFORM -1) needs to be supplemented by hourglass control. [16, 17]

The force-displacement relation obtained from the cantilever bending test is presented in Figure 4.3. The simulation times are listed in Table 4.2. It can be seen that ELFORM 1 behaves too softly in the cantilever beam analysis. Since the element has only one integration point through thickness and is modelled with only one element in this direction the behaviour is expected. The element formulation is excluded from further analysis. Since element formulation 2 over-predicts the stiffness substantially this element formulation is excluded as well. Element formulations -1 and -2 lies directly on top of each other, and since simulations using ELFORM -2 are substantially slower (three times slower than using ELFORM -1) this formulation is excluded. This means that ELFORM -1 and ELFORM 3 are still kept for further analysis.

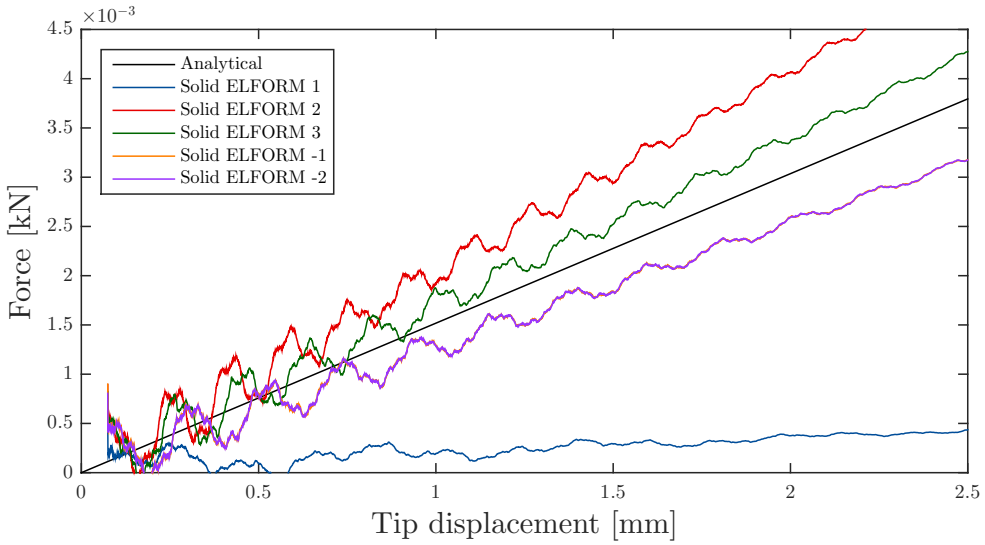

Figure 4.3: *The result from the cantilever beam bending test, where the following element types are tested; ELFORM 1 (blue), ELFORM 2 (red), ELFORM 3 (green), ELFORM -1 (orange) and ELFORM -2 (purple). The analytical result is represented by a black line. Note that the curve representing ELFORM -1 is covered by ELFORM -2.*

Table 4.2: The simulation time for the cantilever beam test with solid element formulations.

ELFORM	**Time [s]**	**Time step [ms]**
1	69	$1.96 \cdot 10^{-4}$
2	125	$1.96 \cdot 10^{-4}$
3	411	$1.96 \cdot 10^{-4}$
-1	149	$1.96 \cdot 10^{-4}$
-2	472	$1.96 \cdot 10^{-4}$

4.1.2 Thin-shell elements

The shell elements are two-dimensional elements based on a combination of plane stress assumptions and plate theory. This assumption is considered as reasonable for thin-walled structures [9]. The shell element describes the mid surface of the structure. A schematic figure of a thin-shell element is presented in Figure 4.4

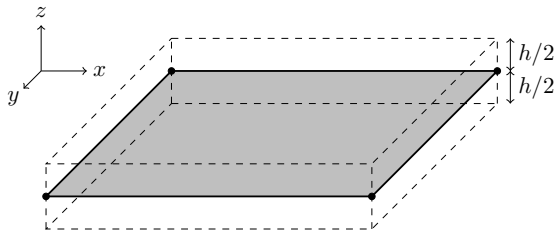

Figure 4.4: *Schematic figure of a thin-shell element, with the mid surface (gray) and the thickness offset $h/2$ (dashed).*

According to Stelzmann, 3-5 integration points (or more) per element are recommended for a non-linear material model. Only two of the available shell elements are recommended; (i) the Belytschko-Tsay element and (ii) the fully integrated shell element. The Belytschko-Tsay element is recommended for simulations that need to give results at low cost and the fully integrated element is recommended for higher accuracy. [17]

(i) Belytschko-Tsay (ELFORM 2) is a standard element with one point integration, and should according to Stelzmann be used with 3 through thickness integration points (NIP) and the hourglass control type 4 to avoid spurious zero energy modes. In CONTROL_SHELL it is recommended to use ISTUPD=4, BWC=1 and PROJ=1. [17]

(ii) The fully integrated element (ELFORM 16) is intended for use when accuracy is needed. Simulations using this element formulation are 2.5 times slower than the Belytschko-Tsay element. The formulation is recommended by Stelzmann to use with 5 through thickness integration points (NIP) and hourglass control type 8 to avoid spurious energy modes. In CONTROL_SHELL it is recommended to use ISTUPD=4. [17]

The result from the cantilever beam test is presented in Figure 4.5. The simulation times are listed in Table 4.3. From the simulations it can be seen that element formulations 2 and 16 performs almost equally well in predicting the force-displacement. Element formulation 16 takes approximately two times longer to run than element formulation 2 as can be seen in Table 4.3, which is close to the difference predicted by Stelzmann [17]. It is worth noting that the fully integrated thin-shell element (ELFORM 16) performs well in computational cost compared to the results for solid elements in Table 4.2 and the thick-shell elements in Table 4.4. It is also interesting to note that the time steps for the thin-shell elements are larger than the time step used for the solid elements in Table 4.2 and the thick-shell elements in Table 4.4. This indicates that the shell elements offer a substantially faster simulation when each time step takes longer time to evaluate (e.g. when the material model is changed from an elastic model to a composite model).

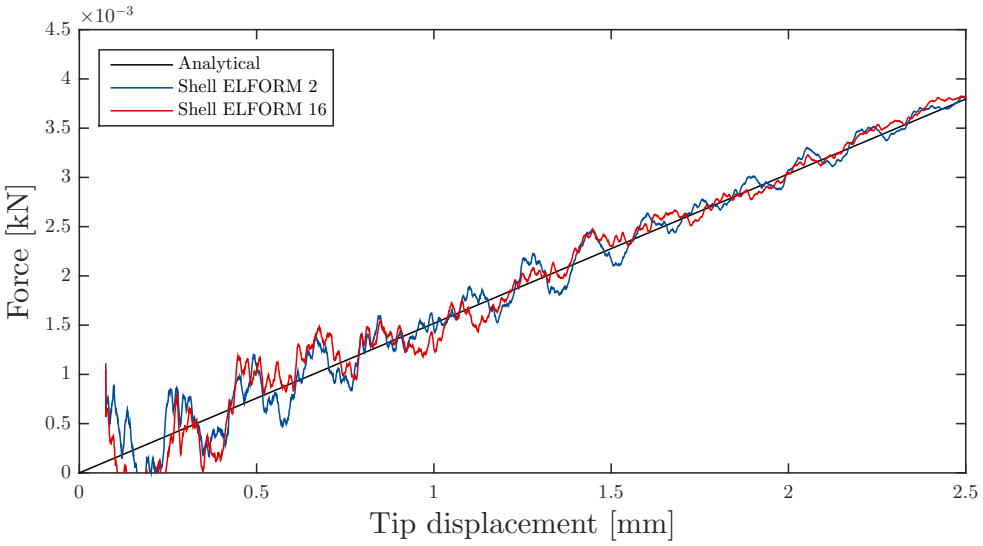

Figure 4.5: *The result from the cantilever beam bending test, where the following element types are tested; ELFORM 2 (blue) and ELFORM 16 (red). The analytical result is represented by a black line.*

Table 4.3: The simulation time for the cantilever beam test for thin-shell element formulations.

ELFORM	**Time [s]**	**Time step [ms]**
2	46	$3.32 \cdot 10^{-4}$
16	87	$3.32 \cdot 10^{-4}$

4.1.3 Thick-shell elements

The thick-shell element is an 8-noded element based on shell theory but with an added strain component through thickness [10]. The element has 8 corner nodes according to Figure 4.6.

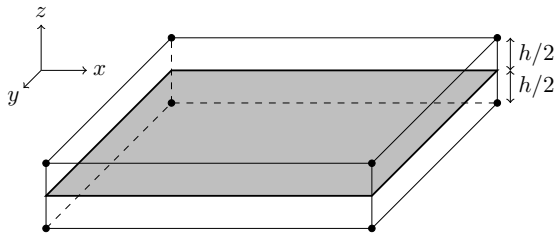

Figure 4.6: *Schematic figure of a thick-shell element, with the mid surface (gray) and the thickness offset* $h/2$.

In LS-DYNA there are four types of thick-shell elements; (i) one point reduced integration, (ii) selectively reduced 2x2 in plane integration, (iii) assumed strain 2x2 in plane integration, and (iv) assumed strain reduced integration. [17]

(i) The one point reduced integration element (ELFORM 1) is a plane-stress formulation, like a thin-shell element and has one in-plane integration point. The thickness stiffness is modelled by a penalty function between the top and bottom nodes, and thickness changes are imposed by the membrane strain as for a regular thin-shell element. The element formulation can behave too softly and hourglass modes are possible. [17]

(ii) The selectively reduced 2 x 2 in plane integration formulation (ELFORM 2) is a fully integrated element formulation with a plane-stress assumption. The thickness stiffness is modelled by a penalty function between the top and bottom nodes, and thickness changes are imposed by the membrane strain as for a regular thin-shell element. The accuracy of the element is comparable to the Belytschko-Tsay thin-shell element, but it is 7-8 times more expensive. [17]

(iii) The assumed strain 2 x 2 in plane integration formulation (ELFORM 3) is a 3D formulation like a solid element and the thickness changes are imposed by the out-of-plane stress. The formulation is slow (approximately 65 times slower than the Belytschko-Tsay thin-shell element), and at least two elements in the thickness direction are needed for an accurate result in bending simulations. [17]

(iv) The assumed strain reduced integration (ELFORM 5) is a 3D formulation like a solid element and the thickness changes are imposed by the out-of-plane stress. The element formulation is developed to model thick composites with the option of including laminate shell theory. The element formulation is fast, approximately 1.5 times slower than the Belytschko-Tsay thin-shell element and the formulation can handle bending simulation with only one element through thickness. Hourglass modes and shear locking are stabilised using an assumed strain method. [17]

The result from the cantilever bending test is presented in Figure 4.7 and the simulation times are presented in Table 4.4. It can be seen that element formulation 3 is the slowest of the thick shells, just as stated by Stelzmann [17]. The setup in the simulation only uses one element through thickness, and for element formulation 3 it is recommended to use at least 2 elements through thickness. This could explain the inaccurate results for this element type. Since it is both extremely slow and inaccurate this element formulation is left out from further analysis. Element formulations 1, 2 and 5 are equally good at predicting the force-displacement, and since neither of the element formulations are exceptionally slow all 3 formulations are kept for further analysis. ELFORM 5 is the least costly of the three formulations and therefore becomes the preferred choice. It can also be seen that the time steps in the simulations are larger for the shell-type elements (thick-shell ELFORM 1 and 2) compared to the time steps for the solid-type elements (thick-shell ELFORM 3 and 5). As for the case when comparing thin-shell elements and solid elements.

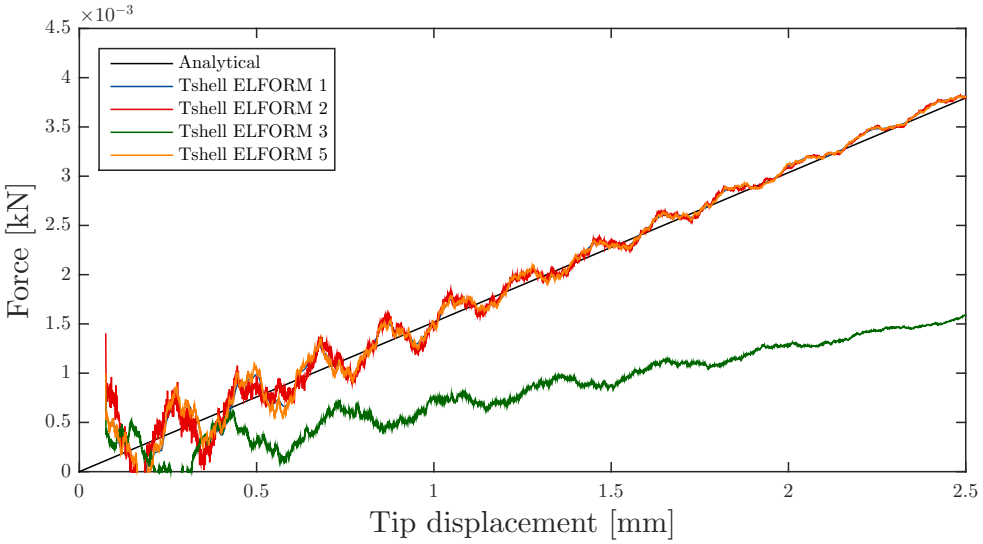

Figure 4.7: *The result from the cantilever beam bending test, where the following element types are tested; ELFORM 1 (blue), ELFORM 2 (red), ELFORM 3 (green) and ELFORM 5 (orange). The analytical result is represented by a black line.*

Table 4.4: The simulation time for the cantilever beam test for thick-shell element formulations.

ELFORM	Time [s]	Time step [ms]
1	96	$2.3 \cdot 10^{-4}$
2	248	$2.3 \cdot 10^{-4}$
3	1069	$1.96 \cdot 10^{-4}$
5	79	$1.96 \cdot 10^{-4}$

4.1.4 Brief conclusion

From the result of the cantilever beam test it can be concluded that the most efficient element formulations, based on the stiffness response and simulations time, are solid ELFORM 3, thin-shell ELFORM 2, and thick-shell ELFORM 5. These three formulations are used as a starting point for the subsequent simulations. Note that the performed tests simply provides information about the stiffness response and the simulation time. The results may therefore only be considered a suggestion of which element formulation that are suitable for modelling the plies of the composite laminate. If there are indications of the element types not giving a reliable response in any further analysis, e.g. hourglass modes, the formulation will be changed into any of the other remaining suitable formulations.

4.2 Composite material models in LS-DYNA

The material data used in the material cards is specified in a report from Bru et al [12] and is listed in Section 3.1. Since the material used in the experiment is a well characterised composite material, most physical parameters are available. However, if the data is not available for any of the material cards, the parameters are estimated based on the data from these given material properties.

In LS-DYNA there are several material models for composites available. These differ in the failure criteria used and the type of elements accepted. The composite material models applicable for the modelling are described further below.

MAT22 MAT_COMPOSITE_DAMAGE
Failure criterion: Chang-Chang, found in Appendix C.1.
Element types accepted: Thin-shell, Thick-shell, Solid
The material card represents an orthotropic material with an optional brittle failure. [18]

MAT54/55 MAT_ENHANCED_COMPOSITE_DAMAGE
Failure criterion (54): Chang-Chang, found in Appendix C.1.
Failure criterion (55): Modified Tsai-Wu and Chang-Chang, found in Appendices C.2 and C.1
Element types accepted: Thin-shell, Thick-shell, Solid
An enhanced version of MAT22. The model contains a crashfront algorithm, meaning that once an element has failed it is deleted and the strength of surrounding element is reduced according to a stated parameter. [18]

MAT58 MAT_LAMINATED_COMPOSITE_FABRIC
Failure criterion: Modified Hashin, found in Appendix C.3. [18]
Element types accepted: Thin-shell, Thick-shell [18]
Material model to represent UD and woven composites as well as complete laminates. [18]

MAT261 MAT_LAMINATED_FRACTURE_DAIMLER_PIHNO
Failure criterion: Pinho, found in Appendix C.4.
Element types accepted: Thin-shell, Thick-shell, Solid
The failure criteria of this model is physically based for all failure modes. It is a continuum damage model and includes non-linear in-plane shear behaviour. [18]

MAT262 MAT_LAMINATED_FRACTURE_DAIMLER_CAMANHO
Failure criterion: Camanho, found in Appendix C.5.
Element types accepted: Thin-shell, Thick-shell, Solid
The failure criteria of this model is physically based for all failure modes. It is a continuum damage model and includes a simplified non-linear in-plane shear behaviour. [18]

4.2.1 Stiffness response

With the aim to detect if any of the composite material cards have a different and unwanted behaviour, a cantilever beam test was performed for the different material cards. The setup of the test is identical to the one described in Section 4.1. For this test, the given material properties are not used. Instead, the composite material card was implemented to mimic an isotropic elastic material, i.e. with the same material parameters in all directions and with the failure parameters set to values large enough such that failure will not occur (e.g. $X_c = 1000$ GPa). The results are then compared with the response of the pure elastic material in the previous cantilever beam test. The result is presented separately for each element type.

4.2.1.1 Solid elements

In Figure 4.3 and Table 4.2 it can be seen that the fully integrated quadratic 8 node element with nodal rotations (ELFORM 3) gives a good force-displacement response with a reasonable simulation time. This element is therefore used when implementing the different material models. The force-displacement curves for the different materials are compared with the pure elastic material in Figure 4.8. The stiffness response is identical to the elastic material for all the material models.

The simulation times are listed in Table 4.5. It can be seen that all material models increase the simulation time, but not the time step. This means that each individual step is slower for the composite material model than for the isotropic elastic material, just as anticipated. The simulation time differs between the material models, where the simplest model (MAT22) has the shortest simulation time, while MAT261 has the largest computational cost. This is expected due to the complexity of the models.

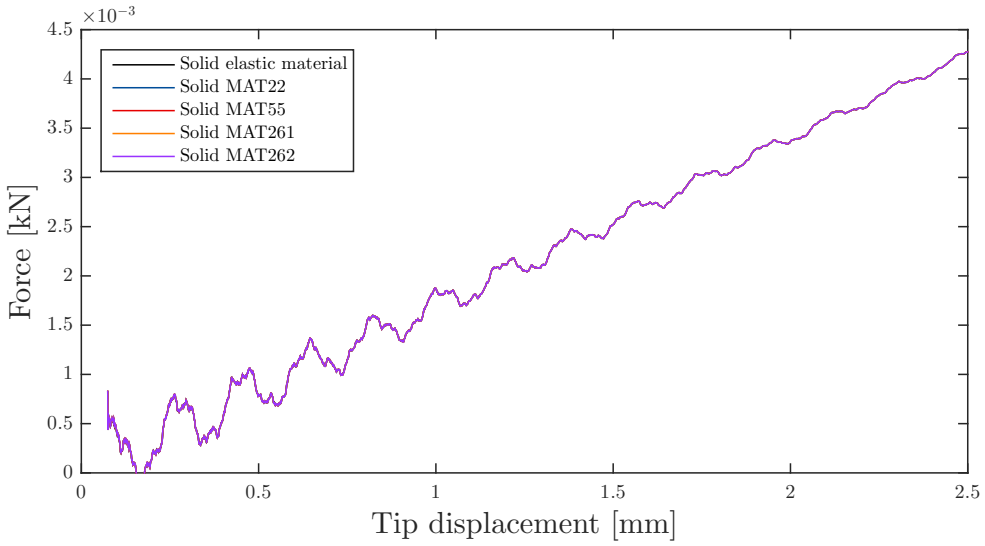

Figure 4.8: *A comparison of the response of the material models in the cantilever bending test. The lines represent the pure elastic material (black), MAT22 (blue), MAT55 (red), MAT261 (orange) and MAT262 (purple).*

Table 4.5: The simulation time for the cantilever beam test for solid elements and composite material models.

Material model	**Time [s]**	**Time increase from reference [%]**	**Time step [ms]**
Elastic	*411*	-	$1.96 \cdot 10^{-4}$
22	588	43	$1.96 \cdot 10^{-4}$
55	661	60	$1.96 \cdot 10^{-4}$
261	1523	270	$1.96 \cdot 10^{-4}$
262	868	111	$1.96 \cdot 10^{-4}$

4.2.1.2 Thin-shell elements

In Figure 4.5 and Table 4.3 it can be seen that the fully integrated shell element (ELFORM 16) gives a good force-displacement response for a reasonable simulation time. This element is therefore used when implementing the different material models. The force-displacement curves for the different material models are compared with the pure elastic material in Figure 4.9. It can be seen that for the lower displacements, MAT262 exhibits a larger magnitude of the force oscillations. As the displacement increases this behaviour settles and all material models behave similarly.

The simulation times and time step sizes are compared with the reference case (elastic material model) in Table 4.6. The time step is decreased for the composite material models MAT22, MAT58, MAT261 and MAT262, which implies a higher computational cost. For material model MAT55 the time step is of the same size as for the elastic reference material, but still the simulation time is large. This suggests that each step is computationally heavy, but that the model is more stable than the other composite material models.

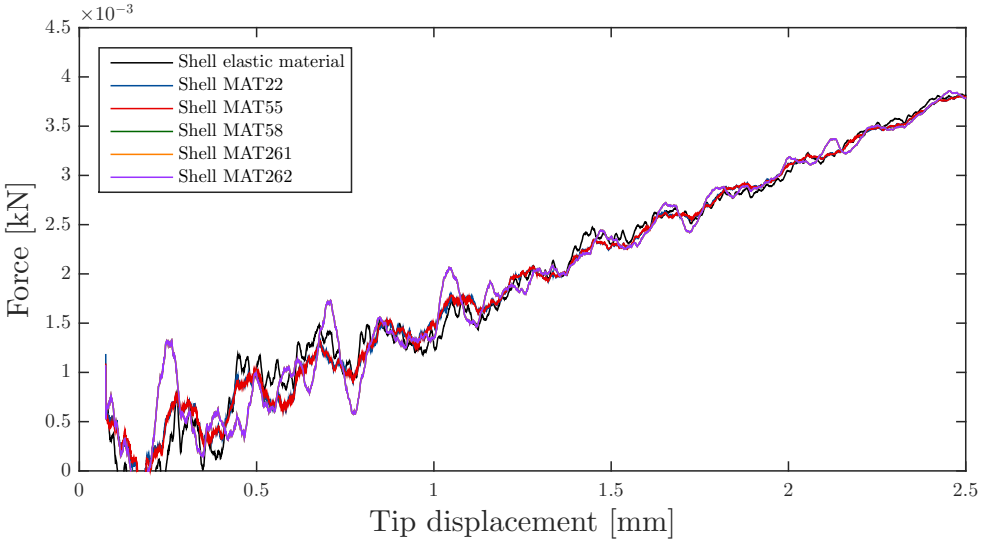

Figure 4.9: *A comparison of the response of the material models in the cantilever bending test. The lines represent the pure elastic material (black), MAT22 (blue), MAT55 (red), MAT58 (green), MAT261 (orange) and MAT262 (purple). Note that MAT58, MAT261 and MAT262 exhibit the same behaviour, and therefore MAT58 and MAT261 are hidden behind MAT262 in the figure.*

Table 4.6: The simulation time for the cantilever beam test for thin-shell elements and composite material models.

Material model	**Time [s]**	**Time increase from reference [%]**	**Time step**
Elastic	*87*	-	$3.32 \cdot 10^{-4}$
22	120	38	$3.0 \cdot 10^{-4}$
55	154	77	$3.32 \cdot 10^{-4}$
58	269	209	$3.0 \cdot 10^{-4}$
261	78	359	$3.0 \cdot 10^{-4}$
262	190	118	$3.0 \cdot 10^{-4}$

4.2.1.3 Thick-shell elements

In Figure 4.7 and Table 4.4 it can be seen that the assumed strain reduced integration formulation (ELFORM 5) gives a reasonable force-displacement response with the shortest simulation time. This element is therefore used when implementing the different material models. The force-displacement curves for the different materials are compared with the pure elastic material in Figure 4.10. It can be seen that all material models behave very similarly for the thick-shell elements.

The simulation times are compared with the reference case (elastic material model) in Table 4.7. In the table it can be seen that the time step is not changed for any of the material models. Still, for all models the simulation time has increased. For the thick-shell elements the increase is generally not as large as for the solid and thin-shell elements in Table 4.5 and Table 4.6, and the reference time is the lowest of the three as well. This indicates that from a computational cost aspect the thick-shell element is well suited for composite materials. Note that the time step for MAT58 is not comparable to the time steps of the other material models since the time step sizes for the elastic case using thick-shell ELFORM 1 and ELFORM 5 are not the same.

Table 4.7: The simulation time for the cantilever beam test for thick-shell elements and composite material models. *Note that MAT58 is run with ELFORM 1 and not ELFORM 5. ** The elastic case for ELFORM 1 is used as reference case.

Material model	**Time [s]**	**Time increase from reference [%]**	**Time step**
Elastic	*79*	-	$1.96 \cdot 10^{-4}$
22	108	37	$1.96 \cdot 10^{-4}$
55	124	77	$1.96 \cdot 10^{-4}$
58*	139	45**	$2.08 \cdot 10^{-4}$
261	266	177	$1.96 \cdot 10^{-4}$
262	130	86	$1.96 \cdot 10^{-4}$

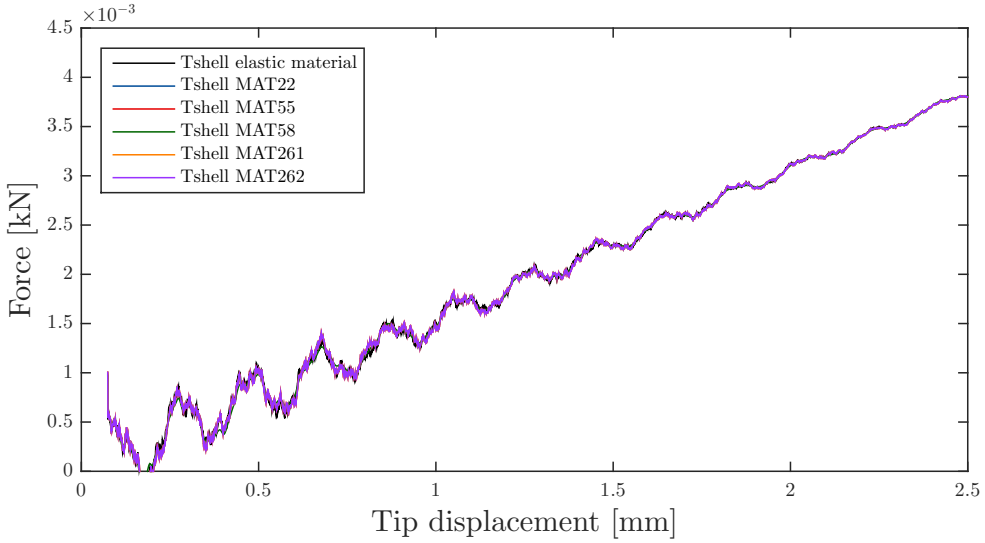

Figure 4.10: *A comparison of the response of the material models in the cantilever bending test. The lines represent the pure elastic material (black), MAT22 (blue), MAT55 (red), MAT58* (green), MAT261 (orange), and MAT262 (purple). *Note that MAT58 is run with ELFORM 1 and not ELFORM 5*

4.2.2 Behaviour at failure

The failure behaviour of the material models is investigated by a simply supported three point bending test, where the specimen is bent until failure with the aim of eliminating combinations of material models and element types that behave in an unreasonable way. The setup of the test is illustrated in Figure 4.11, where a displacement is applied to the middle of the beam. The supports are modelled using boundary conditions (BOUNDARY_SPC(SET)), and the mesh consists of 50 elements in the length direction, 7 in the width direction and 1 element through the thickness. The geometric parameters used in the three point bending to failure are presented in Table 4.8, together with the material data used for the analytical calculations. The displacement is increased linearly until failure occurs, with a velocity of 0.05 m/s, and imposed using a boundary condition (BOUNDARY_PRESCRIBED_MOTION). The parameters of the material models are listed and described in Appendix A. Identical tests with the same mesh sizes are performed for all applicable material models, for solid, thin-shell, and thick-shell elements. Note that the strain failure is captured using the ADD_EROSION card.

To give an indication of the performance in both longitudinal and transversal directions of the material model, the bend to failure is simulated for both fibre angles $\theta = 0°$ and $\theta = 90°$. At failure, the displacement and the corresponding applied force is compared with analytical results in order to verify the accuracy of the analysis. Note that the analytical force/displacement is not an accurate result, but gives an indication of the order of magnitude of the results. A failure at a force or displacement very far from the analytical result is considered as incorrect. In the analytical solution the material is assumed to be isotropic elastic with the mechanical properties taken from the desired fibre angle (i.e. $E_{11}/X_c/\varepsilon_{11cu}$ and $E_{22}/Y_t/\varepsilon_{22tu}$ respectively). In the analytical calculations, the failure may be initiated due to reaching the maximally permitted strain or stress.

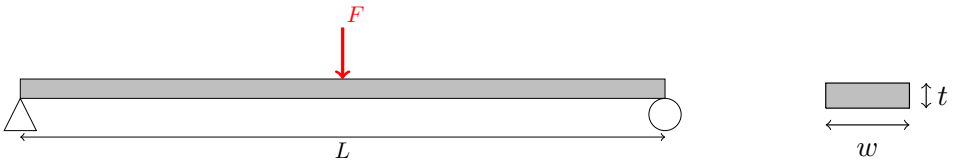

(a) (b)

Figure 4.11: *A schematic figure of (a) the three point bending test setup, performed to test the failure of the matrial models, and (b) the beam cross section. The length is referred to as L, the width as w and the thickness as t.*

Table 4.8: Mechanical and geometric properties for the three point bending analysis

Property	**Value**			
L	150 mm			
t	1.98 mm			
w	20 mm			
	0°		**90°**	
E	132	GPa	9	GPa
ε_{max}	0.49	%	0.32	%
σ_{max}	631	MPa	29.2	MPa

The force and displacement at failure in the bending test are estimated by an elementary case where the maximal stress and the maximum bending moment for an applied force, $M_{max} = \frac{FL}{4}$ and $\sigma_{max} = \pm\frac{6M_{max}}{wt^2}$, are combined to obtain the maximal force of the beam, see Equation (4.2). [19]

$$F_{max,stress} = \frac{2\sigma_{max}wt^2}{3L} \tag{4.2}$$

The displacement $\delta_{max,stress}$ corresponding to the force to failure $F_{max,stress}$ is calculated from an elementary case, see Equation (4.3). [14]

$$\delta_{max,stress} = \frac{F_{max}L^3}{48EI} = \{\text{insert } F_{max,stress} \text{ and } I\} = \frac{\sigma_{max}L^2}{6Et} \tag{4.3}$$

With the (incorrect) assumption of isotropic, elastic material Hooke's law is used to replace the maximum stress with the maximum strain in Equation (4.2) and Equation (4.3). [14]

$$F_{max,strain} = \frac{2E\varepsilon_{max}wt^2}{3L} \tag{4.4}$$

$$\delta_{max,strain} = \frac{\varepsilon_{max}L^2}{6t} \tag{4.5}$$

The analytical solution is presented in Table 4.9.

Table 4.9: The analytically obtained displacement and force at failure for both a ply with fibre angle 0° (fibres along the length of the beam) and with fibre angle 90° (fibres along the width of the beam).

Failure mode	$\theta = \mathbf{0}°$	$\theta = \mathbf{90}°$
Stress	$F = 224.4$ [N] $\delta = 9.0$ [mm]	$F = 10.4$ [N] $\delta = 6.1$ [mm]
Strain	$F = 150.2$ [N] $\delta = 6.0$ [mm]	$F = 15.7$ [N] $\delta = 9.2$ [mm]

4.2.2.1 Solid elements

The displacement and force at failure for the different material models, when modelling using solid elements, are listed in Table 4.10. All material models give reasonable failure responses compared to the analytical result. However, the result of material model MAT22 differs for the 90° ply from the remaining materials. This indicates that this material model should not to be used with this element type.

Table 4.10: The displacement and force, for the different composite material models, at failure in a bending test using solid elements.

Material	δ_{0° **[mm]**	$\mathbf{F}_{0^\circ}$ **[N]**	δ_{90° **[mm]**	$\mathbf{F}_{90^\circ}$ **[N]**
MAT22	10.8	275	6.16	12.7
MAT55	10.7	274	12.06	19.7
MAT261	10.7	274	11.05	18.6
MAT262	10.8	276	10.73	17.5

4.2.2.2 Thin-shell elements

The displacement and force at failure for the different material models, when modelling using thin-shell elements, are listed in Table 4.11. The results of the bending test for MAT262 differs significantly from both the analytical solution and the results of the remaining material models, for the 0° ply. This indicated that thin-shell elements are not compatible with this material model. The material models MAT22 and MAT58 exhibit failure prior to the remaining models for the 90° ply, which also suggests on an inaccuracy of the combination of the element types and material models.

Table 4.11: The displacement and force, for the different composite material models, at failure in a bending test using thin-shell elements.

Material	δ_{0° **[mm]**	$\mathbf{F}_{0^\circ}$ **[N]**	δ_{90° **[mm]**	$\mathbf{F}_{90^\circ}$ **[N]**
MAT22	8.1	141.1	7.76	13.3
MAT55	9.6	196.0	11.23	17.2
MAT58	9.7	237.5	8.27	14.1
MAT261	9.7	170.4	11.00	16.7
MAT262	3.6	86.4	11.22	17.1

4.2.2.3 Thick-shell elements

The displacement and force at failure for the different material models, when modelling using thick-shell elements, are listed in Table 4.12. The combination of thick-shell elements and the material model MAT55 resulted in an unrealistic displacement, and no failure was initiated. This implies that thick-shell elements and MAT55 are not compatible. All remaining material models give reasonable response. However, like for the thin-shell elements the material models MAT22 and MAT58 exhibit failure prior to the remaining models for the 90° ply. Note that MAT58 is not compatible with thick-shell elements of formulation ELFORM 5. These results are instead obtained using ELFORM 1.

Table 4.12: The displacement and force, for the different composite material models, at failure in a bending test using thick-shell elements. ⋆Note that MAT58 is run with ELFORM 1 and not ELFORM 5

Material	δ_{0° **[mm]**	$\mathbf{F}_{0^\circ}$ **[N]**	δ_{90° **[mm]**	$\mathbf{F}_{90^\circ}$ **[N]**
MAT22	11.5	283	7.89	13.1
MAT55	-	-	-	-
MAT58⋆	11.1	272	8.4	13.8
MAT261	11.3	279	11.96	20.2
MAT262	11.3	279	11.78	16.8

4.2.3 Brief conclusion

MAT22 and MAT58 exhibit lower values of the displacement and force at failure for 90° for all element types (except for the combination of MAT58 and solid elements, since this combination is not compatible). However, this is not the case for the 0° ply.

Two different combinations are considered not compatible based on these results; solid elements combined with MAT22 and thin-shell elements together with MAT262 exhibit significantly difference failure values than the remaining combinations. From the analysis it can also be concluded that MAT55 does not work as intended with thick-shell ELFORM 5.

Note that all material models except MAT261 and MAT262, have unphysical parameters that need calibration. This tuning has not been performed and some results may therefore be misleading. However, since MAT261 and MAT262 are based on physical data, these models are the preferred choice since a new material can be implemented without tuning and estimations (if all physical parameters are known). Both MAT261 and MAT262 behave reasonably in these simulations and therefore they have a great advantage over the other models. MAT262 gives these results at a lower computational cost than MAT261, and is therefore considered the best choice of material model when taking both accuracy and computational cost into account.

4.3 Adhesive modelling

In order to capture the delamination behaviour of the simulation model, some sort of adhesive modelling is required both between the steel and the composite laminate, and between the plies of the laminate. In LS-DYNA, there are two available approaches; *tiebreak contact condition* and *cohesive zone*. The first option is a contact condition which as the name reveals ties the parts together and then breaks the contact at a given condition. The cohesive zone consists of a certain type of solid elements, that is implemented between the parts and fails at a given condition. In this section, these adhesive modelling approaches are further described and a comparison between them is conducted. The results are presented separately for each element type. As described in Section 2.1.3, the delamination may occur in three different modes. Two of these, mode I and mode II, are of interest for the adhesive modelling, and will be investigated by a double cantilever beam (DCB) test and an end notched flexure (ENF) test respectively.

4.3.1 Tiebreak contact condition

The tiebreak condition is a contact condition which allows for separation according to an optional failure criteria between the two bodies in contact. The contact is penalty based, and no sliding is allowed between the included elements. The tiebreak conditions in LS-DYNA are contact conditions that transfer both tensile and compressive forces, unlike standard contact conditions that only transfer compressive forces. The tiebreak conditions also contain a failure criterion, and when the condition is met the bodies no longer remain in contact. The failure criteria in the tiebreak contact condition only includes the force/stress to failure. This means that no energy is considered in the failure, and this is not considered as a physically correct model. [20]

The tiebreak contact condition AUTOMATIC_SURFACE_TO_SURFACE_TIEBREAK is used in the simulations. The contact is described in Appendix B. In order to determine the behaviour of the tiebreak condition in combination with different element types, separate simulations with solid, thin-shell and thick-shell elements are run.

4.3.2 Cohesive zone modelling

When using a cohesive zone to model the crack propagation, cohesive elements are implemented between the layers. The nodes of the cohesive elements are merged with the nodes of the adjacent plies. The element may be regarded as nonlinear springs, representing the behaviour of the adhesive [21], see Figure 4.12a. A zero thickness is allowed, inducing a two dimensional behaviour. Instead of strains, the deformation is modelled by the relative displacement between the two surfaces interpolated to the Gauss points. The force per unit area corresponding to the displacement is determined by a cohesive material model in shape of a traction-separation curve for each mode. This governs the behaviour of the element. When the separation at failure is reached (i.e. the traction is 0 for a non-zero separation), the element is eroded.

There are a few cohesive elements in LS-DYNA, all of them are solid elements, since two nodes through the thickness are required in order to not lock the two bodies together in the same node. As stated earlier,

LS-DYNA allows for cohesive elements without thickness, meaning that solids can be modelled with initial contact with an adhesive between the two bodies (if $d = 0$). The configuration of a cohesive element between two solids is shown with a thickness d in Figure 4.12c. For thin-shells the cohesive element spans from the mid surfaces as can be seen in Figure 4.12b. [22]

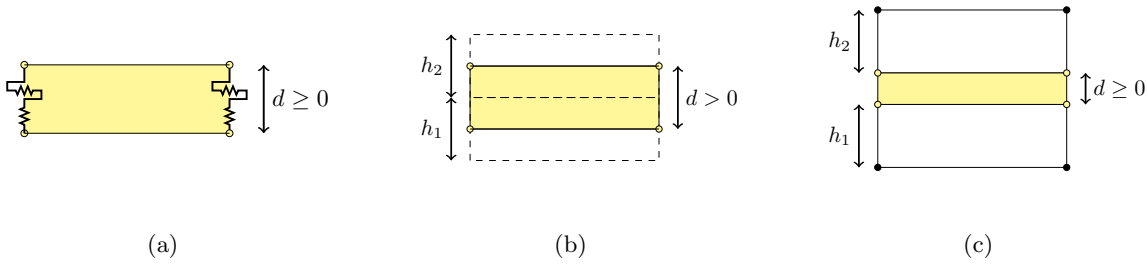

(a) (b) (c)

Figure 4.12: *A schematic figure of (a) 2-dof spring configuration of a cohesive element (yellow) and how it may be used for connecting both (a) thin-shell elements and (b) solid or thick-shell elements. Note that the cohesive element may have a thickness $d = 0$, meaning initial contact between the solid or thick-shell elements. The structure of the cohesive element consists of vertical and horizontal springs, corresponding to mode I and mode II respectively. Figures reproduced and altered from* Adhesives modelling with LS-DYNA: Recent developments and future work *[22].*

In LS-DYNA the solid elements ELFORM 19 and ELFORM 20 are intended for use with cohesive material models. Element formulation 19 defines the traction in the mid surface as the mid points between the nodes, and the element has four integration points. The element accepts an initial volume of zero, meaning that it can be used for adhesive bonding between solid elements. ELFORM 20 is identical but has offsets for shells. Note that there is an additional cohesive material card, MAT169 MAT_ARUP_ADHESIVE, that is intended for adhesive bonding in aluminium structures and can be used with other types of elements than ELFORM 19 and ELFORM 20. [1]

MAT138 MAT_COHESIVE_MIXED_MODE
Damage in the interface is considered in this model using irreversible conditions. [23]

MAT184 MAT_COHESIVE_ELASTIC
Simple cohesive model with three stress outputs instead of the usual six. [23]

MAT185 MAT_COHESIVE_TH
Tri-linear traction-separation law. Three stress outputs instead of the usual six. [23]

MAT186 MAT_COHESIVE_GENERAL
Arbitrary traction separation law. Damage of the interface is considered in this model using irreversible conditions. [23]

For the cohesive elements, the material type MAT186 is used due to it allowing an arbitrary traction separation law. Since all data for the material card is provided the general cohesive model is used. The material data has been supplied by Gestamp HardTech for the glue, and from Bru et al. [12] for the composite interface. This configuration allows for both movement without failure and separation at failure.

4.3.3 DCB test

The double cantilever beam (DCB) test is intended to investigate the delamination behaviour of mode I. This test consists of a specimen with an initial crack with length a_0. On each side of the opening there is a force (F) opening the crack, with equal size of both sides, see Figure 4.13. The forces are added using an applied displacement in the end nodes using BOUNDARY_PRESCRIBED_MOTION. The fixed edge is implemented using BOUNDARY_SPC(SET) with all degrees of freedom fixed. The parameters for the simulations are presented in Table 4.13, and the results obtained for the different configurations are compared to the force-displacement curve in Figure 4.14.

In the tests an elastic model with the longitudinal stiffness of the composite is used, and the properties

used together with the measurements presented in Table 4.13. Each lamina ply is modelled with one layer of elements through thickness and each element is 1×1 mm, i.e. a total of 20×150 elements in each ply. This mesh, including dimensions and mesh refinement, is based on a report from Turon et al. In the Turon et al. report it can be seen that the performance of the cohesive elements is heavily mesh dependent, and since no mesh convergence study is performed a mesh already concluded to give accurate results at a reasonable computational cost is chosen. [24]

Table 4.13: Material properties and measurements for the DCB simulations.

Property	**Value**	
E	132	GPa
ν	0.3	
ρ	1.5	g/cm^3
G_{IC}	149	J/m^2
Y_t	29.2	MPa
L	150	mm
a_0	58	mm
t	1	mm
w	20	mm

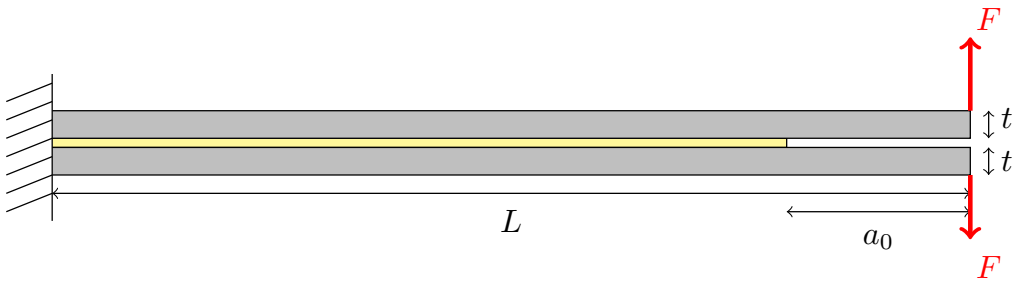

Figure 4.13: *Schematic figure of Mode I/DCB test. The two plies (grey) with length L, thickness t and w are pulled apart by two forces F (red). Between the plies are an adhesive (yellow) and an initial opening of length* a_0.

To predict the behaviour of the crack growth along the interface, an analytical solution is calculated. The analytical solution of the DCB test is divided into two parts; (i) before the crack grows and (ii) during the crack growth. The calculations are based on an elementary case, see Equation (4.6) where a is the crack size, E the Young's modulus and I the second moment of inertia [14]. The crack size is determined according to Equation (4.7). The crack starts to grow when the energy release (G_I) reaches the critical value (G_{IC}) [25]. The behaviour according to the hand calculations, with the properties for the DCB simulations described above, is presented in Figure 4.14. The force at initial crack propagation is approximately 14 N at a tip displacement of just above 4 mm.

$$F = \frac{3EI}{a^3}\delta \tag{4.6}$$

$$a = \begin{cases} a_0 & \text{(i)} \\ \left(\frac{9EI\delta^2}{wG_{IC}}\right)^{1/4} & \text{(ii)} \end{cases} \tag{4.7}$$

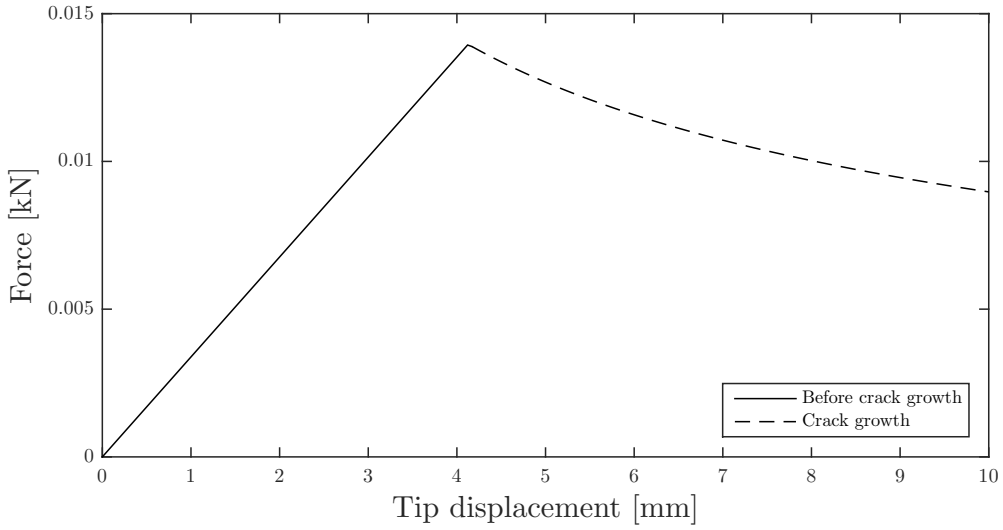

Figure 4.14: *The force-displacement relation for the analytic Mode I/DCB calculations.*

In the analysis for the different element types, the fracture zone is modelled using either a tiebreak contact condition (using Y_t as failure condition) or a cohesive zone (using both G_{IC} and Y_t as failure condition). The two beams are modelled using an elastic material model (MAT1). The configurations are simulated for solid, thin-shell, and thick-shell elements and the results are presented for each element type separately.

4.3.3.1 Solid elements

The force-displacement relation obtained in the DCB test, when modelling using solid elements, is presented in Figure 4.15. Both the tiebreak condition and the cohesive zone are included, as well as the analytical solution. It can be seen that both adhesive modelling methods exhibit the desired behaviour. However, the curve representing the cohesive zone simulation demonstrates a more stable behaviour that is similar to the analytical solution. The tiebreak condition exhibits larger drops in force during the crack propagation process, which could be an indication that the contact is released, i.e. the criteria is met, for a large area simultaneously. The magnitude of force that is required to initiate crack growth for the tiebreak condition is significantly lower than the analytically predicted force. This is something that could be solved by tuning the parameters in the contact card, but since a parameter that requires tuning is undesirable this is considered as a drawback of the solid element - tiebreak condition combination. For both simulations the response is stiffer than in the analytical case. This comes from using ELFORM 3, which in Figure 4.3 is shown to be overly stiff.

Although the cohesive zone modelling comes at a higher computational cost, see simulation times listed in Table 4.14, the cohesive zone is the preferred method based on the obtained response.

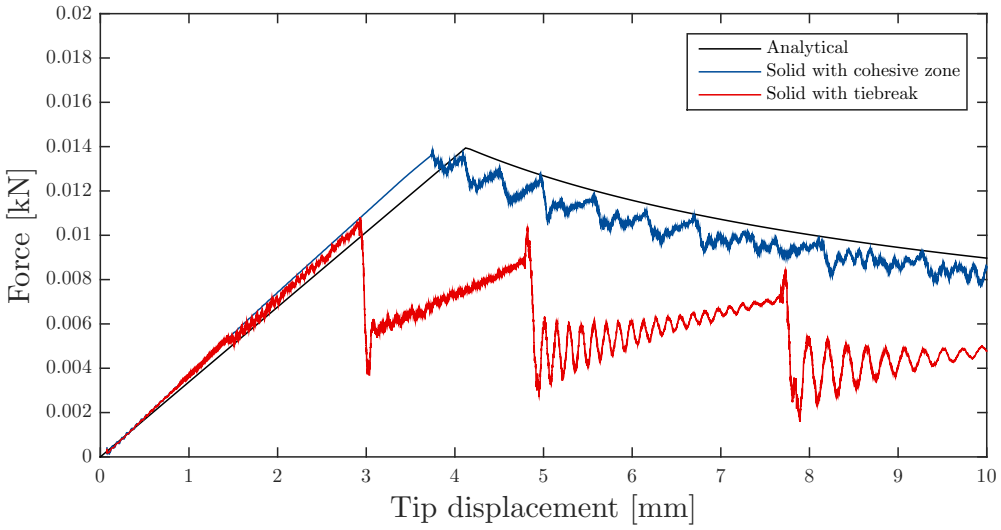

Figure 4.15: *Comparison of the force-displacement relation for the DCB/Mode I simulations with cohesive elements and tiebreak condition as adhesive model for the solid element formulation.*

Table 4.14: Simulation times for the DCB test when modelling with solid elements.

Adhesive model	**Time [s]**
Cohesive zone	10596
Tiebreak condition	7628

4.3.3.2 Thin-shell elements

The force-displacement relations for the modelling using thin-shell elements are presented and compared to the analytical result in Figure 4.16. The configuration with the cohesive zone exhibits a reasonable behaviour, but vibrates heavily. The tiebreak condition configuration initially behaves as the analytical solution. However, after this initial behaviour, the failure criteria of the contact is reached earlier than expected (at a displacement of approximately 3 mm), and a response dissimilar to the analytical solution arises. Neither of the two simulations gives an acceptable result.

The simulation times are listed in Table 4.15. It may be seen that the cohesive zone has a higher computational cost than the tiebreak condition. Due to the undesired response, none of the thin-shell configurations in the DCB test are recommended.

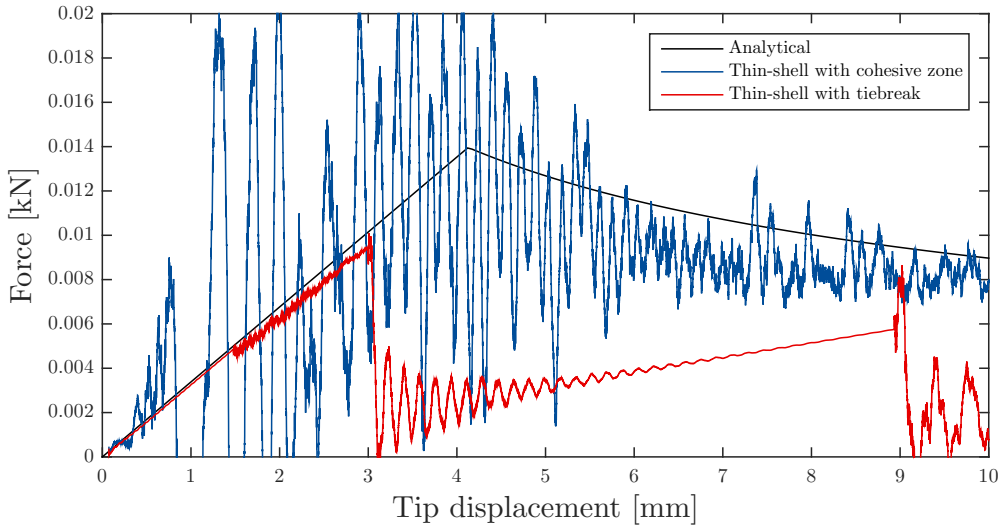

Figure 4.16: *Comparison of the force-displacement relation for the DCB/Mode I simulations with cohesive elements and tiebreak condition as adhesive model for the thin-shell element formulation.*

Table 4.15: Simulation times for the DCB test when modelling using thin-shell elements.

Adhesive model	**Time [s]**
Cohesive zone	3240
Tiebreak condition	2551

4.3.3.3 Thick-shell elements

In Section 4.1, it was recommended to use element formulation ELFORM 5 when modelling thick-shell elements. However, some unstable behaviour was detected in the testing of this section. The thick-shell elements are therefore henceforth modelled using element formulation ELFORM 1, with hourglass control activated. The difference is illustrated in Figure 4.17 where the results for both ELFORM 1 and ELFORM 5 are presented. It can be seen that while the ELFORM 1 configuration behaves as intended, the ELFORM 5 response is vibrating heavily.

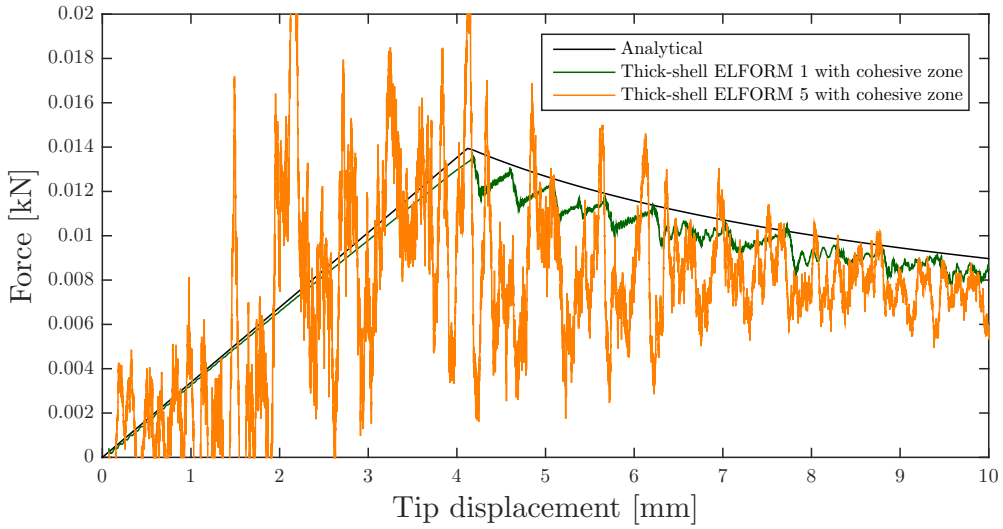

Figure 4.17: *Comparison of the force-displacement relation for cohesive zone using ELFORM 1 (green) and ELFORM 5 (orange).*

For the thick-shell element, the force-displacement relations obtained in the DCB test are presented and compared to the analytical result in Figure 4.18. It can be seen that both adhesive models exhibit the desired behaviour, but the force-displacement curve obtained when modelling using tiebreak condition is not as smooth as the one obtained using a cohesive zone or the analytical results. This indicates that large areas are released from contact at the same displacement. Additionally, the tiebreak condition does not sustain enough loading until the crack propagation is initiated. This is something that could be solved by tuning the parameters in the contact card, but since a parameter that requires tuning is undesirable this is considered as a drawback of the thick-shell element - tiebreak contact condition combination.

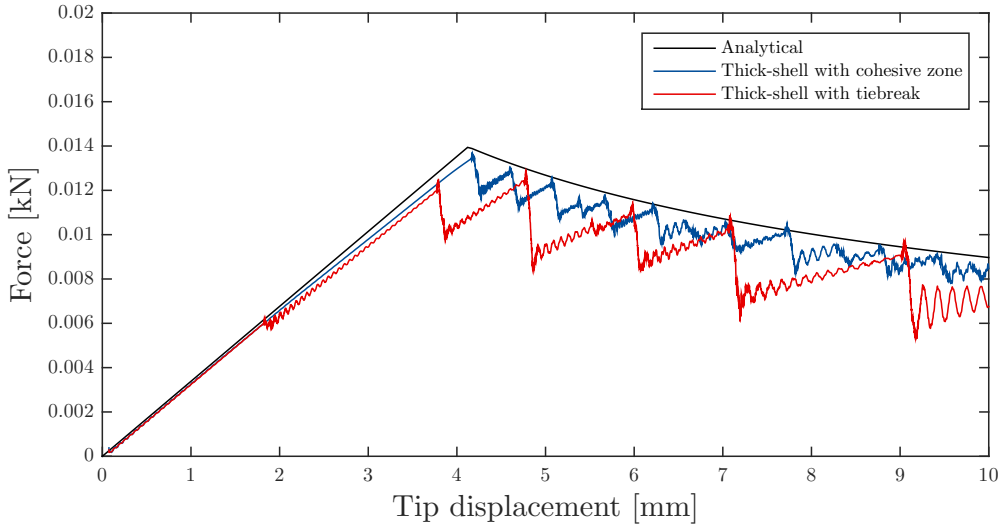

Figure 4.18: *Comparison of the force-displacement relation for the DCB/Mode I simulations with cohesive elements and tiebreak condition as adhesive model for the thick-shell element formulation.*

Table 4.16: Simulation times for the DCB test when modelling using thick-shell elements.

Adhesive model	**Time** [s]
Cohesive zone	3768
Tiebreak condition	1988

4.3.4 ENF test

In order to study the response when a crack propagates along the ply interface according to mode II, an end notched flexure (ENF) test is performed. A schematic figure of the ENF test is presented in Figure 4.20. The test consists of a specimen with an initial crack of length a_0. The specimen is placed on two supports, both modelled using the boundary condition BOUNDARY_SPC(SET), with a velocity of 0.05 m/s. For the pinned support (left) all translational degrees of freedom are fixed, while for the roller support (right) all translational degrees of freedom are fixed except for the movement along the length of the beam. For the solid and thick-shell elements the boundary condition is applied on the bottom nodes in the thickness direction. A force (F) is applied at the midpoint of the beam. The force is added using an applied displacement in the middle nodes of the top ply modelled with BOUNDARY_PRESCRIBED_MOTION. For the solid and thick-shell elements the upper nodes in the thickness direction are used for the applied displacement. The parameters for the simulations are presented in Table 4.17. An elastic material (MAT1) is used for modelling the plies. The same mesh as for the DCB tests is used in the ENF simulations, which means that each layer is modelled with one ply through thickness and the element size is 1×1 mm. This gives a total of 20×150 elements in each ply.

In the analysis the fracture zone is modelled using either a tiebreak contact condition (using S_{12} as failure condition) or a cohesive zone (using both G_{IIC} and S_{12} as failure condition).

Table 4.17: Material properties and measurements for the ENF simulations.

Property	Value	
E	132	GPa
ν	0.3	
ρ	1.5	g/cm^3
G_{IIC}	690	J/m^2
S_{12}	77.8	MPa
L	150	mm
a_0	58	mm
t	1	mm
w	20	mm

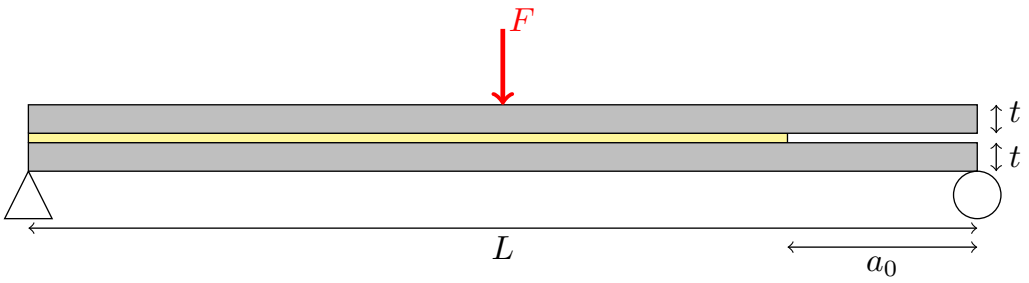

Figure 4.19: *Schematic figure of Mode II/ENF test. The two plies (gray) with length L, thickness t and width w with an applied force F (red) in the middle of the beam. Between the plies are an adhesive (yellow) and an initial opening of length* a_0.

To predict the behaviour of the crack growth along the ply interface, an analytical solution is calculated. The analytical solution of the ENF test is divided into four parts; (i) before the crack grows, (ii) the crack growth until the crack spans to the midpoint of the beam, (iii) the crack growth from the midpoint until the crack spans over the entire length and (iv) after the crack spans over the entire length of the beam. The force-displacement relation for each part can be seen in Equations (4.8)-(4.11). The fourth part of the calculations is after the crack spans over the entire length, meaning bending of two beams that slide on top of each other [25]. This part is not included in the solution, due to only the crack propagation being of interest. The behaviour according to the hand calculations, with the properties for the ENF simulations described above is presented in Figure 4.20. The force at initial crack propagation is approximated to 135N at a displacement of 9 mm.

$$\delta_i = \frac{2L^3 + 3a_0^3}{96EI}F \tag{4.8}$$

$$\delta_{ii} = \frac{F}{96EI}\left(2L^3 + \frac{(64G_{IIC}wEI)^{3/2}}{\sqrt{3}F^3}\right) \tag{4.9}$$

$$\delta_{iii} = \frac{F}{24EI}\left(2L^3 - \frac{(64G_{IIC}wEI)^{3/2}}{4\sqrt{3}F^3}\right) \tag{4.10}$$

$$\delta_{iv} = \frac{L^3}{12EI}F \tag{4.11}$$

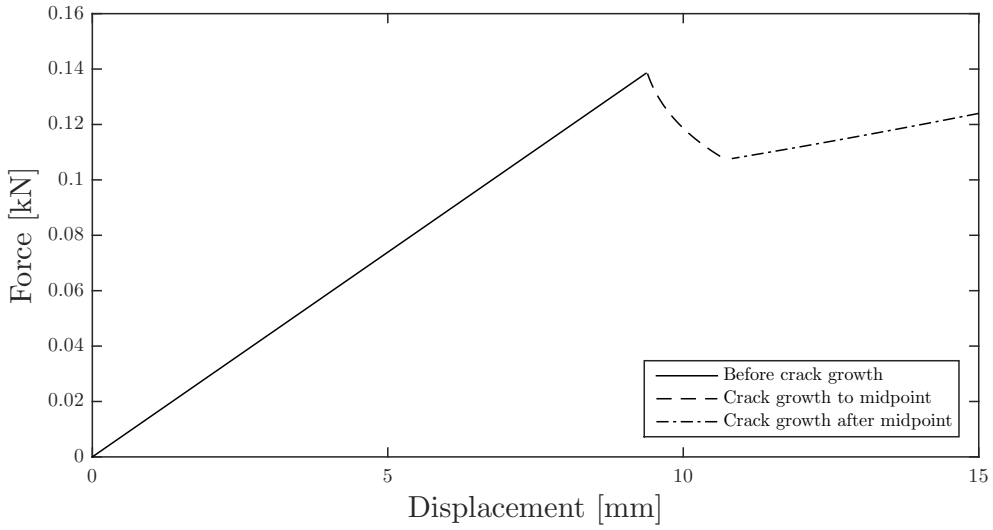

Figure 4.20: *The force-displacement relation for the analytic ENF/Mode II calculations.*

4.3.4.1 Solid elements

In Figure 4.21, a comparison of the force-displacement response obtained for the solid elements in the ENF test is presented for both adhesive modelling methods. The response of the cohesive zone, the tiebreak condition, and the analytical solution is included. It can be seen that the tiebreak condition does not correlate with the analytical force-displacement relation. The behaviour of the tiebreak simulation indicates that the criteria for failure is met immediately, and therefore it behaves as if the two plies are not tied together in any way. This is not a reasonable response. It can also be seen that the behaviour of the cohesive element configuration is similar to the analytical predicted response.

The simulation times are listed in Table 4.18. The tiebreak condition is more time efficient than the cohesive zone, but as stated earlier an unreasonable force-displacement response is obtained for the combination of solid elements and the tiebreak contact condition.

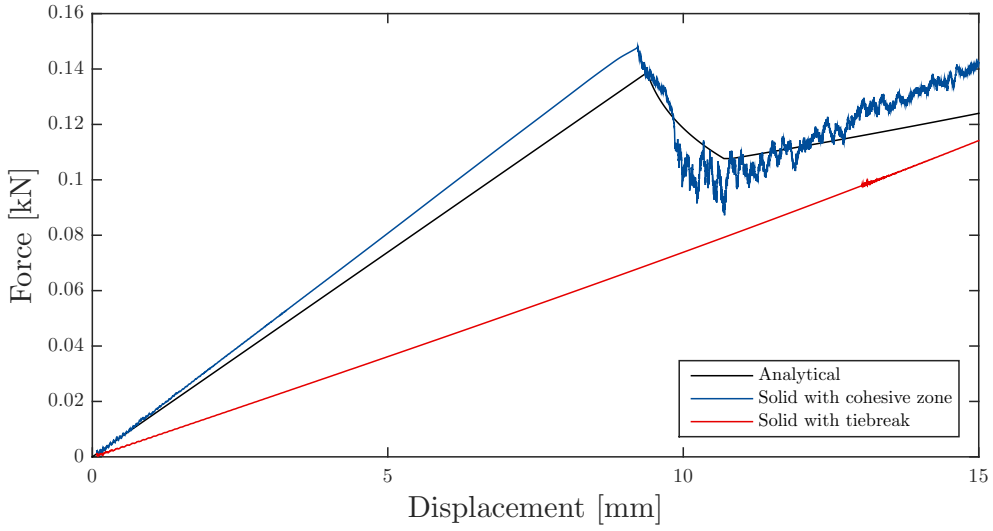

Figure 4.21: *The force-displacement relation obtained from the ENF simulations when modelling the plies using solid elements. Both a cohesive zone (blue) and a tiebreak condition (red), was used to model the adhesive. The analytical solution (black) is included for a comparison.*

Table 4.18: The simulation time for the ENF test when modelling using solid elements.

Adhesive model	**Time [s]**
Cohesive zone	13984
Tiebreak	11893

4.3.4.2 Thin-shell elements

A comparison of the force-displacement responses obtained for the two different adhesive modelling methods in the ENF test are presented in Figure 4.22. Thin-shell elements were used for modelling the plies. Both configurations behave unreasonable compared to the analytical solution. The configuration with cohesive elements does not sustain enough displacement until failure and is vibrating heavily. The vibrations may introduce local stress concentrations and this could be the reason for the early failure. Even though the cohesive elements are eroded too quickly, the behaviour has the same pattern as the analytical result, and with some modifications this model may be improved to resemble the desired curve. The tiebreak condition fails immediately and give an unphysical response. This adhesive modelling gave an error and the simulation was terminated.

The simulation times are listed in Table 4.19. Note that due to the termination of the tiebreak condition simulation, no simulation time may be listed for this configuration.

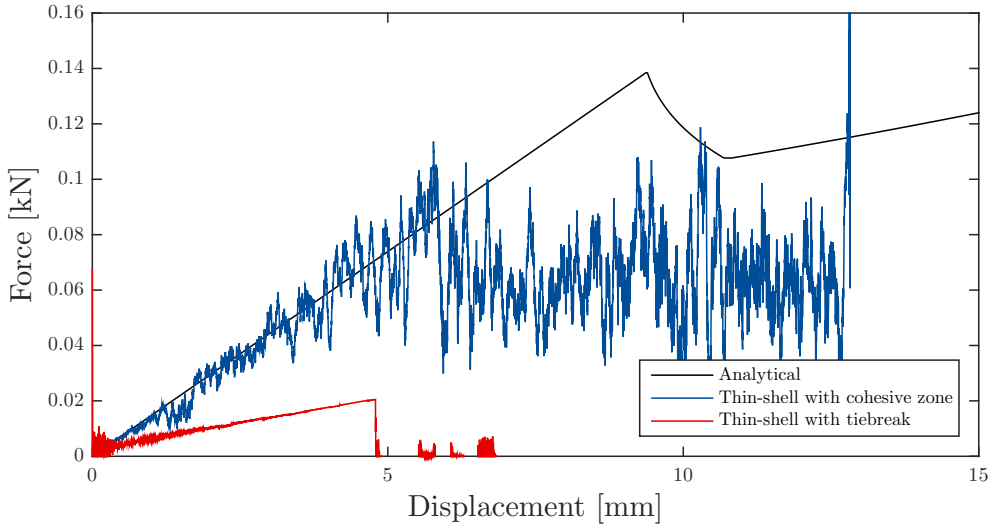

Figure 4.22: *The force-displacement relation obtained from the ENF simulations when modelling the plies using thin-shell elements. Both a cohesive zone (blue) and a tiebreak condition (red), were used to model the adhesive. The analytical solution (black) is included for a comparison.*

Table 4.19: The simulation time for the ENF test when modelling using thin-shell elements.

Adhesive model	**Time [s]**
Cohesive zone	N/A
Tiebreak	3909

4.3.4.3 Thick-shell elements

A comparison of the response of the adhesive modelling methods (cohesive zone and tiebreak contact condition) in the ENF is presented in Figure 4.23. It can be seen that the configuration using tiebreak condition behaves unreasonable and very stiffly compared to the analytical solution. The behaviour of the thick-shell elements combined with cohesive elements is very similar to the analytical behaviour.

The simulation time for both the cohesive zone and the tiebreak contact condition are listed in Table 4.20.

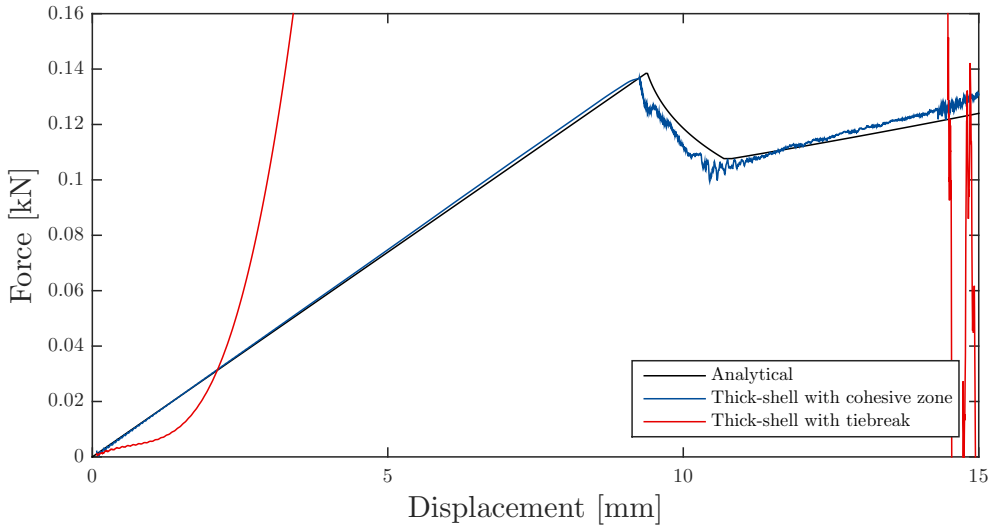

Figure 4.23: *Comparison of the force-displacement relation for the ENF/Mode II simulations with cohesive elements and tiebreak condition as adhesive model for the thick-shell element formulation.*

Table 4.20: The simulation time for the ENF test when modelling using thick-shell elements.

Adhesive model	**Time [s]**
Cohesive zone	5483
Tiebreak	3160

4.3.5 Brief conclusion

The crack propagation along the interface of two plies, i.e. the delamination behaviour, was investigated using two different tests; DCB and ENF. Based on this, the behaviour of the adhesive modelling methods, tiebreak condition and cohesive zone, in combination with both solid, thin-shell, and thick-shell elements was investigated.

For solid elements, the cohesive zone gave a good response for both mode I and mode II. For mode I, the curve at crack growth is not as smooth as the analytical solution, but clearly the wanted behaviour is reached. The tiebreak condition gave a reasonable response for mode I, but with a too early initiated crack growth and an unstable force-displacement relation. For mode II, an unrealistic result was obtained.

In both tests, the thin-shell elements exhibited large vibrations and none of the adhesive modelling methods gave results that corresponded to the analytical results. The thin-shell are therefore excluded from all further analysis.

For thick-shell elements, the cohesive zone gave good results close to the analytical solution, especially for mode II. As for solid elements, the curve is not as smooth as the analytical solution for mode I, but the desired behaviour is clearly implied. The tiebreak condition gave a reasonable result for mode I crack propagation. However, as for the solid elements the crack growth was initiated at a displacement lower than indicated in the analytical calculations. Compared to the cohesive response, the tiebreak condition provides an unstable curve. For mode II, the tiebreak condition gave unreasonable results.

It is concluded that adhesive modelling using a tiebreak condition does not perform as well as using a cohesive zone. Note that the tiebreak condition most likely can be calibrated to work as intended for both modes. For the cohesive zone on the other hand, no calibration was needed, and the initial configuration gave reasonable results for both thick-shell and solid elements. Therefore, this adhesive modelling method is to be preferred. Additionally, the cohesive zone may result in a smoother curve if a mesh refinement is performed. However, this is not of interest in this case due to the higher computational cost the increase in number elements would induce.

Based on that the combination of thick-shell elements ELFORM 1 and a cohesive zone results in a simulation time that is less than half of the one using solid elements, this combination is chosen to be further analysed.

4.4 Combining composite material model and adhesive model

The purpose of this section, is to determine which combinations of the different composite material models and the adhesive modelling that are compatible. The same tests as used to analyse the adhesive modelling behaviour are repeated in this section; DCB and ENF tests.

In Section 4.3, it was determined that the adhesive was best modelled using a cohesive zone. This, together with thick-shell elements (ELFORM 1) gave the most efficient way of modelling the delamination of mode I and mode II. Therefore, this configuration is used in the simulations.

In Section 4.2, it can be seen that all listed composite materials are compatible with the thick-shell elements except for MAT55 that does not exhibit a proper failure behaviour.

The force-displacement relation is illustrated in Figure 4.24 for the elastic case as well as with the different material models. It can be seen that for the DCB test, three material models gives a reasonable response similar to the analytical one; MAT22, MAT58 and MAT262. For the ENF test, only two material models give a reasonable response; MAT261 and MAT262. Note that MAT22 follow the same curve, but exhibit failure. This material model has earlier been documented to reach the failure criteria in an early stage.

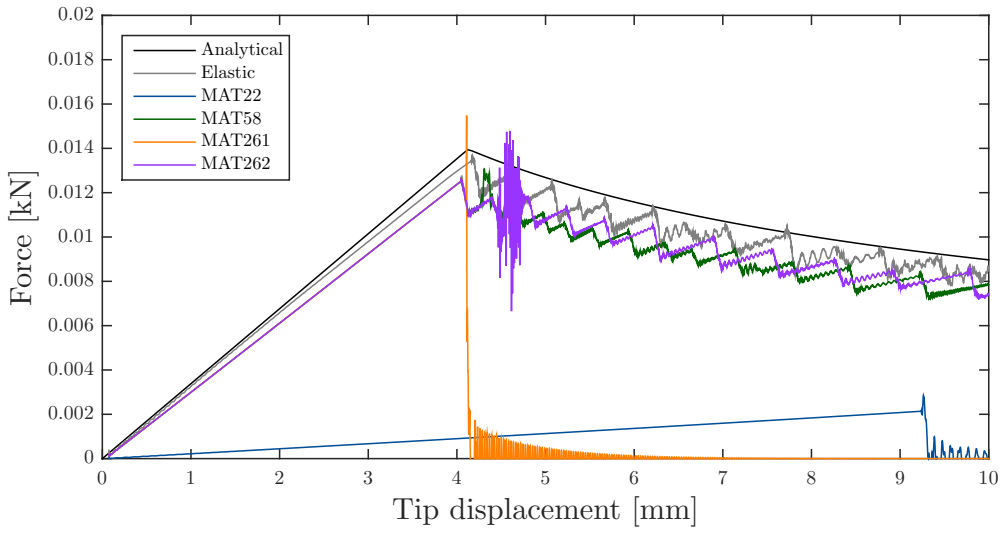

(a)

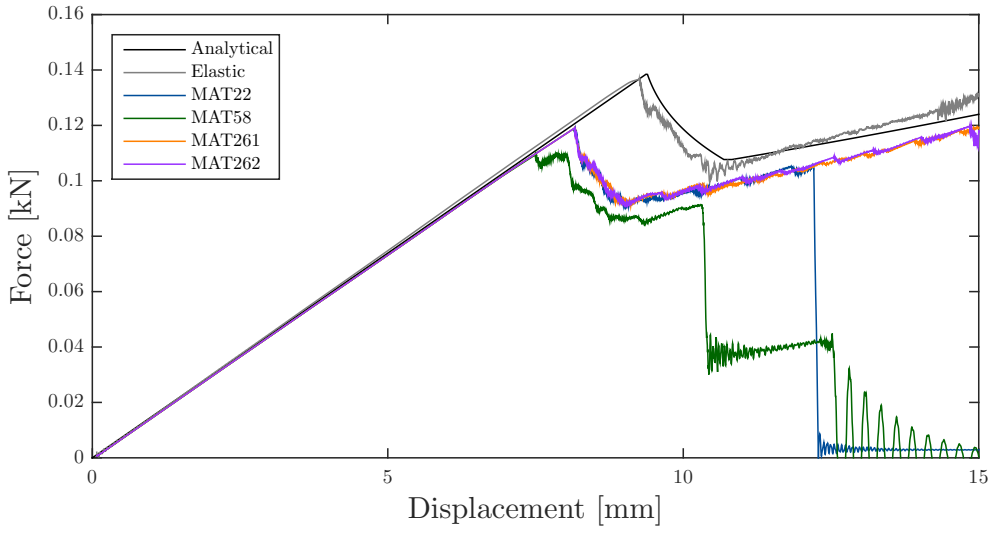

(b)

Figure 4.24: *The force displacement relation for (a) the DCB simulations and (b) the ENF simulations using different composite material models combined with thick-shell elements (ELFORM 1).*

4.4.1 Brief conclusion

The only material model that exhibit a good response in both the DCB and the ENF test is MAT262. This strengthens the conclusion of using this material model for modelling the composite laminate.

4.5 Version study in LS-DYNA

During the project, it was concluded that different versions of LS-DYNA gave unexpected differing results. The presented results are not an accurate comparison between the versions, but a way of alerting users of the varying results that different versions of LS-DYNA provide. Note that it is unclear if the results differ due to the versions or the solver types; SMP (symmetric multiprocessing, for running on few CPUs, e.g. desktop computer) or MPP (massively parallel processing, for running on many CPUs, e.g. a computer cluster).

A comparison of version R7.1.2 SMP and version R8.0.0 MPP has been performed, and a difference of the simulation results has been discovered. A comparison of the force-displacement relation for a cantilever beam test with shell elements (ELFORM 16) and MAT261 is presented in Figure 4.25. It can be seen that the results differ between the versions. It is worth noting that for version R7.1.2 SMP, the vibrating increases without any extra loading introduced, which is not considered as reasonable.

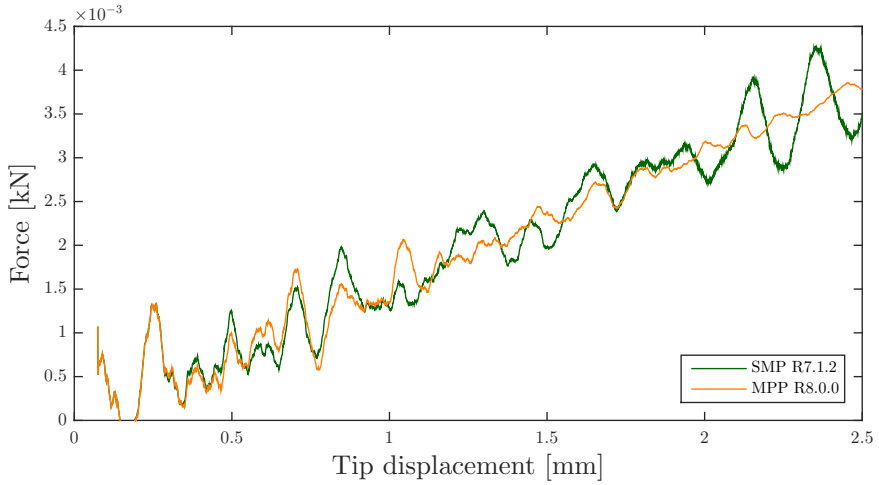

Figure 4.25: *A comparison of the force-displacement curve from the cantilever beam test with MAT261 and Shell ELFORM 16 when using version R7.1.2 SMP (green) and version R8.0.0 MPP (orange).*

To compare the effect of different versions for the cohesive elements, the ENF test described in Section 4.3.4 is run using the two different versions in LS-DYNA. The force-displacement results are presented in Figure 4.26 and here the difference is visible as well. The simulations are run using solid elements (ELFORM 3) and an elastic material model (MAT1).

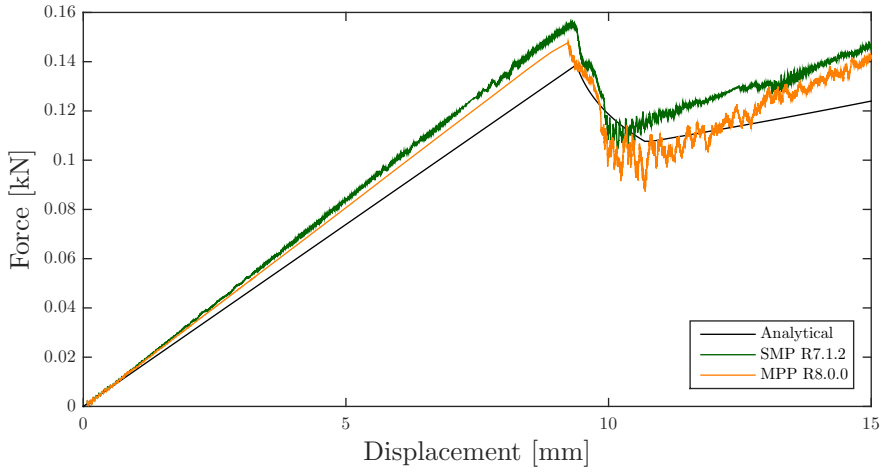

Figure 4.26: *A comparison of the force-displacement curve from the ENF test when using version R7.1.2 SMP (green) and version R8.0.0 MPP (orange).*

4.5.1 Brief conclusion

From Figure 4.25 and Figure 4.26 it can be seen that for MAT261 in version R8.0.0. MPP seems to behave more stable with regards to vibration, and for the ENF simulations the behaviour of the R8.0.0 MPP simulation is closer to the analytical, desired behaviour. Therefore version R8.0.0 MPP is preferred over R7.1.2 SMP.

4.6 Hat profile model testing procedure

In this chapter, the process of implementing the obtained results into the model matching the experimental setup described in Section 3 is presented. The model is built on a simulation model provided by Gestamp HardTech.

4.6.1 Modelling the steel beam

In the original geometry, the steel hat profile beam was modelled with thin-shell elements. To be able to simulate the delamination behaviour between the steel and the composite using a cohesive zone, the steel beam is modelled with thick-shell elements. None of the cohesive elements in LS-DYNA can be used to connect thin-shell with thick-shell or solid elements. A comparison between the original element formulation (thin-shell ELFORM 2) and two different types of thick-shell elements, (ELFORM 1 and 5) was done. The setup of the simulation was the same for all cases, with a difference in element type and the corresponding hourglass control. A loading based on the one in the experiment was used, i.e. a constant velocity of the impactor.

The result is presented in Figure 4.27. It can be seen that thick-shell ELFORM 1 has the same buckling behaviour as thin-shell ELFORM 16 while thick-shell ELFORM 5 does not buckle properly. The buckling starts (or should start) at the displacement $\delta = 23$mm for the pure steel beam, based on the results from the thin-shell element simulations. The subsequent decrease of bending stiffness may be seen as a drop in the force needed to impose the displacement at approximately 23 mm.

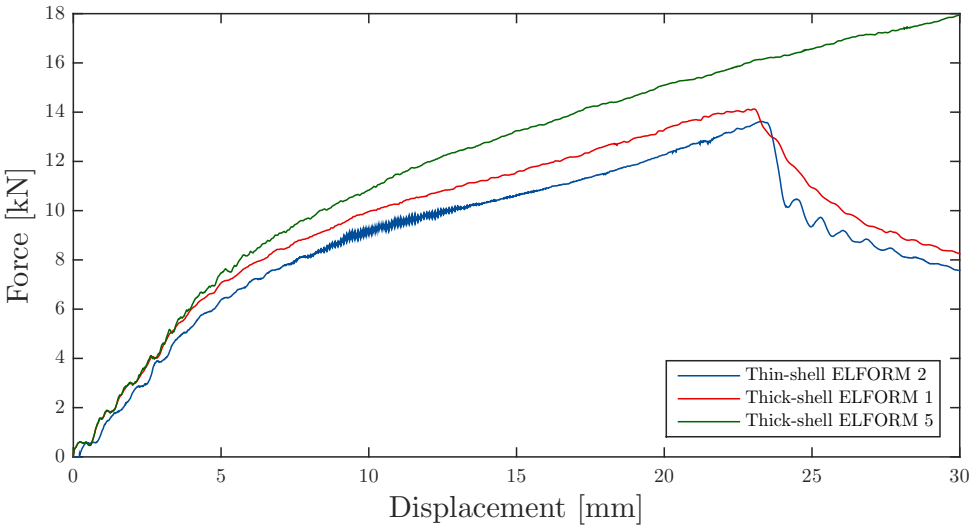

Figure 4.27: *The force-displacement relation of the steel beam for (blue) thin-shell ELFORM 2, (red) thick-shell ELFORM 1, and (green) thick-shell ELFORM 5.*

The buckling at a displacement of 30 mm, i.e when the buckling is fully developed, is presented in Figure 4.28. It can be seen that the geometry modelled with thick-shells ELFORM 1 gives a similar buckling response as the original modelling method using thin-shell ELFORM 2. The thick-shells ELFORM 5 on the other hand exhibit a different behaviour. The buckling behaviour of the thin-shell and thick-shell ELFORM 1 approaches are considered physically plausible, while the behaviour of the thick-shell ELFORM 5 simulation is not. Therefore the steel beam in the full model is modelled using thick-shell elements ELFORM 1.

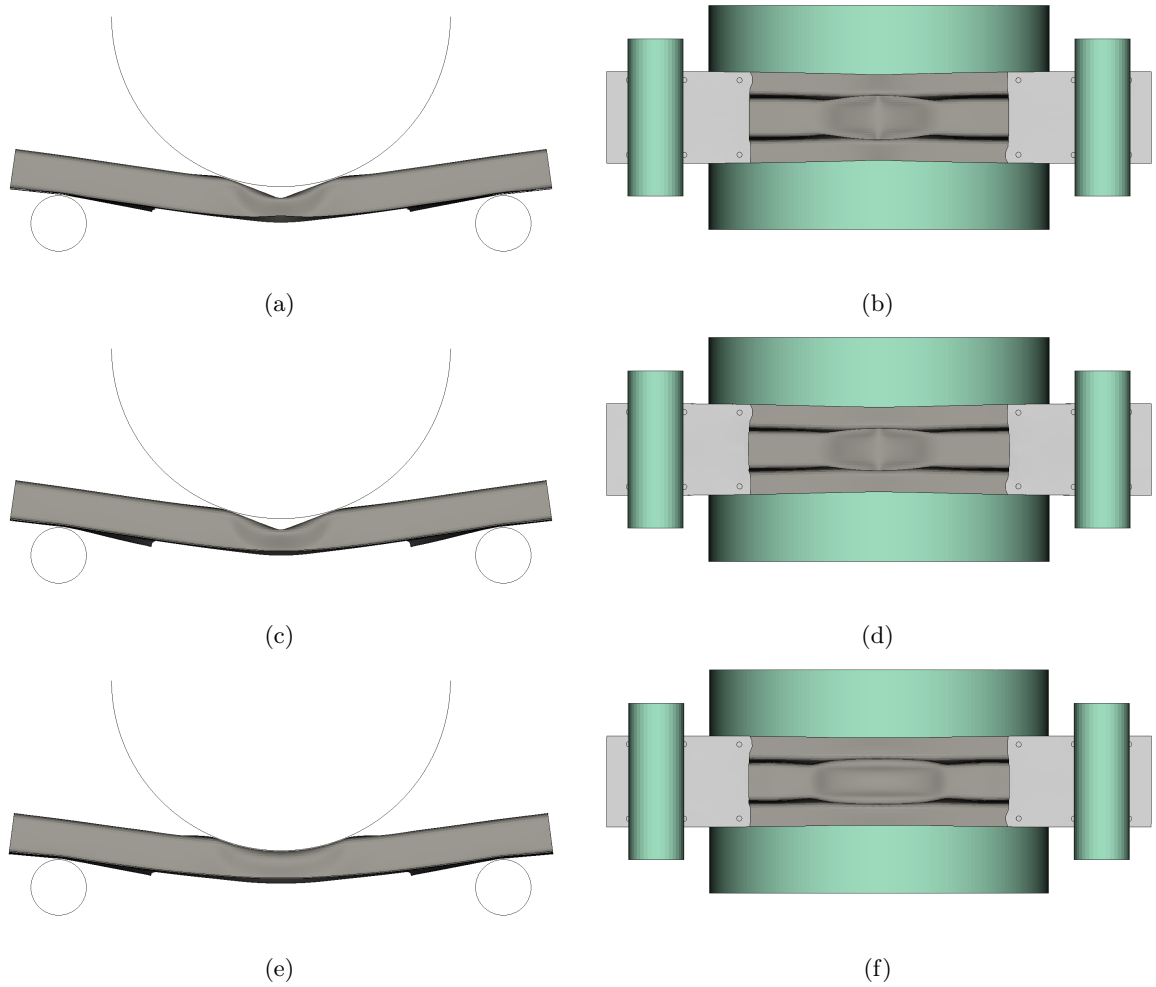

Figure 4.28: *The buckling behaviour using (a)-(b) the original modelling method (thin-shell elements ELFORM 2), (c)-(d) thick-shell elements ELFORM 1 and (e)-(f) thick-shell elements ELFORM 5. The behaviour is captured at a applied displacement of 30 mm.*

4.6.2 Modelling the composite laminate

In the middle of the composite plate there are four adjacent plies with the same fibre orientation. Since delamination does not occur often in the interface between same angled layers [2], and since the computational cost is important, these four plies are modelled together using one thick ply. By doing this 6 element layers are removed, 3 composite plies and 3 cohesive plies, which saves computational effort since both composite and cohesive material models are computationally costly, as has been presented with previous testing.

4.6.3 Benchmarking the simulation model

From the small scale tests it is suggested that the steel should be modelled using thick-shell ELFORM 1, the composite material using thick-shell ELFORM 1 combined with MAT262, for material card see Appendix A. The interface between steel and composite and lamina interface should be modelled using cohesive elements with a size of 1×1mm. It was also discovered that for LS-DYNA version R8.0.0. cohesive elements are not eroded automatically when its neighbouring composite elements are removed. This leads to a heavily distorted cohesive element, and is not considered as a physical behaviour. This problem is fixed in LS-DYNA version R9.0.0. Cohesive elements are eroded automatically if the ICOHED flag in the CONTROL_SOLID card is used. Therefore the hat profile simulations use R9.0.0 MPP with the ICOHED flag instead of R8.0.0 MPP. It was also discovered that the ADD_EROSION card gave out-of-bound forces, and therefore the erosion card is left out of the simulations. During the search for errors regarding the cohesive zone, the material model of the cohesive elements was changed into the more simple material model MAT138.

The resulting force-displacement for the initial settings with the modifications described above (i.e. no ADD_EROSION, a mesh size of 1 × 1mm in the composite and cohesive elements, and LS-DYNA version R9.0.0 MPP) is presented in Figure 4.29 together with the experimental results. In Figure 4.30 the deformation of beam A from three views is shown. It can be seen that the composite exhibits delamination throughout the entire composite plate, resulting in the bottom part of the plate falling off. The same views for beam E is shown in Figure 4.31. For beam E, the composite has not delaminated throughout the entire plate, and therefore the composite is still attached at the edges but has detached at the buckled part of the steel. Note that for both beams there is still one ply attached to the steel. For beam A the ply has a fibre angle of 0° and for beam E the fibre angle of the ply is 90°.

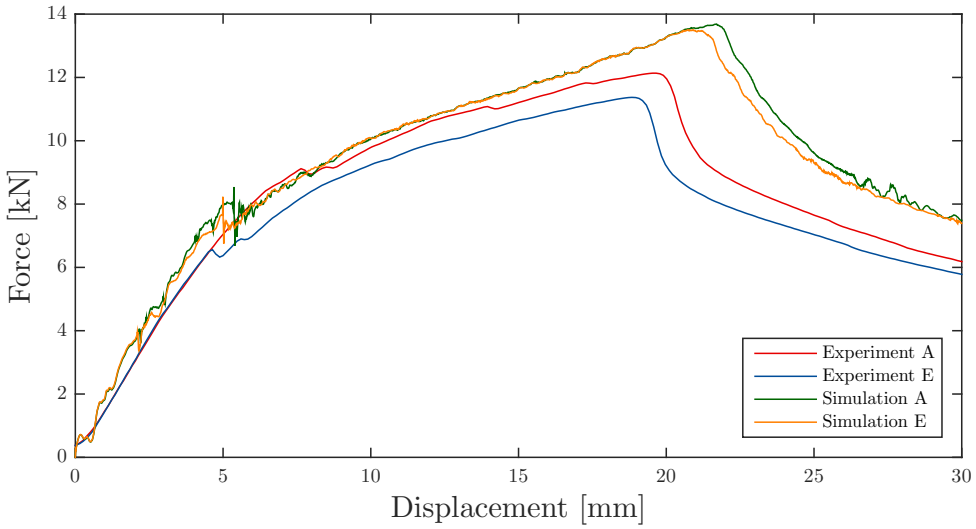

Figure 4.29: *The force displacement relations for (red) test beam A, (blue) test beam E, (green) simulation beam A, and (orange) simulation beam E.*

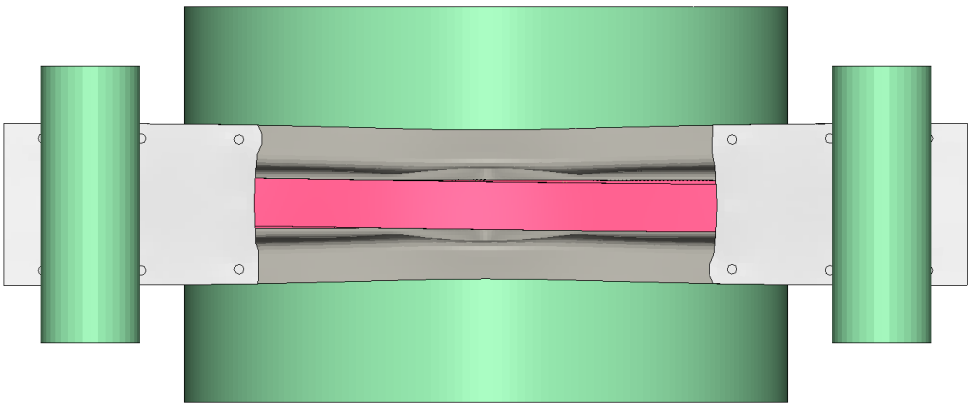

(a)

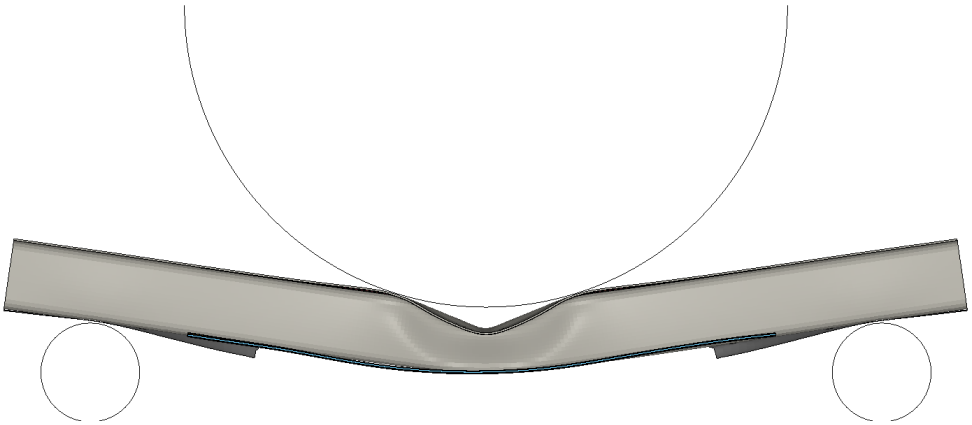

(b)

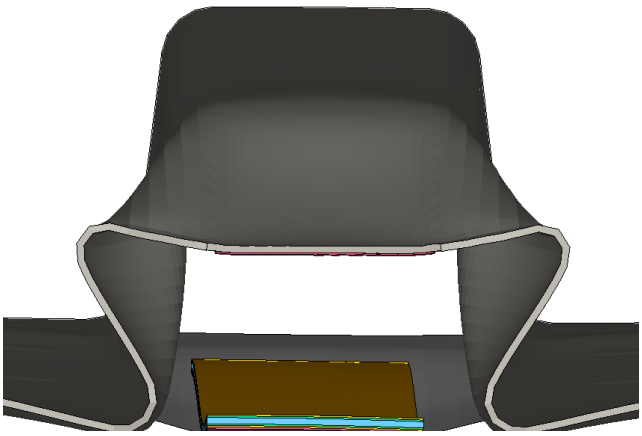

(c)

Figure 4.30: *Test beam A simulation results from (a) the bottom, (b) from the side with the beam cut through the middle of the width in order to see the delamination of the beam, and (c) the cross section at the final time step of the simulation. The plies are colour coordinated according to;* 0° *- pink,* 45° *- orange,* −45° *- green,* 90° *- blue, and cohesive elements are yellow.*

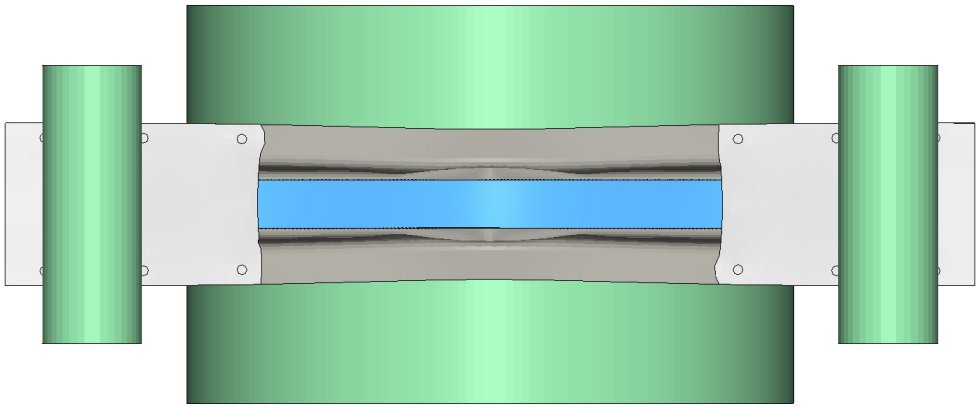

(a)

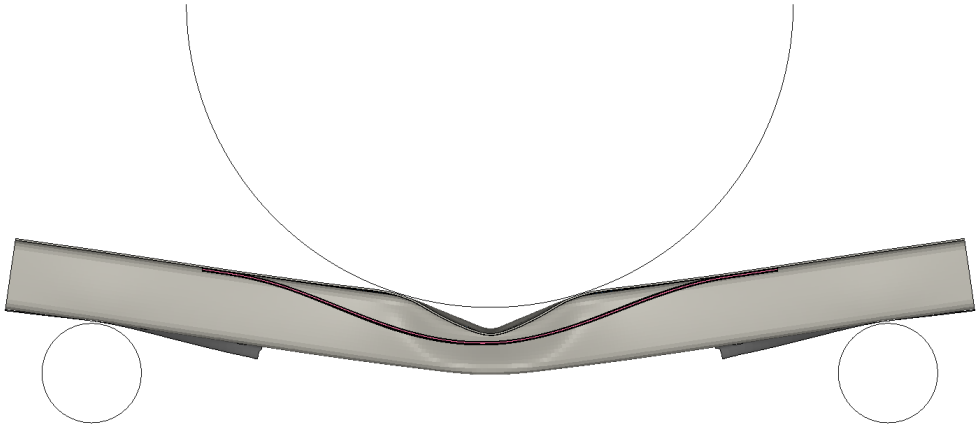

(b)

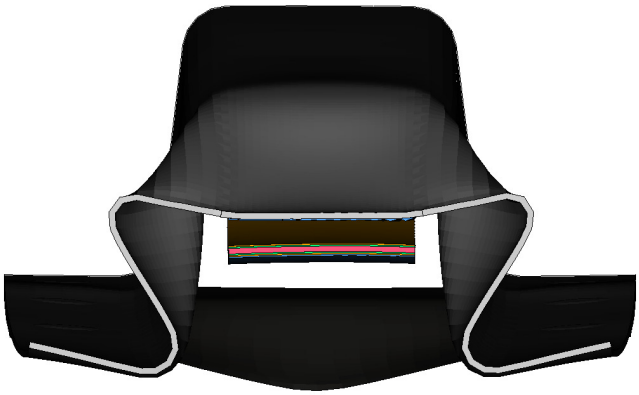

(c)

Figure 4.31: *Test beam E simulation results from (a) the bottom, (b) from the side with the beam cut through the middle of the width in order to see the delamination of the beam, and (c) the cross section at the final time step of the simulation. The plies are colour coordinated according to;* $0°$ *- pink,* $45°$ *- orange,* $-45°$ *- green,* $90°$ *- blue, and cohesive elements are yellow.*

In Figure 4.29 it can be seen that the simulations give stiffer results than both experimental results. This indicates that either some material in the simulation is stiffer than the actual case, or that some dimension is larger in the model than in reality. In the gluing process the composite together with the steel was heated to 175°C and this could have had an effect on the properties of steel, which could be the reason for the softer experimental results. When comparing the delamination behaviour for the simulations and experiments, which can be seen in the graph as a sudden drop in the force, it can be seen that beam A delaminates at an earlier stage in the simulations compared to the experiment. For beam E, the simulation and the experiment delaminates at the same displacement, but not the same force. This however could be described by the overly stiff response of the steel in the simulation.

In order to see this effect, the simulation results are compared to the response of a pure steel beam in Figure 4.32. In the figure it can be seen that initially both beams with composite behave stiffer, but after delamination all three beams exhibit the same stiffness until buckling. The point of buckling is different for all three beams.

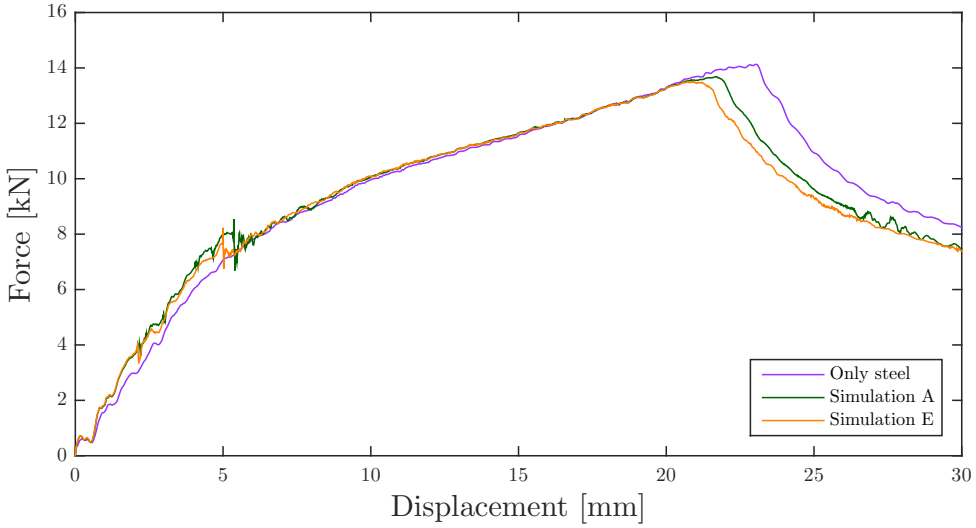

Figure 4.32: *The force displacement relations for (purple) the pure steel beam, (green) simulation of beam A, and (orange) simulation of beam E.*

4.6.3.1 Yield property study

Since the steel behaves too stiff, the simulations are performed again with lowered yield properties of the steel. The values in the yield curve presented in Section 3 are lowered by 20% in order to compensate for the overly stiff steel. The result is presented in Figure 4.33.

In Figure 4.33 it can be seen that lowering the steel properties alters the buckling behaviour, but does not move the point of delamination much with respect to the displacement. This indicates that the stiffness of the steel caused the difference in point of buckling for the original setup, and with some tuning of the yield parameters the correct point of buckling could be obtained. This also indicates that the original assumption of the overly stiff steel in simulations was correct.

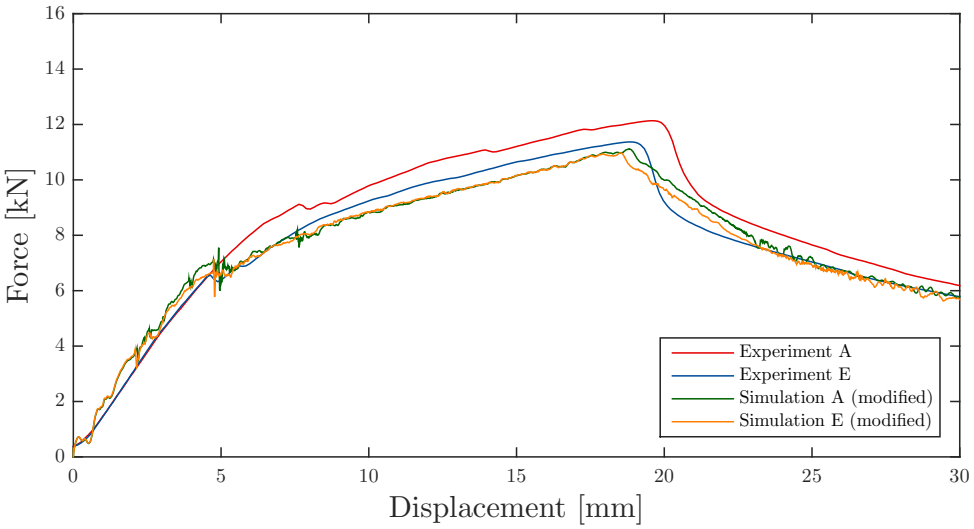

Figure 4.33: *The force displacement relations for (red) test beam A, (blue) test beam E, (green) simulation beam A with lowered yield parameters, and (orange) simulation beam E with lowered yield parameters.*

5 Recommended model configuration

The current section describes the modelling procedure in LS-DYNA that is found best to predict the behaviour of a steel-composite structure in a crash scenario. The described modelling method is formulated with focus on capturing the delamination between the steel and the composite laminate as well as between the plies in the composite laminate. When deciding on for example element type, material model and adhesive modelling method, both the behaviour of the model and the computational cost were taken into account.

In order to capture the delamination behaviour within the composite laminate, each ply of the laminate requires to be modelled separately. The plies are then connected by an adhesive model.

5.1 Element type

Both the composite plies and the steel should be modelled using thick-shell elements. The recommended element formulation is ELFORM 1, supplemented with hourglass control. For the simulations in this project, hourglass control 1 with the default coefficient (0.1) is used. Since no investigation of the different hourglass control methods has been performed, no specific recommendation can be provided.

If there are two or more adjacent plies with the same fibre angle, these can be modelled as one thick ply. This in order to reduce the computational cost. If this is done, it is important to keep the aspect ratio of the elements in mind. If the aspect ratio gets poor when combining many plies into one element, it is possible to use more layers of elements and merge the nodes instead of using a cohesive element between. This will also reduce the computational cost. Note that this is not applicable for composites where there are very many plies with the same orientation stacked together. Since this not has been studied specifically, no exact recommendation as to how many plies can be joined together without losing delamination information can be given.

5.2 Adhesive model

In Section 4.3, a comparison between different adhesive modelling methods is presented. Based on this comparison, the cohesive zone is recommended for capturing delamination of both mode I and mode II.

By using a cohesive zone, cohesive elements are implemented between the layers with the nodes merged to the adjacent plies. A zero thickness is allowed and used in the tested model. No study of the thickness of the cohesive zone is performed. Since the adhesive is implemented between plies modelled using thick-shells, element formulation 19 is to be used for the cohesive zone.

The cohesive elements are mesh dependent and the recommendations of the discretisation are described in Section 5.4.

5.3 Material models

Based on the tests described in Section 4, it can be seen that material model MAT262 has a good behaviour and comes at a computational cost that, compared to the other composite material models, is reasonable. Therefore, if there is enough material data provided, this material model is recommended. Note that no calibration of the unphysical parameters included in the more simple material models was performed. If not enough material data is provided to implement MAT262, an additional study may be needed. In order to capture the maximum and minimum strains in the ADD_EROSION card should be added if it can be implemented without causing errors.

For the cohesive zone, the material model MAT186 was used in the pre-study. This material card requires the critical energy release rates (G_{IC} and G_{IIC}), the ultimate strengths (mode I and mode II) and a traction-separation curve. Due to a search of an error, the material model was replaced by MAT138 when benchmarking the full hat profile beam model. When implementing MAT138, the Young's moduli (E_t and E_n), energy release rates (G_{IC} and G_{IIC}), the ultimate strengths (mode I and mode II), and the ultimate displacements are possible inputs. Peak traction is not necessary to define and can be calculated using the other inputs, since the traction-separation relation is bilinear for this material model. However, the error was not due to the cohesive material model. Nevertheless, due to the fine response of the full model, MAT138 was kept. Both cohesive material models MAT138 and MAT186 are therefore considered usable.

5.4 Mesh discretisation

The recommended adhesive modelling method, the cohesive zone, is mesh dependent. The cohesive elements require a relatively fine mesh to provide the wanted behaviour. For the simulations in Section 4.3 an element size of approximately 1×1 mm is used. If the mesh is too coarse the delamination behaviour will not be captured as intended.

5.5 Contact conditions

A general single surface contact is included to handle the contact between the beam and supports, as well as the contact between the composite plies after delamination. In order to capture the contact force between the rigid impactor and the steel beam, FORCE_TRANSDUCER_PENALTY is implemented between the two parts. For the contacts, BSORT is set to 10, so that the contact is checked every tenth time step. This in order to not let the contact pass through one of the thin composite elements unnoticed.

5.6 Important settings

It is important to use version R9.0.0 of LS-DYNA, otherwise the cohesive elements can cause problems if its neighbouring elements are eroded. This problem is solved by setting the parameter ICOHED to 1 in the CONTROL_SOLID card.

In order to allow for initial penetration, the IGNORE parameter in CONTROL_CONTACT need to be set to 1 or 2. If this is not done, an initial penetration can lead to an inaccurate behaviour in the beginning of the simulation.

If a contact condition is used to model the interface, it is important to use OPTION 4 in the contact card.

6 Concluding remarks

The obtained results suggests that the delamination may be captured in a steel-composite structure. The computational cost is high due to many factors. The composite material models are generally computational expensive. This is combined with the large amount of elements, both due to modelling each ply with an element through thickness and due the mesh refinements needed for the cohesive zone to behave as intended. The recommended model configuration is formulated to keep the computational cost low while still getting the wanted behaviour.

From the procedure it can be concluded that it is of importance to be observant of what material models are compatible with what element types. It is also concluded that for modelling delamination where the composite is at risk of failing prior to the cohesive elements, the LS-DYNA version R9.0.0 should be used. This with the ICOHED flag activated.

Additional studies are needed in order to possess a simulation model that is reliable enough to be used in the product development process at Gestamp HardTech. However, this study is a great initial step towards a simulation model that may predict the failure behaviour of steel-composite components.

7 Future work

In order to ensure the level of prediction in the model, more types of experiments are needed. This is to be carried out at Gestamp HardTech. The maximum and minimum strains need to be included in order to give a better correlation with the experiments with respect to the failure. A more thorough investigation of which adjacent fibre angles are possible to model together, either using merged nodes or one thicker ply, and still maintain a satisfactory level of prediction in the analysis is required. This is needed if laminates with more plies are to be modelled at a reasonable computational cost.

References

[1] *LS-DYNA Keyword User's Manual, Volume I*. 971st ed. California: Livermore Software Technology Corporation, 2007. ISBN: 0977854027.

[2] B. D. Agarwal, L. J. Broutman, and K. Chandrashekhara. *Analysis and performance of fiber composites*. 3rd ed. Hoboken, N.J: John Wiley & Sons, 2006. ISBN: 0471268917;9780471268918.

[3] L. Iannucci et al. *Failure Models and Criteria for FRP Under In-Plane or Three-Dimensional Stress States Including Shear Non-Linearity*. Tech. rep. 2005.

[4] P. Robinson, E. Greenhalgh, and S. Pihno. *Failure mechanisms in polymer matrix composites*. Cambridge: Woodhead Publishing Limited, 2012. ISBN: 9781845697501.

[5] J.-K. Kim and M.-L. Sham. Impact and delamination failure of woven-fabric composites. English. *Composites Science and Technology* **60**.5 (2000), 745–761.

[6] S. Lomov and Knovel. *Non-Crimp Fabric Composites: Manufacturing, Properties and Applications*. English. Sawston;LaVergne; Woodhead Publishing Limited, 2011. ISBN: 1845697626;9781845697624;

[7] F. Edgren, L. E. Asp, and R. Joffe. Failure of NCF composites subjected to combined compression and shear loading. *Composites Science and Technology* **66**.15 (2006), 2865–2877.

[8] S. Hartmann, T. Klöppel, and C. Liebold. *Introduction to Composite Material Modeling with LS-DYNA*. Dynamore GmbH, 2014.

[9] N. Saabye Ottosen and H. Petersson. *Introduction to the finite element method*. Prentice Hall, 1992.

[10] J. Hallquist. *LS-DYNA theory manual*. California: Livermore Software Technology Corporation, 2006. ISBN: 0977854000.

[11] E. Qiuli Sun. *Shear Locking and Hourglassing in MSC Nastran, ABAQUS, and ANSYS*. Tech. rep. 2006.

[12] T. Bru et al. Characterisation of the mechanical and fracture properties of a uni-weave carbon fibre/epoxy non-crimp fabric composite. *Data in Brief* **6** (2016), 680–695.

[13] Sika®. *SikaPower®-MBX Class I*. Product Data Sheet Version 1, 2014.

[14] B. Alfredsson. *Handbok och formelsamling i Hållfasthetslära*. 11th ed. Instutitionen för hållfasthetslära KTH, 2014.

[15] M. Fagerström. Associate Professor at Chalmers University of Technology, Department of Applied Mechanics, Division of Material and Computational Mechanics, 2016.

[16] T. Erhart. *Review of Solid Element Formulations in LS-DYNA*. Tech. rep. 2011.

[17] U. Stelzmann. *Die große Elementbibliothek in LS-DYNA - Wann nimmt man was?* Tech. rep. 2010.

[18] *LS-DYNA keyword user's manual, Volume II, Material Models*. California: Livermore Software Technology Corporation, 2016.

[19] K. Björk. *Formler och Tabeller för Mekanisk Konstruktion - MEKANIK och HÅLLFASTHETSLÄRA*. 5th ed. Karl Björks Förlag HB, 2003.

[20] S. Bala. *Tie-Break Contacts in LS-DYNA*. Tech. rep. 2007.

[21] *Cohesive element formulation*. `http://www.dynasupport.com/howtos/element/cohesive-element-formulation`. Accessed: 2016-06-20.

[22] T. Graf, A. Haufe, and F. Andrade. *Adhesives modeling with LS-DYNA: Recent developments and future work*. Tech. rep. 2014.

[23] *LS-DYNA keyword user's manual, Volume II, Material Models*. California: Livermore Software Technology Corporation, 2015.

[24] A. Turon et al. *An engineering solution for mesh size effects in the simulation of delamination using cohesive zone models*. Tech. rep. 2006.

[25] Y. Mi et al. Progressive Delamination Using Interface Elements. *Journal of Composite Materials* **32**.14 (1998), 1246–1272.

[26] Z.Hashin. Failure Criteria for Unidirectional Fiber Composites. *Journal of Applied Mechanics* **47** (1980), 329–334.

Appendices

A Material cards

A.1 MAT22

Table A.1: Material card for MAT22

Card 1	MID	RO	EA	EB	EC	PRBA	PRCA	PRCB
		1500 kg/m^3	132 GPa	9 GPa	9 GPa	0.029	0.02	0.43
Card 2	GAB	GBC	GCA	(KFAIL)	AOPT	MACF		
	4.3 GPa	3.5 GPa	4.3 GPa		2	1		
Card 3	XP	YP	ZP	A1	A2	A3		
				0	1	0		
Card 4	V1	V2	V3	D1	D2	D3	BETA	
				1	0	0		
Card 5	SC	XT	YT	YC	ALPH	SN	SYZ	SZX
	77.8 MPa	1787 MPa	29.2 MPa	130 MPa	0	29.2 MPa	56.7 MPa	77.8 MPa

Table A.2: Description of abbreviations in Material model MAT22.

Name	**Description**
Card 1	
MID	Material ID (for the current model)
RO	Density (ρ)
EA	Young's modulus - longitudinal direction (E_a)
EB	Young's modulus - transverse direction (E_b)
EC	Young's modulus - normal direction (E_c)
PRBA	Poisson's ratio - *ba* (ν_{ba})
PRCA	Poisson's ratio - *ca* (ν_{ca})
PRCB	Poisson's ratio - *cb* (ν_{cb})
Card 2	
GAB	Shear modulus - *ab* (G_{ab})
GBC	Shear modulus - *bc* (G_{bc})
GCA	Shear modulus - *ca* (G_{ca})
KFAIL	Bulk modulus of failed material (K), necessary for compressive failure.
AOPT	Material axes option
MACF	Material axes flag, change axes for brick elements
Card 3	
[XP YP ZP]	Defines coordinate of point **p** for AOPT=1 and 4
[A1 A2 A3]	Defines component vector **a** for AOPT=2
MANGLE	Material angle (degrees) for AOPT=0 and 3
Card 4	
[V1 V2 V3]	Defines component vector **v** for AOPT=3 and 4
[D1 D2 D3]	Defines component vector **d** for AOPT=2
BETA	Material angle for AOPT=0 and 3 (degrees). Can be overrided by the element card.
Card 5	

SC	Shear strength - *ab*-plane (S_c)
XT	Tensile strength -longitudinal (X_t)
YT	Tensile strength - transverse (Y_t)
YC	Compressive strength- transverse (Y_c)
ALPH	Shear stress for the non-linear term
SN	Normal tensile strength - solid elements
SYZ	Transverse shear strength - solid elements
SZX	Transverse shear strength - solid elements

A.2 MAT54/55

Table A.3: Material card for MAT54/55

Card 1	MID	RO	EA	EB	EC	PRBA	PRCA	PRCB
		1500 kg/m^3	132 GPa	9 GPa	9 GPa	0.029	0.02	0.43
Card 2	GAB	GBC	GCA	(KF)	AOPT			
	4.3 GPa	3.5 GPa	4.3 GPa		2			
Card 3				A1	A2	A3	MANGLE	
				0	1	0		
Card 4	V1	V2	V3	D1	D2	D3	DFAILM	DFAILS
				1	0	0		
Card 5	TFAIL	ALPH	SOFT	FBRT	YCFAC	DFAILT	DFAILT	EFS
	-1	1000 GPa	1	0	2	0.0123	-0-0049	
Card 6	XC	XT	YC	YT	SC	CRIT	BETA	
	630 MPa	1787 MPa	130 MPa	29.2 MPa	77.8 MPa	55	1	
Card 7	PFL	EPSF	EPSR	TSMD	SOFT2			
Card 8	SLIMT1	SLIMC1	SLIMT2	SLIMC2	SLIMS	NCYRED	SOFTG	
							1	
Card 9	LCXC	LCXT	LCYC	LCYT	LCSC	DT		

Table A.4: Description of abbreviations in Material model MAT54/55.

Name	**Description**
Card 1	
MID	Material ID (for the current model)
RO	Density (ρ)
EA	Young's modulus - longitudinal direction (E_a)
EB	Young's modulus - transverse direction (E_b)
EC	Young's modulus - normal direction (E_c)
PRBA	Poisson's ratio - *ba* (ν_{ba})
PRCA	Poisson's ratio - *ca* (ν_{ca})
PRCB	Poisson's ratio - *cb* (ν_{cb})
Card 2	
GAB	Shear modulus - *ab* (G_{ab})
GBC	Shear modulus - *bc* (G_{bc})
GCA	Shear modulus - *ca* (G_{ca})
(KF)	Bulk modulus of failed material (not used) (K)
AOPT	Material axes option
Card 3	

[A1 A2 A3]	Defines component vector **a** for AOPT=2
MANGLE	Material angle (degrees) for AOPT=0 and 3
Card 4	
[V1 V2 V3]	Defines component vector **v** for AOPT=3
[D1 D2 D3]	Defines component vector **d** for AOPT=2
DFAILM	Maximum strain for matrix in tension and compression (only MAT54)
DFAILS	Maximum tensorial shear strain (only MAT54)
Card 5	
TFAIL	Time step criteria for element deletion
ALPH	Scear stress parameter for the non-linear term
SOFT	Softening reduction factor for material strength in crashfront
FBRT	Softening for fibre tensile strength
YCFAC	Reduction factor for compressive strength after matrix failure (only MAT54)
DFAILT	Maximum strain for fibre tension (only MAT54)
DFAILT	Maximum strain for fibre compression (only MAT54)
EFS	Effective failure strain (only MAT54)
Card 6	
XC	Compressive strength - longitudinal
XT	Tensile strength -longitudinal
YC	Compressive strength- transverse
YT	Tensile strength - transverse
SC	Shear strength - *ab* - plane
CRIT	Failure criteria (54 or 55)
BETA	Weight factor for shear term (only MAT54)
Card 7	Only MAT54
PFL	Percentage of layers that must fail before crashfront is initiated
EPSF	Damage initiation transverse shear strain
EPSR	Final rupture transverse shear strain
TSMD	Maximum damage, transverse shear
SOFT2	Softening reduction factor for material strength in crashfront elements "orthogonal"
Card 8	Only MAT54
SLIMT1	Factor to determine the minimum stress limit after stress maximum - fibre tension
SLIMC1	Factor to determine the minimum stress limit after stress maximum - fibre compression
SLIMT2	Factor to determine the minimum stress limit after stress maximum - matrix tension
SLIMC2	Factor to determine the minimum stress limit after stress maximum - matrix compression
SLIMS	Factor to determine the minimum stress limit after stress maximum - shear
NCYRED	Number of cycles for stress reduction from maximum to minimum
SOFTG	Softening reduction factor for shear stiffness in crashfront elements - transverse
Card 9	
LCXC	Load curve ID for XC - strain rate. Overrides XC in Card 6
LCXT	Load curve ID for XT - strain rate. Overrides XT in Card 6
LCYC	Load curve ID for YC - strain rate. Overrides YC in Card 6
LCYT	Load curve ID for YT - strain rate. Overrides YT in Card 6
LCSC	Load curve ID for SC - strain rate. Overrides SC in Card 6
DT	Strain rate averaging option

A.3 MAT58

Table A.5: Material card for MAT58

Card 1	MID	RO	EA	EB	(EC)	PRBA	TAU1	GAMMA
		1500 kg/m^3	132 GPa	9 GPa	9 GPa	0.029		
Card 2	GAB	GBC	GCA	SLIMT1	SLIMC1	SLIMT2	SLIMC2	SLIMS
	4.3 GPa	3.5 GPa	4.3 GPa					
Card 3	AOPT	TSIZE	ERODS	SOFT	FS	EPSF	EPSR	TSMD
	2				1			
Card 4	XP	YP	ZP	A1	A2	A3	PRCA	PRCB
				0	1	0	0.02	0.43
Card 5	V1	V2	V3	D1	D2	D3	BETA	
				1	0	0		
Card 6	E11C	E11T	E22C	E22T	GMS			
	0.0049	0.0123	0.0171	0.0032	0.091			
Card 7	XC	XT	YC	YT	SC			
	630 MPa	1787 MPa	130 MPa	29.2 MPa	77.8 MPa			
Card 8	LCXC	LCXT	LCYC	LCYT	LCSC	LCTAU	LCGAM	DT
Card 9	LCE11C	LCE11T	LCE22C	LCE22T	LCGMS	LCEFS		

Table A.6: Description of abbreviations in Material model MAT58

Name	**Description**
Card 1	
MID	Material ID (for the current model)
RO	Density
EA	Young's modulus - longitudinal direction
EB	Young's modulus - transverse direction
EC	Young's modulus - normal direction
PRBA	Poisson's ratio - *ba*
TAU1	Stress limit of the first slightly non-linear part of the shear stress-shear strain curve
GAMMA	Stain limit of the first slightly non-linear part of the shear stress-engineering shear strain curve
Card 2	
GAB	Shear modulus - *ab*
GBC	Shear modulus - *bc*
GCA	Shear modulus - *ca*
SLIMT1	Factor to determine minimum stress limit after stress maximum - fibre tension
SLIMC1	Factor to determine minimum stress limit after stress maximum - fibre compression
SLIMT2	Factor to determine minimum stress limit after stress maximum - matrix tension
SLIMC2	Factor to determine minimum stress limit after stress maximum - matrix compression
SLIMS	Factor to determine minimum stress limit after stress maximum - shear
Card 3	

AOPT	Material axes option
TSIZE	Time step for automatic element deletion
ERODS	Maximum effective strain for element layer failure
FS	Failure surface type
EPSF	Damage initiation - transverse shear strain
EPSR	Final rupture - transverse shear strain
TSMD	Maximum damage - transverse shear
Card 4	
[XP YP ZP]	Defines coordinates of point **p** for AOPT=1
[A1 A2 A3]	Defines component vector **a** for AOPT=2
PRCA	Poisson's ratio - *ca*
PRCB	Poisson's ratio - *cb*
Card 5	
[V1 V2 V3]	Defines component vector **v** for AOPT=3
[D1 D2 D3]	Defines component vector **d** for AOPT=2
BETA	Material angle for AOPT = 0 and 3 (°)
Card 6	
E11C	Strain at longitudinal compressive strength
E11T	Strain at longitudinal tensile strength
E22C	Strain at transversal compressive strength
E22T	Strain at transversal tensile strength
GMS	Engineering shear stain at shear strength
Card 7	
XC	Compressive strength - longitudinal
XT	Tensile strength -longitudinal
YC	Compressive strength- transverse
YT	Tensile strength - transverse
SC	Shear strength - *ab* - plane
Card 8	
LCXC	Load curve ID for XC - strain rate. Overrides XC in Card 7
LCXT	Load curve ID for XT - strain rate. Overrides XT in Card 7
LCYC	Load curve ID for YC - strain rate. Overrides YC in Card 7
LCYT	Load curve ID for YT - strain rate. Overrides YT in Card 7
LCSC	Load curve ID for SC - strain rate. Overrides SC in Card 7
LCTAU	Load curve ID for TAU1 - strain rate. Overrides TAU1 in Card 1. Only used for FS=-1
LCGAM	Load curve ID for GAMMA - strain rate. Overrides GAMMA in Card 1. Only used for FS=-1
DT	Strain rate averaging option
Card 9	
LCE11C	Load curve ID for E11C - strain rate. Overrides E11C in Card 6
LCE11T	Load curve ID for E11T - strain rate. Overrides E11T in Card 6
LCE22C	Load curve ID for E22C - strain rate. Overrides E22C in Card 6
LCE22T	Load curve ID for E22T - strain rate. Overrides E22T in Card 7
LCGMS	Load curve ID for GMS - strain rate. Overrides GMS in Card 6
LCEFS	Load curve ID for ERODS - strain rate. Overrides ERODS in Card 3

A.4 MAT261

Table A.7: Material cards for MAT261

Card 1	MID	RO	EA	EB	(EC)	PRBA	PRCA	PRCB
		1500 kg/m^3	132 GPa	9 GPa	9 GPa	0.029	0.02	0.43
Card 2	GAB	GBA	GCA	AOPT	DAF	DKF	DMF	EFS
	4.3 GPa	3.5 GPa	4.3 GPa	2	0	0	0	0
Card 3	XP	YP	ZP	A1	A2	A3		
				0	1	0		
Card 4	V1	V2	V3	D1	D2	D3	MANGLE	
				1	0	0		
Card 5	ENKINK	ENA	ENB	ENT	ENL			
	103.1 kJ/m^2	67.1 kJ/m^2	51.8 kJ/m^2	33.7 kJ/m^2	33.7 kJ/m^2			
Card 6	XC	XT	YC	YT	SL			
	630 MPa	1787 MPa	130 MPa	29.2 MPa	77.8 MPa			
Card 7	FIO	SIGY	LCSS	BETA	FPL	PUCK	SOFT	
	62 °	1000 GPa	0	0	0	0	1	

Table A.8: Description of abbreviations in Material model 261

Name	**Description**
Card 1	
MID	Material ID (for the current model)
RO	Density
EA	Young's modulus - longitudinal direction
EB	Young's modulus - transverse direction
EC	Young's modulus - normal direction
PRBA	Poisson's ratio - *ba*
PRCA	Poisson's ratio - *ca*
PRCB	Poisson's ratio - *cb*
Card 2	
GAB	Shear modulus - *ab*
GBA	Shear modulus - *bc*
GCA	Shear modulus - *ca*
AOPT	Material axes option
DAF	Flag to control failure of integration point - longitudinal tensile fibre failure
DKF	Flag to control failure of integration point - longitudinal compressive fibre failure
DMF	Flag to control failure of integration point - transverse matrix failure
Card 3	
[XP YP ZP]	Defines component vector **p** for AOPT=1 & 4
[A1 A2 A3]	Defines component vector **a** for AOPT=2
Card 4	
[V1 V2 V3]	Defines component vector **v** for AOPT=3
[D1 D2 D3]	Defines component vector **d** for AOPT=2
MANGLE	Material angle (degrees) for AOPT=0& 3
Card 5	
ENKINK	Fracture toughness for longitudinal compressive fibre failure
ENA	Fracture toughness for longitudinal tensile fibre failure
ENB	Fracture toughness for interlaminar tensile matrix failure
ENT	Fracture toughness for interlaminar transverse shear matrix failure
ENL	Fracture toughness for interlaminar longitudinal shear matrix failure
Card 6	

XC	Compressive strength - longitudinal
XT	Tensile strength -longitudinal
YC	Compressive strength- transverse
YT	Tensile strength - transverse
SL	Longitudinal shear strength
Card 7	
FIO	Fracture angle in pure transverse compression (°)
SIGY	In-plane shear yield stress
LCSS	Load curve or Table ID
BETA	Hardening parameter for in-plane shear plasticity
PFL	Percentage of elements that must fail before crashfront is initiated
PUCK	Flag for evaluation and postprocessing of the Puck criterion
SOFT	Softening reduction factor for material strength in the crashfront

A.5 MAT262

Table A.9: Material cards for MAT262

Card 1	MID	RO	EA	EB	(EC)	PRBA	PRCA	PRCB
		1500 kg/m^3	132 GPa	9 GPa	9 GPa	0.029	0.02	0.43
Card 2	GAB	GBA	GCA	AOPT	DAF	DKF	DMF	EFS
	4.3 GPa	3.5 GPa	4.3 GPa	2	0	0	0	0
Card 3	XP	YP	ZP	A1	A2	A3		
				0	1	0		
Card 4	V1	V2	V3	D1	D2	D3	MANGLE	
				1	0	0		
Card 5	GXC	GXT	GYC	GYT	GLS	GXCO	GXTO	
	103.1 kJ/m^2	67.1 kJ/m^2	51.8 kJ/m^2	33.7 kJ/m^2	33.7 kJ/m^2			
Card 6	XC	XT	YC	YT	SL	XCO	XTO	
	630 MPa	1787 MPa	130 MPa	29.2 MPa	77.8 MPa			
Card 7	FIO	SIGY	ETAN	BETA	FPL	PUCK	SOFT	
	62 °	1000 GPa	0	0	0	0	1	

Table A.10: Description of abbreviations in Material model 261

Name	**Description**
Card 1	
MID	Material ID (for the current model)
RO	Density
EA	Young's modulus - longitudinal direction
EB	Young's modulus - transverse direction
EC	Young's modulus - normal direction
PRBA	Poisson's ratio - *ba*
PRCA	Poisson's ratio - *ca*
PRCB	Poisson's ratio - *cb*
Card 2	
GAB	Shear modulus - *ab*
GBA	Shear modulus - *bc*
GCA	Shear modulus - *ca*
AOPT	Material axes option
DAF	Flag to control failure of integration point - longitudinal tensile fibre failure
DKF	Flag to control failure of integration point - longitudinal compressive fibre failure
DMF	Flag to control failure of integration point - transverse matrix failure
Card 3	
[XP YP ZP]	Defines component vector **p** for AOPT=1 & 4
[A1 A2 A3]	Defines component vector **a** for AOPT=2
Card 4	
[V1 V2 V3]	Defines component vector **v** for AOPT=3
[D1 D2 D3]	Defines component vector **d** for AOPT=2
MANGLE	Material angle (degrees) for AOPT=0& 3
Card 5	
GXC	Fracture toughness for longitudinal compressive fibre failure
GXT	Fracture toughness for longitudinal tensile fibre failure
GYC	Fracture toughness for transverse compressive failure
GYT	Fracture toughness for transverse tensile failure
GSL	Fracture toughness for in-plane shear failure

GXCO	Fracture toughness for longitudinal compression fibre failure - bi-linear damage evolution
GXTO	Fracture toughness for longitudinal tension fibre failure - bi-linear damage evolution
Card 6	
XC	Compressive strength - longitudinal
XT	Tensile strength -longitudinal
YC	Compressive strength- transverse
YT	Tensile strength - transverse
SL	Longitudinal shear strength
XCO	Longitudinal compressive strength at inflection point
XTO	Longitudinal tensile strength at inflection point
Card 7	
FIO	Fracture angle in pure transverse compression (°)
SIGY	In-plane shear yield stress
LCSS	Load curve or Table ID
BETA	Hardening parameter for in-plane shear plasticity
PFL	PErcentage of elements that must fail before crashfront is initiated
PUCK	Flag for evaluation and postprocessing of the Puck criterion
SOFT	Softening reduction factor for material strength in the crashfront

B Tiebreak card

B.1 AUTOMATIC_SURFACE_TO_SURFACE_TIEBREAK

Table B.1: Contact card for AUTOMATIC_SURFACE_TO_SURFACE_TIEBREAK

Card 1	SSID	MSID	SSTYP	MSTYP	SBOXID	MBOXID	SPR	MPR
				3	3		0	0
Card 2	FS	FD	DC	VC	VCD	PENCHK	BT	DT
					20	0		
Card 3	SFS	SFM	SST	MST	SFST	SFMT	FSF	VSF
Card 4	OPTION	NFLS	SFLS	PARAM	ERATEN	ERATES	CT2CN	CN
	4	29.2 MPa	77.8 MPa	1				
Card A	SOFT	SOFTCL	LCIDAB	MAXPAR	SBOPT	DEPTH/LCID	DEPTH	BSORT/LCID
	0	0.1		1.025	0	DEPTH	2	BSORT
A, cont							BSORT	FRCFRQ
							10	0

C Failure criteria

All information in this section is from the LS-DYNA keyword manual [18]. Variables for all criteria:

σ_{aa}	Stress from FE analysis - *aa*	σ_{ab}	Stress from FE analysis - *ab*
σ_{bb}	Stress from FE analysis - *bb*		
E_a	Young's modulus - longitudinal	E_b	Young's modulus - transverse
E_c	Young's modulus - normal	ν_{ba}	Poisson's ratio *ba*
ν_{ca}	Poisson's ratio *ca*	ν_{cb}	Poisson's ratio *cb*
G_{ab}	Shear modulus *ab*	G_{bc}	Shear modulus *bc*
X_c	Compressive strength - longitudinal	X_t	Tensile strength - longitudinal
Y_c	Compressive strength - transverse	Y_t	Tensile strength - transverse
S_c	Shear strength	S_l	Longitudinal shear strength
$\tilde{\sigma}$	Effective stress tensor	ϕ	Fracture plane for general loading
ϕ_o	Fracture plane for pure compression	Ψ	Angle to principal stress

Table C.1: Variables used in failure criteria calculations

C.1 Chang-Chang

Tensile fibre mode:

$$\sigma_{aa} > 0 \ then \ e_f^2 = \left(\frac{\sigma_{aa}}{X_t}\right)^2 + \beta\left(\frac{\sigma_{ab}}{S_c}\right) - 1 \begin{cases} \geq 0 & failed \\ < 0 & elastic \end{cases} \tag{C.1}$$

$$E_a = E_b = G_{ab} = \nu_{ba} = \nu_{ab} = 0$$

Compressive fibre mode:

$$\sigma_{aa} < 0 \ then \ e_c^2 = \left(\frac{\sigma_{aa}}{X_c}\right)^2 - 1 \begin{cases} \geq 0 & failed \\ < 0 & elastic \end{cases} \tag{C.2}$$

$$E_a = \nu_{ba} = \nu_{ab} = 0$$

Tensile matrix mode:

$$\sigma_{bb} > 0 \ then \ e_m^2 = \left(\frac{\sigma_{bb}}{Y_t}\right)^2 + \left(\frac{\sigma_{ab}}{S_c}\right)^2 - 1 \begin{cases} \geq 0 & failed \\ < 0 & elastic \end{cases} \tag{C.3}$$

$$E_a = \nu_{ba} = 0 \implies G_{ab} = 0$$

Compressive matrix mode:

$$\sigma_{bb} < 0 \ then \ e_d^2 = \left(\frac{\sigma_{bb}}{2S_c}\right)^2 + \left[\left(\frac{Y_c}{2S_c}\right)^2 - 1\right]\frac{\sigma_{bb}}{Y_c} + \left(\frac{\sigma_{ab}}{S_c}\right)^2 - 1 \begin{cases} \geq 0 & failed \\ < 0 & elastic \end{cases} \tag{C.4}$$

$$E_b = \nu_{ba} = \nu_{ab} = 0 \implies G_{ab} = 0$$

$$X_c = 2Y_c \text{ for } 50\% \text{ fibre volume}$$

C.2 Tsai-Wu

The tensile and compressive fibre failure criteria for Tsai-Wu are the same as for Chang-Chang, see equations (C.1) and (C.2). The same equation is used for both tensile and compressive matrix failure, see (C.5).

$$e_{md}^2 = \frac{\sigma_{bb}^2}{Y_c Y_t}\left(\frac{\sigma_{ab}}{S_c}\right)^2 + \frac{(Y_c - Y_t)\,\sigma_{bb}}{Y_c Y_t} - 1 \begin{cases} \geq 0 & failed \\ < 0 & elastic \end{cases} \tag{C.5}$$

C.3 Modified Hashin

[26]

Tensile fibre mode:

$$f_a = \{\sigma_{aa} > 0\} = \left(\frac{\sigma_{aa}}{X_t}\right)^2 + \left(\frac{\tau_{ab}}{S_l}\right)^2 \begin{cases} \geq 1 & \textit{failed} \\ < 1 & \textit{no failure} \end{cases} \tag{C.6}$$

Compressive fibre mode:

$$f_a = \{\sigma_{aa} < 0\} = \left(\frac{\sigma_{aa}}{X_c}\right)^2 \begin{cases} \geq 1 & \textit{failed} \\ < 1 & \textit{no failure} \end{cases} \tag{C.7}$$

Tensile matrix mode:

$$f_a = \left(\frac{\sigma_{bb}}{Y_t}\right)^2 + \left(\frac{\tau_{ab}}{S_l}\right)^2 \begin{cases} \geq 1 & \textit{failed} \\ < 1 & \textit{no failure} \end{cases} \tag{C.8}$$

Compressive matrix mode:

$$f_a = \left(\frac{\sigma_{bb}}{2S_c}\right)^2 + \left(\left(\frac{Y_c}{2S_c}\right)^2 - 1\right)\frac{\sigma_{bb}}{Y_t} + \left(\frac{\tau_{bb}}{S_l}\right)^2 \begin{cases} \geq 1 & \textit{failed} \\ < 1 & \textit{no failure} \end{cases} \tag{C.9}$$

C.4 Pinho

Tensile fibre mode:

$$f_a = \frac{\sigma_a}{X_t} \begin{cases} \geq 1 & \textit{failed} \\ < 1 & \textit{no failure} \end{cases} \tag{C.10}$$

Compressive fibre mode (kinking model):

$$f_{kink} = \begin{cases} \left(\frac{\tau_t}{S_t - \mu_t \sigma_n}\right)^2 + \left(\frac{\tau_l}{S_l - \mu_l \sigma_n}\right)^2 = 1 & \textit{if } \sigma_{b^m} \geq 0 \\ \left(\frac{\sigma_n}{Y_t}\right)^2 + \left(\frac{\tau_t}{S_t}\right)^2 + \left(\frac{\tau_l}{S_l}\right)^2 = 1 & \textit{if } \sigma_{b^m} > 0 \end{cases} \tag{C.11}$$

with $S_t = \frac{Y_c}{2tan(\phi_o)}$, $\mu_t = -\frac{1}{tan(2\phi_o)}$, $\mu_l = S_l \frac{\mu_t}{S_t}$

$$\sigma_n = \frac{\sigma_{b^m} + \sigma_{c^\Psi}}{2} + \frac{\sigma_{b^m} - \sigma_{c^\Psi}}{2} cos(2\phi) + \tau_{b^m c^\Psi} sin(2\phi)$$

$$\tau_t = -\frac{\sigma_{b^m} - \sigma_{c^\Psi}}{2} sin(2\phi) + \tau_{b^m c^\Psi} cos(2\phi)$$

$$\tau_l = \tau_{a^m b^m} cos(2\phi) + \tau_{c^\Psi a^m} sin(\phi)$$

Tensile matrix mode:

$$\textit{if } \sigma \geq 0 \; f_{mat} = \left(\frac{\sigma_n}{Y_t}\right)^2 + \left(\frac{\tau_t}{S_t}\right)^2 + \left(\frac{\tau_l}{S_l}\right)^2 \begin{cases} \geq 1 & \textit{failed} \\ < 1 & \textit{no failure} \end{cases} \tag{C.12}$$

with

$$\sigma_n = \frac{\sigma_b + \sigma_c}{2} + \frac{\sigma_b - \sigma_c}{2} cos(2\phi) + \tau_{bc} sin(2\phi)$$

$$\tau_t = -\frac{\sigma_b - \sigma_c}{2} sin(2\phi) + \tau_{bc} cos(2\phi)$$

$$\tau_l = \tau_{ab}cos(2\phi) + \tau_{ca}sin(\phi)$$

Compressive matrix mode:

$$if\ \sigma < 0\ f_{mat} = \left(\frac{\tau_t}{S_t - \mu_t\sigma_n}\right)^2 + \left(\frac{\tau_l}{S_l - \mu_l\sigma_n}\right)^2 \begin{cases} \geq 1 & failed \\ < 1 & no\ failure \end{cases} \tag{C.13}$$

C.5 Camanho

Tensile fibre mode:

$$\phi_{1+} = \frac{\sigma_{11} - \nu_{12}\sigma_{22}}{X_t} \begin{cases} \geq 1 & failed \\ < 1 & no\ failure \end{cases} \tag{C.14}$$

Compressive fibre mode:

$$\phi_{1-} = \frac{\langle|\sigma_{12}^m| + \mu_l\sigma_{22}^m\rangle}{S_l} \begin{cases} \geq 1 & failed \\ < 1 & no\ failure \end{cases} \tag{C.15}$$

with

$$\mu_l = -\frac{S_l cos(2\phi_o)}{Y_c cos^2(\phi_o)}$$

$$\sigma_{22}^m = \sigma_{11}sin^2(\varphi^c) + \sigma_{22}cos^2(\varphi^c) - 2|\sigma_{12}|sin(\varphi^c)cos(\varphi^c)$$

$$\sigma_{12}^m = (\sigma_{22} - \sigma_{11})\,sin(\varphi^c)cos(\varphi^c) + |\sigma_{12}|\left(cos^2(\varphi^c) - sin^2(\varphi^c)\right)$$

$$\varphi^c = arctan\left[\frac{1 - \sqrt{1 - 4\left(\frac{S_l}{X_c} + \mu_l\right)\frac{S_l}{X_c}}}{2\left(\frac{S_l}{X_c} + \mu_l\right)}\right]$$

Tensile matrix mode (perpendicular to the laminate mid-plane):

$$\phi_{2+} = \begin{cases} if\ \sigma_{22} \geq 0\ then\ \sqrt{(1-g)\,\frac{\sigma_{22}}{Y_t} + g\left(\frac{\sigma_{22}}{Y_y}\right)^2 + \left(\frac{\sigma_{12}}{S_l}\right)^2} \\ if\ \sigma_{22} < 0\ then\ \frac{\langle|\sigma_{12}| + \mu_l\sigma_{22}\rangle}{S_l} \end{cases} \quad \begin{cases} \geq 1 & failed \\ < 1 & no\ failure \end{cases} \tag{C.16}$$

Compressive/shear matrix mode:

$$if\ \sigma_{22} < 0 then\ \ \phi_{2-} = \sqrt{\left(\frac{\tau_t}{S_t}\right)^2 + \left(\frac{\tau_l}{S_l}\right)^2} \begin{cases} \geq 1 & failed \\ < 1 & no\ failure \end{cases} \tag{C.17}$$

With

$$\begin{aligned} \mu_t =& -\frac{1}{tan(2\phi_o)} \\ S_t =& Y_c cos(\phi_o)\left[sin(\phi_o) + \frac{cos(\phi_o)}{tan(2\phi_o)}\right] \\ \theta =& arctan\left(\frac{-|\sigma_{12}|}{\sigma_{22}sin(\phi_o)}\right) \\ \tau_t =& \langle -\sigma_{22}cos(\phi_o)\left[sin(\phi_o) - \mu_t cos(\phi_o)cos(\theta)\right]\rangle \\ \tau_l =& \langle cos(\phi_o)\left[|\sigma_{12}| + \mu_l\sigma_{22}cos(\phi_o)sin(\theta)\right]\rangle \end{aligned}$$